ABSTRACT

THOMAS, REBECCA LYNN. Effect of Rare-Earth Incorporation in Ferromagnetic Metals for Magnetic Domain Wall Devices. (Under the direction of Dr. Veena Misra).

Devices that utilize propagation of magnetic domain walls are of interest for memory and logic applications. These devices are inherently non-volatile and have the potential for major reductions in energy consumption and required power dissipation. However, the speed of these devices must increase to compete with conventional electronics and the energy required to switch and propagate magnetic domains must be reduced to achieve low-power operation.

While Permalloy wires have been widely studied in recent years for domain wall based device applications, domain walls propagated by a spin-polarized current through Permalloy require high critical current densities to initiate domain wall motion and exhibit low velocities. Domain wall dynamics caused by an applied current are not yet fully understood and must be further explored and optimized to establish domain wall device concepts as viable technologies. Magnetization dynamics depend strongly on material properties yet utilization of materials engineering to provide insight and enhancements in dynamics is an area that has not been adequately explored.

In this work, we study novel magnetic metal alloys created by doping ferromagnetic materials with rare-earth elements and evaluate their potential to enhance domain wall dynamics thereby improving domain wall device performance. We focus on Gd dopants that reduce magnetization of magnetic transition metals by antiferromagnetic coupling while still maintaining a low Gilbert damping factor. Dopant atoms should also act as scattering centers that reduce the spin-flip length thus enhancing the non-adiabatic spin torque factor. The

static magnetic properties and crystallinity of various film compositions incorporating Gd dopants in Permalloy, Ni and Co are characterized by SQUID magnetometry and XRD measurements. The measurements confirm that Gd dopants decrease the film magnetization and destroy the film crystallinity creating amorphous films with low coercive fields.

Measurements analyzing the effect of Gd dopants on magnetization dynamics are limited to doped Permalloy films because Permalloy has the lowest Gilbert damping factor and has been extensively characterized. FMR measurements demonstrate a small effect on the Gilbert damping factor and verify that co-sputtering yields high-quality uniform thin films. The spin transfer velocity and current polarization are measured using a spin wave Doppler technique. Through measurements, it was found for the first time, that introducing Gd dopants results in a considerable reduction in current polarization which reduces the spin transfer velocity.

These results are verified with the first domain wall velocity measurements through PyGd wires performed using time-resolved MOKE magnetometry. The spin transfer velocity for Permalloy reduces by 30% for the $Py_{0.921}Gd_{0.079}$ composition. The effect of the non-adiabatic spin torque contribution is determined through current-assisted domain wall depinning measurements. An unexpected negative spin torque effect is measured for two of the PyGd compositions implying a negative non-adiabatic factor.

In summary, this work explores new magnetic materials and provides insight into current-induced domain wall dynamics that can be used to enhance the domain wall velocity for device applications. These findings indicate that rare-earth dopants are useful for devices utilizing magnetic field propagation resulting in similar velocities as Permalloy but at lower magnetic fields. However, for devices that propagate domain walls using spin-polarized current, the rare-earth doping technique is not beneficial due to the unexpected degradation in spin torque efficiency. This work is the first of its kind to reveal this mechanism and provides insight into the impact of rare-earth incorporation on domain wall dynamics. Although these devices may not provide the expected increase in velocity, the use of rare-earth dopants in magnetic materials provides a platform to study domain wall dynamics by allowing the tuning of material parameters and correlating the impact on domain wall velocities.

Effect of Rare-Earth Incorporation in Ferromagnetic Metals for Magnetic Domain Wall Devices

by
Rebecca Lynn Thomas

A dissertation submitted to the Graduate Faculty of
North Carolina State University
in partial fulfillment of the
requirements for the degree of
Doctor of Philosophy

Electrical Engineering

Raleigh, North Carolina

2012

APPROVED BY:

Dr. Veena Misra
Chair of Advisory Committee

Dr. Michael Escuti

Dr. Mehmet Ozturk

Dr. Nadia El-Masry

DEDICATION

To my parents
Dale and Bonita Scott

and my husband
Stewart Thomas

BIOGRAPHY

Rebecca Thomas attended the University of Louisville where she received both the Bachelor of Science and Masters of Engineering degrees with Highest Honors. Her master's research involved designing and fabricating a microfluidic Coulter counter utilizing three-dimensional hydrodynamic focusing and was conducted under the direction of Dr. Cindy K. Harnett. In August 2007, Rebecca enrolled in as a graduate student in the Electrical and Computer Engineering Department at North Carolina State University in Raleigh, North Carolina. Her dissertation research involved researching magnetic nanostructures and magnetic domain wall dynamics. The advisor for her doctoral work was Dr. Veena Misra.

ACKNOWLEDGMENTS

This dissertation would not have been possible without the help and support of a long list of people. First of all, I would like to express my gratitude to my advisor, Dr. Veena Misra, for her guidance and encouragement throughout this work. I would also like to thank Dr. Michael Escuti, Dr. Mehmet Ozturk and Dr. Nadia El-Masry for serving on my advisory committee and for the helpful insight on this work, and Dr. John Muth for being a substitute committee member during my final defense.

I am grateful for the Misra group for their insightful discussions, contributions to this work and friendship. Thank you to Casey Kirkpatrick, Srikant Jayanti, Xiangyu Yang, Narayanan Ramanan, Steven Mills, Michael Lim, Dr. Rahul Suri, Jason Culp, Dr. Smita Sarkar, Dr. Bongmook Lee, and Dr. Niv Biswas for being great group members. A special thanks to Dr. Steven Novak for the proposal idea and his assistance throughout this work especially in programming the automated magnetic measurements. Thank you to the NCSU and Duke University clean room staff and especially Henry Taylor and Jay Dalton for processing help and discussions.

I would like to acknowledge funding support from the Semiconductor Research Corporation's Nanoelectronics Research Initiative INDEX center and the U.S. Department of Education Graduate Assistance in the areas on National Need (GAANN) Fellowship Program in the area of Nanoscale Electronic and Energy Materials (NEEM). I would also like to take this opportunity to thank all of my collaborators. Thank you to everyone that has helped me at the National Institute of Standards and Technology including Dr. Robert McMicheal, Dr. John Read and Dr. Mung Zhu for collaborations with FMR and spin wave

Doppler measurements, Dr. Cindi Dennis for SQUID measurements, and Dr. John Unguris, Dr. Ben McMorran and Dr. Samuel Bowden for working with me on SEMPA measurements. I would also like to thank my collaborators at MIT, Dr. Geoff Beach and the Beach group for making me feel welcome and allowing me to use their MOKE setup. I am indebted to Satoru Emori for help in running measurements, processing data and data analysis.

I would also like to thank my classmates and study group for spending many hours with me working on homework and studying for exams; Thanks to Anne Costolanski, Edward Van Brunt and Kristopher Lawler. Finally, it is an honor for me to acknowledge the great friends I have in Raleigh that help me to stay sane and have a life outside of graduate school. Thank you to the members of the IV Graduate Christian Fellowship for teaching me to approach all texts with the same amount of scrutiny as academic texts, making my experience in graduate school much more enjoyable and for being my best friends and family. I am so glad that all of you are a part of my life. Last but definitely not least, I am grateful for my wonderful husband, Stewart Thomas, for dealing with my stress, always listening to my problems, being my number one editor and being my best friend.

TABLE OF CONTENTS

LIST OF TABLES

LIST OF FIGURES

LIST OF SYMBOLS

A	Exchange stiffness constant
B	Number of binary transitions per unit time
e	Electron charge
E_{bit}	Energy per bit transition
E_w	Domain wall energy per unit area
g	Landé factor
$\mathbf{H}$	Effective magnetic field
H_k	Anisotropy field
H_p	Effective pinning field
H_{res}	Ferromagnetic resonance field
H_w	Walker breakdown field
$\mathbf{J}$	Current density
j_{th}	Critical current density required to initiate domain wall motion
J_w	Walker breakdown current density
K	Anisotropy constant
$\mathbf{k}$	Spin wave vector
k_B	Boltzmann's constant
M_{eff}	Effective magnetization
M_s	Saturation magnetization
n	Integration density
P	Spin polarization

PD	Require power dissipation per unit area
t	Device switching time
T	Temperature
$\mathbf{u}$	Spin transfer velocity
$\mathbf{v_{DW}}$	Domain wall velocity
α	Gilbert damping factor
β	Non-adiabatic factor
γ	Gyromagnetic ratio
Δ	Domain wall width
ΔH	Ferromagnetic resonance linewidth
ΔH_0	Inhomogeneous broadening term
Δw	Shift in the spin wave angular frequency
$\hbar$	Dirac constant
η	Torque due to the adiabatic spin transfer
λ_J	Exchange length
λ_{sf}	Spin-flip length
μ	Mobility of a domain wall due to a magnetic field
μ_0	Permeability of free space
μ_B	Bohr magnetron

LIST OF ACRONYMS

ALD	Atomic layer deposition
CMOS	Complementary metal-oxide semiconductor technology for creating integrated circuits
CPP	Current perpendicular to the plane
CPW	Coplanar waveguide
DAQ	Data acquisition
EBL	Electron beam lithography
FIB	Focused ion beam
FMR	Ferromagnetic resonance
GMR	Giant magnetoresistance
IPA	Isopropanol alcohol
LOR	Lift-off resist
MIBK	Methyl isobutyl ketone
MOKE	Magneto-optical Kerr effect
MRAM	Magnetic random-access memory
NMP	N-methyl-2-pyrolidone
PMA	Perpendicular magnetic anisotropy
PMGI	Polymethylglutarimide
PMMA	Polymethyl methacrylate (Positive electron sensitive resist)
RF	Radio frequency
SEM	Scanning electron microscope

SQUID	Superconducting quantum interference device
TMA	Trimethyl Aluminum
XRD	X-ray diffraction

CHAPTER 1

INTRODUCTION

1.1 Motivation for Spintronics

The scaling limits for Moore's law based on traditional complementary metal-oxide-semiconductor (CMOS) processes will soon be reached. One of the fundamental problems facing future CMOS is power dissipation. The following analysis and equations of CMOS scaling projections are originally from Zhirnov *et al.* [1]. Scaling continues to improve both device switching time, t, and integration density, n, resulting in an exponential increase in the number of binary transitions per unit time, $B=n/t$. In order to maintain the power dissipation while keeping optimal device performance, the energy per bit transition must be reduced. For charge-based devices an energy barrier with less than 50% probability of spontaneous transition must be maintained. Therefore, the energy per bit transition has a fundamental limit given by the Shannon-von Neumann Landuer expression

$$E_{bit} = k_B T \ln 2 = 0.017eV = 2.87\times10^{-9}\, pJ. \tag{1.1}$$

For comparison, the energy per bit transition of the 45 nm gate process is $1.5 \times 10^{-4}\, pJ$. Based on Heisenberg's uncertainty relations, minimum values of gate size and switching times at the fundamental energy limit are 1.5 nm and 0.04 ps respectively. These values along with the maximum density of switches determine the required power dissipation,

$$PD = \frac{n_{\max} E_{bit}}{t_{\min}} = 3.7\times10^{6}\, {W}/{cm^2}\,. \tag{1.2}$$

The required amount of power dissipation is much too large to achieve these optimal parameters. Power dissipation of only ~100 W/cm^2 can be achieved using passive cooling techniques [2] and using other known cooling techniques several hundred W/cm^2 of power can be dissipated.

As the limits of heat removal capacity are approached, speed and density cannot continue to be scaled simultaneously. Tradeoffs between density and the frequency of the devices will be required. Since heat dissipation limits any device using electronic charge, to maintain scaling trends alternate state variables with lower energy per bit transitions are required. Therefore, devices utilizing new computational state variables such as spin, phonons and photon fields are being investigated. The use of state variables other than electronic charge offers great new opportunities for novel logic and memory approaches and can help create a new computational roadmap.

One promising alternative that has been the focus of intense research in recent years is the emerging field of spintronics. Spintronics uses both the spin and charge of electrons for data storage and operations. Two different approaches in utilizing electron spin have emerged. One approach is based on spin-polarized electrons in semiconductors. The second approach uses the magnetization direction of magnetic domains in ferromagnets as a method to represent information. Domains are regions of uniform magnetization that cause magnetic behavior in ferromagnetic materials. The details of the formation and orientation of magnetic domains will be described in the next chapter.

Magnetic devices offer potential benefits over conventional charge-based devices. Magnetic materials exhibit hysteresis. When an external field is applied, the atomic dipoles within a magnetic material align with the field and their state is maintained even after the field is removed. Consequently, devices utilizing magnetism will be non-volatile and therefore save energy as information is retained without power. Non-volatility is important for mobile devices that can boot almost instantaneously. Since magnetic devices do not physically change their structure, they do not exhibit any wearout mechanisms. Magnetic devices enable increased density and have potential for much lower power dissipation compared with charge based devices since electronic charge is not moving. Additionally, magnetism is already well established and widely used in commercial devices for data storage and memory. Read-out heads based on giant magnetoresistance (GMR) were introduced in 1997 and have enabled the miniaturization of magnetic hard disk drives in recent years [3]. Magnetic random-access memory (MRAM) which was first commercialized in 2005 has been hailed as the "holy grail" of logic because it is non-volatile, high density and high-speed. Consequently, future device applications involving magnetics are generating great excitement.

1.2 Magnetic Device Concepts

Domain wall motion in thin films generated much interest in the 1960s and 1970s through a non-volatile memory concept known as Magnetic bubble memory. These devices worked by controlling the motion of cylindrical domains, or bubbles, in epitaxial garnet films using magnetic field gradients. One mechanism to produce a magnetic field gradient involves adjacent tracks of Permalloy [4]. The bubble memory concept was proven and commercialized by several companies in the late 1970s, but ultimately was outpaced by hard disk drives with regards to capacity and cost. However, bubble memory had some key attributes including non-volatility, operation using solid-state technology, high reliability and suitability with harsh environments.

Fast forwarding approximately 20 years after bubble memory became obsolete, a related concept began to emerge as an alternative route for logic and memory applications. This concept was based on manipulating magnetization by moving the mobile interfaces between domains, called domain walls, through ferromagnetic wires have been proposed for both memory [5] and logic applications [6]. The smallest bubble diameter possible in epitaxial garnet is 0.3 μm while domain walls can have widths as low as 1 nm. To avoid interference, bubbles should be separated by at least four times their diameter. It is estimated that domain walls can be separated by a minimum distance of ~0.8 μm dependent on the wire dimensions but using pinning centers to stabilize the domain walls have allowed them to be spaced more closely [7]. In addition, advancements in magnetic sensing enable reading of smaller magnetic domains. As a result, these new devices potentially have much higher densities and better efficiency when compared with bubble memory.

In 2005, Allwood *et al.* demonstrated magnetic logic by propagating domains through geometrically patterned nanowire structures using a rotating magnetic field [6]. A complete set of logic functions were accomplished using single-layer lithography through this technique that represents Boolean logic states according to the direction of the wire's magnetization and the direction of domain wall motion. Wire magnetization and domain wall motion in the same direction are evaluated as a "1" while opposing directions are evaluated as a "0".

This magnetic logic demonstration accomplished the NOT operation by patterning a cusp shape that will rotate the direction of the wire's magnetization by 180 degrees as illustrated in Fig. 1.1 [8]. The magnetization is rotated 90 degrees as the domain wall moves into the cusp and around the first corner of the junction with a corresponding magnetic field. The domain wall remains in the central section of the cusp until the field rotates in the opposite direction. The domain wall then rotates a further 90 degrees by moving out of the cusp with its tail end first. The NOT-gate therefore functions with a propagation delay equal to half of the field rotation cycle. The proposed magnetic logic functions have very simple structures and can be fabricated in a single lithography step. A comparison of implementing an AND function in CMOS and magnetic domain-wall logic is shown in Fig. 1.2. Table 1.1 provides a comparison between magnetic logic and traditional CMOS logic devices.

Researchers at IBM are developing a new form of magnetic memory referred to as "racetrack" memory that utilizes current to create and move series of domain walls through a nanowire. Magnetic domains will be used to store information in vertical columns of magnetic material perpendicular to the surface of the silicon wafer as shown in Fig. 1.3. The controlled motion of multiple domains by current is key to this device concept which is essentially a shift register combined with writing and reading elements. If successful, this approach will greatly surpass the density of other solid-state memories [5].

Both the domain wall logic and racetrack memory device concepts store information according to the magnetization direction. Unlike CMOS devices, a semiconducting substrate is not required for these devices. As a result, these concepts enable high density 3D devices that can be fabricated using multiple stacked layers and can utilize space that was previously unusable in standard CMOS devices. These device concepts have the potential to be incorporated into low-power, low-cost portable electronic devices. Magnetic devices have the potential to become the next generation technology beyond CMOS.

1.3 Objective and Overview of Dissertation

In order for domain-wall based technologies to become viable candidates for commercial devices, several challenges involving the dynamics of propagating domain walls must be overcome. $Ni_{0.80}Fe_{0.20}$ (Py, Permalloy) is the most commonly used material to study domain wall dynamics and test domain wall device concepts. However, domain wall dynamics are strongly dependent on material properties. Better understanding of domain wall dynamics will be accomplished through exploring new materials. Materials engineering for enhancing domain wall dynamics is a critical research area that has not been adequately explored. The objective of this work is to study novel magnetic alloys created by doping ferromagnetic materials and evaluate their potential to optimize domain wall propagation and improve domain wall device performance. Throughout this work, the term doping is used as a general term to describe the process of adding impurities to alter material properties.

Chapter 1 has provided the motivation for exploring device concepts that utilize magnetization rather than traditional electronic charge as a new state variable, given examples of proposed magnetic devices and introduced some of the benefits and challenges facing magnetic devices. The next chapter outlines the formation of magnetic domains as a mean to reduce the overall magnetic energy if a ferromagnet. Chapter 2 also explores the dynamics of propagating the transitional regions between domains, referred to as domain walls, by applying either a magnetic field or an electrical current. Chapter 3 examines the way in which the magnetic nanostructures were fabricated including patterning by electron-beam lithography (EBL) and metal deposition techniques including e-beam evaporation and sputtering. Giant magnetoresistance (GMR) measurements are used to determine the orientation of domains and detect the presence of a domain wall within the structures. In Chapter 4, the impact of rare-earth dopants on the magnetic and properties of Ni, Co and Permalloy ferromagnets are demonstrated using superconducting quantum interference device (SQUID) magnetometry and ferromagnetic resonance (FMR) measurements. X-ray diffraction techniques are utilized to determine the effect of rare-earth dopants on the crystallinity of these ferromagnetic materials. Chapter 5 describes the spin wave Doppler technique used to analyze the effect of Gd dopants on current polarization and the non-adiabatic spin transfer velocity in Permalloy nanowires. Domain wall velocity measurements are performed utilizing the magneto-optic Kerr effect (MOKE). Average velocities of propagating domain walls are analyzed as a function of rare-earth concentration with propagation due either to only a magnetic field or also assisted by a current. Finally, current-assisted domain wall depinning MOKE measurements evaluate the effect of rare-earth dopants on non-adiabatic effects in Chapter 6. Finally, a brief summary of the research and direction for future work conclude this dissertation in Chapter 7.

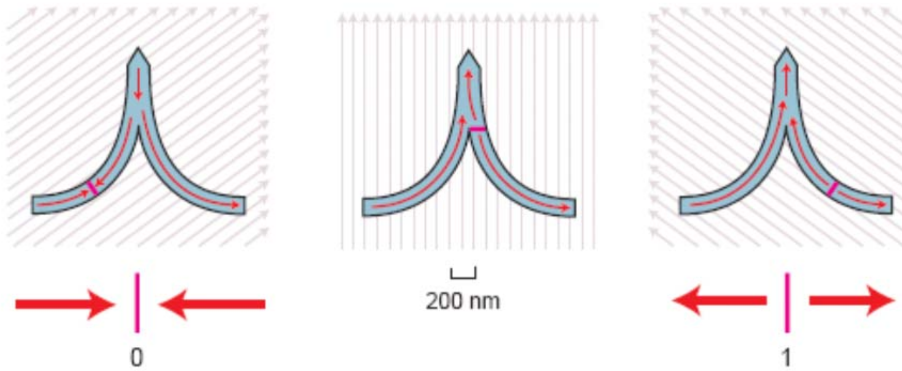

Figure 1.1: Operating concept of the domain-wall logic NOT gate with magnetic field directions shown with arrows in background [8].

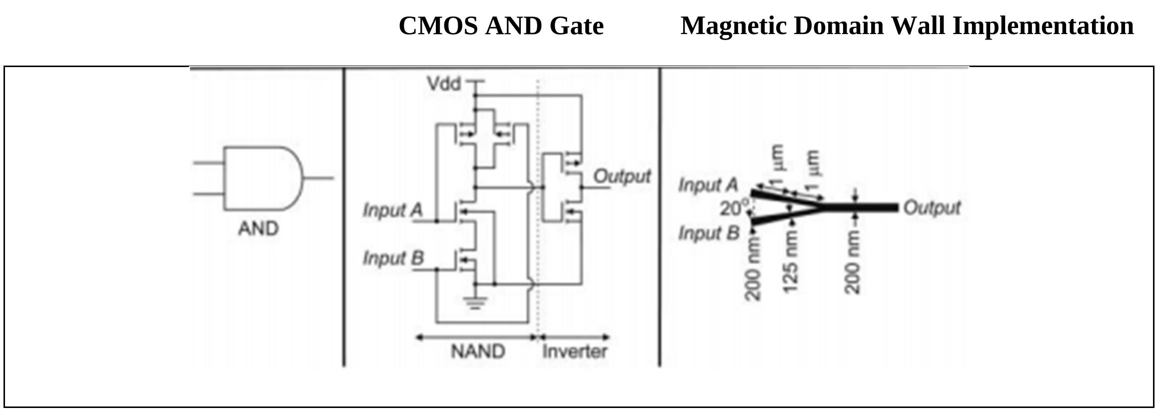

Figure 1.2: Magnetic domain wall logic functions are created by simple, single-layer lithography shown here in comparison with the arrangement of 6 transistors necessary to implement the AND function in CMOS [6].

Table 1.1: The advantages and disadvantages of magnetic logic when compared to CMOS logic devices.

Comparison with CMOS

Advantages	Disadvantages
Simplicity	Power requirements for DW nucleation and propagation?
Scaling potential	Fabrication limitations
Cheaper fabrication	Integration with charge-based electronics
Lower energy per operation [1] 200 nm devices: E ~ 10^{-5} pJ for DW logic vs. 10^{-2} pJ for CMOS 70 nm devices: E ~ $3\text{x}10^{-7}$ pJ for DW logic vs. 10^{-3} pJ for CMOS	Complicated DW propagation processes are not fully understood
Lower power dissipation	Speed?

[1] Energy does not include power to generate magnetic field

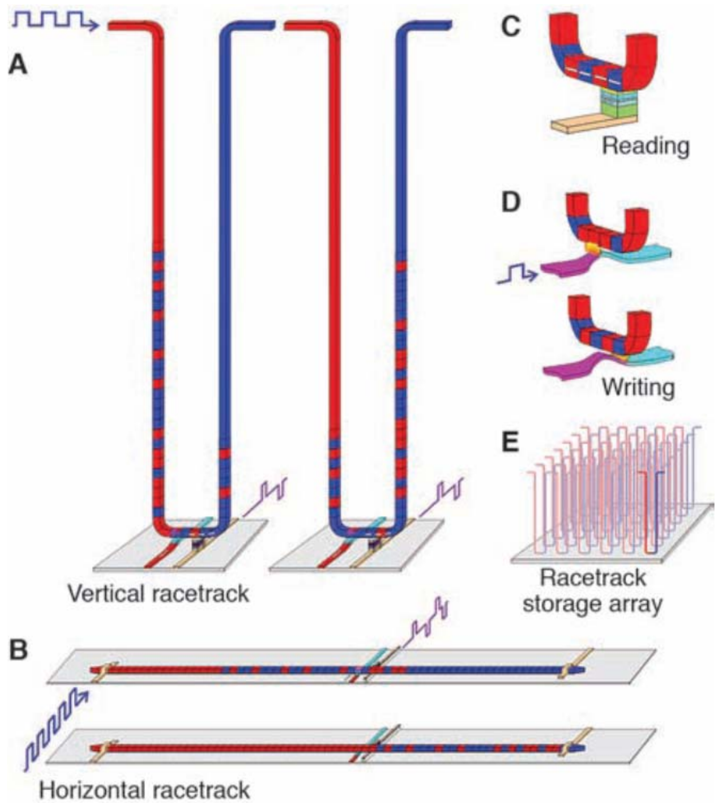

Figure 1.3: Illustration of racetrack memory proposed by IBM implementing current-controlled motion of a series of domain walls through a ferromagnetic nanowire [5].

REFERENCES

[1] V. V. Zhirnov, R. K. Cavin, J. A. Hutchby, and G. I. Bourianoff, "Limits to binary logic switch scaling - A Gedanken model," *Proceedings of the IEEE,* vol. 91, pp. 1934-1939, Nov 2003.

[2] G. Bourianoff, "The future of nanocomputing," *Computer,* vol. 36, pp. 44-53, Aug 2003.

[3] Nobel Foundation, "Discoverers Of Giant Magnetoresistance Used In Hard Drives Win 2007 Nobel Prize In Physics," in *ScienceDaily*, Oct 2007.

[4] A. Hubert and R. Schäfer, *Magnetic Domains : The Analysis of Magnetic Microstructures*. Berlin: Springer, 1998.

[5] S. S. P. Parkin, M. Hayashi, and L. Thomas, "Magnetic domain-wall racetrack memory," *Science,* vol. 320, pp. 190-194, Apr 2008.

[6] D. A. Allwood, G. Xiong, C. C. Faulkner, D. Atkinson, D. Petit, and R. P. Cowburn, "Magnetic domain-wall logic," *Science,* vol. 309, pp. 1688-1692, Sep 2005.

[7] M. Hayashi, L. Thomas, R. Moriya, C. Rettner, and S. S. P. Parkin, "Current-controlled magnetic domain-wall nanowire shift register," *Science,* vol. 320, pp. 209-211, Apr 2008.

[8] A. Cho, "Spintronics - Magnetic gate opens new computing path," *Science,* vol. 296, pp. 1948-1948, Jun 2002.

CHAPTER 2

MAGNETIC DOMAINS AND DYNAMICS

2.1 Domain Walls

Magnetic energy is the combination of several energy terms: anisotropy energy, exchange energy, external field (Zeeman energy), stray field energy and magnetostrictive energy [1]. Anisotropy occurs from spin-orbit interactions and aligns magnetization in a particular lattice direction. Anisotropy energy is minimized when magnetic moments lie along the preferred crystallographic axes. In ferromagnets, it is energetically favorable to align spins in a common direction. When electrons have a parallel magnetization direction, minimal exchange energy occurs. Magnetic field energy can be caused by an external field or be generated by the ferromagnetic material itself in stray field energy. Magnetostrictive energy causes ferromagnetic materials to change their shape or dimension as a response to a magnetic field.

In magnetic domains, the magnetic moments of the atoms are aligned parallel. Domains are formed in ferromagnets to reduce the stray field energy. Since magnetic moments of neighboring domains do not have parallel direction, energy is added at transitions between domains. The wall energy per unit area is equal to $E_w = 4\sqrt{AK}$ where A is the exchange stiffness constant and K is the anisotropy constant [2]. Domains minimize the overall energy in a ferromagnet and will continue to form until the energy to create a domain is larger the energy decrease achieved from the lower stray field energy. In an unmagnetized material, domains are randomly oriented so that the structure has no external magnetization. Domains cause magnetic behavior in ferromagnetic materials because they all align with an applied field and retain magnetization. The magnetic orientation of a domain depends on its effective field caused by external magnetic fields, magnetocrystalline anisotropy, exchange energy and stray fields.

The mobile interfaces separating domains where the magnetization direction continuously rotates from the orientation of one domain to the next are referred to as domain walls. Magnetic wires with large width to thickness ratios yield single domains separated by simple domain wall structures where the shape anisotropy confines the orientation of domains to the long axis of the nanowire. Consequently domain walls in nanowires are 180^o walls that can occur in head-to-head or tail-to-tail configurations. There are two different spin structures domain walls that typically occur in wires. The transverse wall has spins that rotate in the plane of the wire and is described by its chirality, the direction that the magnetization rotates. In a vortex wall, the vortex core points out of the wire plane and spins curl around the vortex core. Vortex walls are characterized both by their chirality and their polarity which is the direction of the core's magnetization [3].

The spin structures of each type of wall in a head-to-head domain wall are shown in Fig. 2.1. Transverse walls have a stray field at the wire boundary but very low exchange energy. More exchange energy is required for a vortex, but the stray field energy is minimized. Consequently, the wire geometry and material determine the preferred type of domain wall where vortex walls are nucleated in thick and wide wires while transverse walls occur in thin and narrow wires. The phase boundary between the two spin structures is determined by comparing the stray energy of a transverse wall with the additional exchange energy due to a vortex and occurs where $wt \approx 60L_{ex}^2$, where L_{ex} is the exchange length [4].

Experimental phase diagrams, such as the one in Fig. 2.2, have verified this theoretical phase boundary.

2.2 Domain Wall Width

The width of the domain wall is determined by the balancing of the exchange and anisotropy energies to minimize the wall energy density. Larger walls are preferred for minimizing exchange energy because the magnetizations between neighboring electrons are similar. However, minimum anisotropy energy is achieved with narrow walls. Domain wall width is difficult to define because domain walls are a continuous transition. This parameter is also difficult to determine because different spin structures are possible. Furthermore, walls with the transverse structure have a triangular profile to reduce energy [5].

The classical and most commonly used definition for wall width was introduced by Lilley and determined as

$$\Delta = \pi\sqrt{A/K} \tag{2.1}$$

with A and K both being material parameters [1]. However, soft materials have low anisotropy energies so the interplay between the exchange and stray field energies determine the domain wall width. The resulting domain wall width for soft magnetic materials is given as

$$\Delta = \sqrt{2A/\mu_0 M_s^2}, \tag{2.2}$$

by Hrkac *et al*. where M_s is the saturation magnetization and μ_0 is the permeability constant [2]. Domain wall widths can range from 1 nm for hard materials to 100 nm for soft materials where typical domain wall widths in Permalloy are around 20 nm. The next section will explain the impact of domain wall width on the interaction between domain walls and both magnetic fields and spin-polarized currents.

2.3 Domain Wall Dynamics

Domain walls behave as quasiparticles that can be manipulated by application of a magnetic field, an injected current or their combination [5]. The domain wall dynamics are defined by the Landau-Lifshitz Gilbert (LLG) equation modified to include the influence of current [6, 7]:

$$\frac{\partial \mathbf{M}}{\partial t} = \gamma\mu_0 \mathbf{H}\times\mathbf{M} + \frac{\alpha}{M_s}\mathbf{M}\times\frac{\partial \mathbf{M}}{\partial t} - (\mathbf{u}\cdot\nabla)\mathbf{M} + \frac{\beta}{M_s}\mathbf{M}\times[(\mathbf{u}\cdot\nabla)\mathbf{M}]. \tag{2.3}$$

The first and second terms on the right describe the effects of an applied magnetic field $\overrightarrow{H}$. The first term describes the precession around the local magnetic field that is analogous to the motion of a spinning top. The gyromagnetic ratio, γ, is the ratio of the magnetic dipole moment to the angular momentum.

Magnetic damping moves the magnetization toward the effective field until vectors are parallel in static solution and is represented by the second term. The amount of damping and the energy dissipated through the process are determined by, α, the Gilbert damping factor. Consequently, materials with a low Gilbert damping factor are desired for domain wall propagation. The precession and damping mechanisms are illustrated in Fig. 2.3. The last two terms of the LLG equation account for the effects of an injected current representing the adiabatic and non-adiabatic spin torques and will be described in the current driven dynamics section.

2.3.1 Magnetic Field Driven Dynamics

A domain wall feels a change in potential due to an applied magnetic field and can transition to an energetically favorable position. Domains with the same orientation as the applied magnetic field expand propagating the domain wall through the wires as shown in Fig. 2.4. The velocity of the domain wall is directly proportional to the magnitude of the applied field below the Walker breakdown point. The domain wall velocity is given by $\mathbf{v_{DW}} = \mu\mathbf{H}$. The mobility is given by $\mu = \left(\Delta\gamma / \alpha \right)$ where Δ is the domain wall width described in the previous section. The behavior above the Walker breakdown point will be described in Section 2.4.

There are several problems that are encountered using magnetic fields to propagate domain walls. One major problem is that head-to-head and tail-to-tail domain walls move in opposite directions within ferromagnetic wires so that neighboring domain walls annihilate each other as shown in the cartoon in Fig. 2.5. A magnetic field generator is also required for these systems which increases the cost and complexity of the system and limits the scalability. Generating a magnetic field is also energy inefficient and increases the total energy of the system.

2.3.2 Current Driven Dynamics

In contrast to magnetic fields, electric currents can be easily generated and precisely controlled. Moving magnetic domains walls with a spin polarized current rather than a magnetic field is expected to eliminate power inefficiencies [8] and complications caused by the direction of motion of neighboring domains [9]. As a result, domain wall propagation by spin-polarized current has become an intense area of research over the past few years and is a key focus of this work. Although current induced domain wall motion was predicted and observed in 1984 [10], lithography techniques which enable reasonable current densities had to be developed for this technique to be feasible. Current traveling through a ferromagnet becomes spin polarized and has spin angular momentum. Current acts to propagate a domain wall by two different mechanisms. Some current-carrying electrons will rotate to follow the local magnetization as when they encounter and travel through a domain wall. A torque is exerted to orient the electron spin with the domain wall and in response an exchange torque is applied to the ferromagnet. Thus the domain wall propagates in the direction of electron flow. This is the adiabatic spin transfer torque and is given by the third term on the right-hand side of the LLG equation where **u** is the velocity caused by the adiabatic spin transfer torque. This term, called the adiabatic spin transfer velocity, is given by

$$\mathbf{u} = \frac{g\mu_B P}{2M_s e}\mathbf{J} \tag{2.4}$$

where g is the Landé factor, μ_B is the Bohr magnetron, P is the current polarization, M_s is the saturation magnetization, e is the (negative) electron charge and $\mathbf{J}$ is the current density [7].

Other current-carrying electrons will not follow the spin orientation adiabatically and will be reflected when they encounter a domain wall. The direction of motion of the electrons reverses and their momentum is transferred to the domain wall resulting in a non-adiabatic spin torque contribution [11]. Their force is analogous to a localized magnetic field at the domain wall. The contribution of this effect is included in the last term of the LLG equation where the non-adiabatic factor β characterizes its strength. The non-adiabatic factor depends on the square of the exchange length, λ_J, to the spin-flip length ratio, λ_{sf}, as shown below [7]:

$$\beta = \left(\frac{\lambda_J}{\lambda_{sf}} \right)^2 . \tag{2.5}$$

A cartoon illustrating the adiabatic and non-adiabatic spin torque contributions is shown in Fig. 2.6.

In simple models, the current-driven domain wall velocity $\mathbf{v_{DW}}$ below Walker breakdown is proportional to $\mathbf{u}\,\beta/\alpha$ [7, 12]. The critical current required to depin a domain wall from a potential well is inversely proportional to the β/α ratio and the strength of the spin transfer velocity. This value is determined by

$$j_{th} = \frac{\mu H_p}{\left({}^{\beta}/_{\alpha} \right) \eta} \tag{2.6}$$

where μ is the magnetic field mobility, H_p is the effective pinning field and η is the torque associated with the adiabatic spin transfer and is given as $\eta = {}^{\mathbf{u}}/_{\mathbf{J}}$ [4].

2.4 Walker Breakdown

It is well known that two distinct regimes exist with regard to the domain wall velocity as a function of the driving force. The transition between these two regimes is referred to as the Walker breakdown point. With increasing velocity, the canting angle of the domain wall increases due to the demagnetizing field. The canting of the domain wall adds stray field energy and increases the anisotropy constant resulting in an increase to the domain wall energy. As a result, the domain wall structure alternates between states and the instantaneous velocity changes direction. Above the Walker breakdown point, the wall exhibits oscillatory forward and backward motion as shown in Fig. 2.6. Far above Walker breakdown the periodic torque terms average out yielding another linear velocity regime but with significantly reduced mobility. Walker breakdown occurs with both magnetic field driven and current induced wall motion.

Far above Walker breakdown, the average velocity of a field driven domain wall is $\langle v \rangle = \alpha^2 \mu H$. For current driven domain wall motion, the average velocity approaches the spin transfer velocity, **u** because the adiabatic term dominates far above Walker breakdown. It is beneficial to delay the onset of Walker breakdown in order to retain high mobility and greater efficiency in domain wall dynamics. The magnetic field at which Walker breakdown occurs is given by

$$H_w = \frac{\alpha H_k}{2} \tag{2.7}$$

where H_k is the anisotropy field which is proportional to M_s [4]. Precession of the domain wall due to an applied current occurs at the Walker current density,

$$J_w = \frac{2eM_s\gamma\Delta}{g\mu_B P\alpha}\frac{1}{(1 - {}^{\beta}/_{\alpha})}. \tag{2.8}$$

Experimental evidence of Walker breakdown for both magnetic field driven and current induced wall motion is shown in Fig. 2.7.

There are several methods that have been proposed or demonstrated to delay the onset of Walker breakdown by improving the stability of domain walls and preventing transformations. One method involves using a transverse magnetic field that helps stabilize the domain wall. Bryan *et al.* demonstrates that the Walker threshold field is dependent on the transverse field [13]. However, the impact of the transverse field is also dependent on its direction compared to the wall magnetization. Additionally, this technique requires multiple magnetic field generation which is energetically inefficient and causes scaling problems. Modulating magnetic parameters could contribute to a delay the onset of Walker breakdown. Moore *et al.* show that by tuning the Gilbert damping parameter through Ho doping Walker breakdown is delayed with magnetic field induced propagation [14].

2.5 Challenges in Domain Wall Motion

The majority of research on domain wall devices has been performed using Permalloy wires. However, current induced domain wall motion through Permalloy exhibits low domain wall velocities and require high critical current densities to initiate motion [15-17]. Because the operation speeds of domain wall devices are directly related to the domain wall velocities, faster propagation is desired for potential applications. The very high threshold currents required to initiate domain wall motion in Permalloy wires are on the order of 10^{12} A/m^2. These current densities approach the point where failure will occur due to electromigration effects and must be reduced to eliminate this possible failure mode and reduce the power consumption of domain wall devices.

Although non-adiabatic effects are a key factor of domain wall dynamics, they are not well understood. Theory predicts that the non-adiabatic effects are dependent on domain wall width. Non-adiabatic effects are predicted to be very small for wide domain walls but large in narrow domain walls due to the large magnetization gradients [18]. The β/α ratio is key to enhancing domain wall dynamics. Better understanding of the origin of non-adiabatic effects will be accomplished by evaluating the effect of material properties on the non-adiabatic factor and the β/α ratio.

This work addresses the challenges in domain wall motion that are limiting the potential of domain wall device concepts. These challenges include optimizing the domain wall velocity and reducing the critical current density to initiate domain wall motion. Maximizing $\mathbf{v}_{\mathbf{DW}}$ and minimizing j_{th} requires a large value of β, a small value of α, and as indicated by Eq. 2.4, low magnetization and large current polarization. It has been demonstrated the rare-earth dopants can be used to tune the magnetic properties of Permalloy for applications such as magnetic storage technologies [19, 20]. We focus specifically on the effect of doping on the domain wall dynamics of Permalloy.

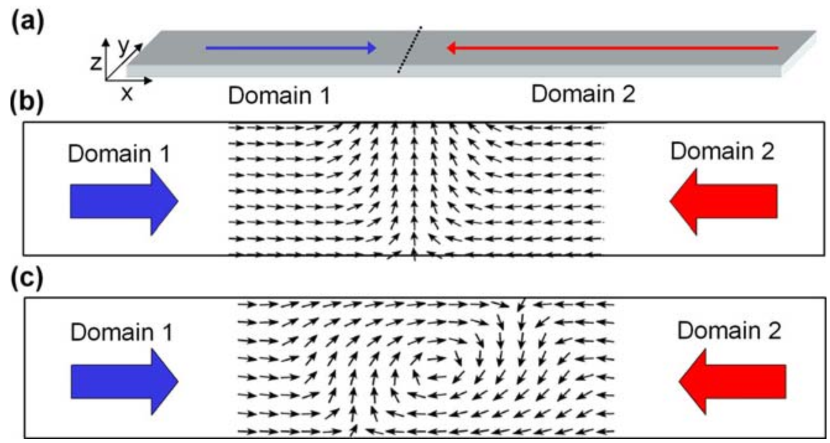

Figure 2.1: 180° head-to-head domain wall in a ferromagnetic wire. Spin structure of a transverse (b) and vortex domain wall (c) [5].

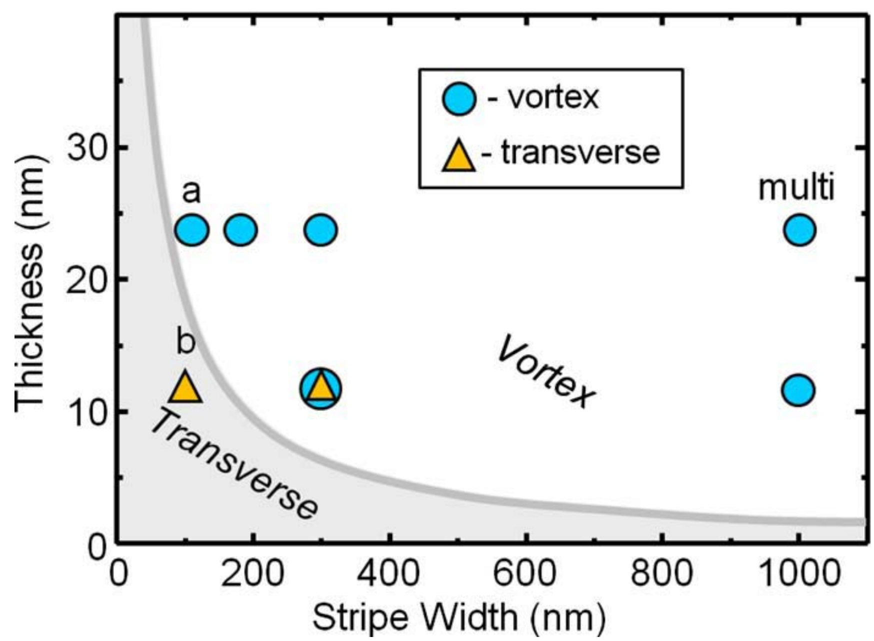

Figure 2.2: Experimental domain wall phase diagram for Permalloy wires. The width and thickness determine the preferred type of domain wall configuration [3].

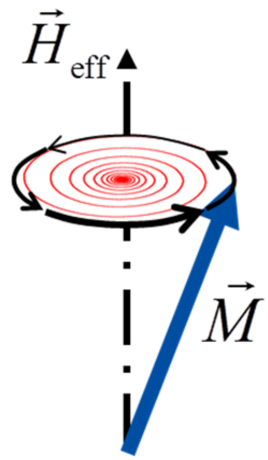

Figure 2.3: Damped magnetization precession that occurs a magnetic field is applied to a ferromagnet.

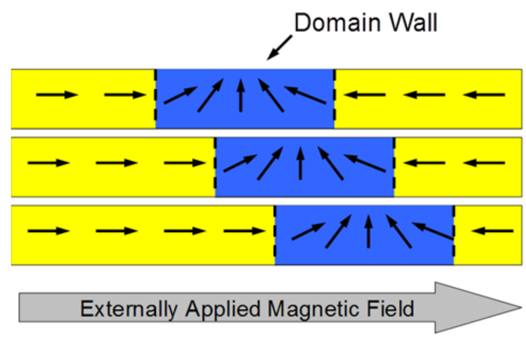

Figure 2.4: Domain wall propagation under an externally applied magnetic field. As the magnetic moments on the left are oriented with the magnetic field, the transition region between domains propagates.

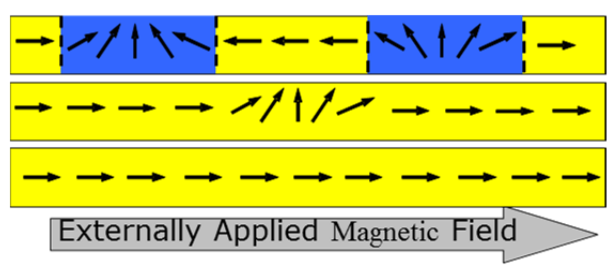

Figure 2.5: Neighboring domain walls in a wire move in opposite directions when a magnetic field is applied resulting in the domain walls colliding and annihilating each other and information loss in a magnetic device.

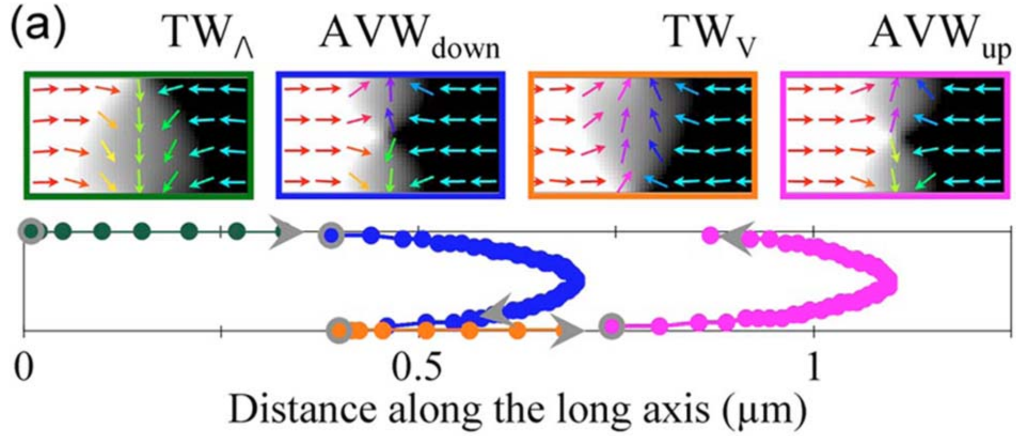

Figure 2.6: Domain wall transformations and oscillatory motion that occurs above Walker breakdown [21].

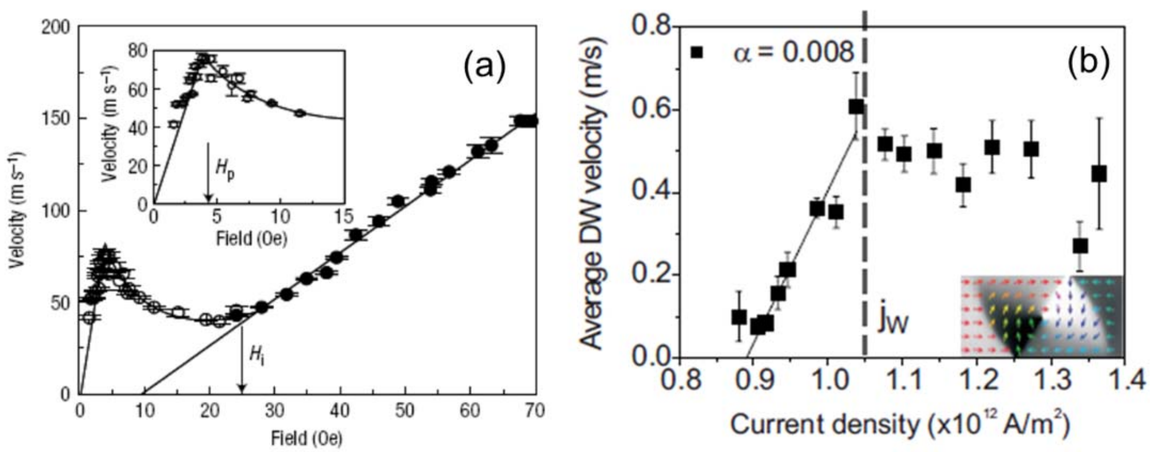

Figure 2.7: Experimental results of average domain wall velocities as a function of applied field [22] (a) and current density [12] (b) through Permalloy wires. Below the Walker thresholds, the solid lines show the linear fits. Linear fits far above Walker breakdown are also shown for the field driven domain walls (a).

REFERENCES

[1] A. Hubert and R. Schäfer, *Magnetic Domains : The Analysis of Magnetic Microstructures*. Berlin: Springer, 1998.

[2] G. Hrkac, J. Dean, and D. A. Allwood, "Nanowire spintronics for storage class memories and logic," *Philosophical Transactions of the Royal Society a-Mathematical Physical and Engineering Sciences,* vol. 369, pp. 3214-3228, Aug 2011.

[3] W. C. Uhlig, M. J. Donahue, D. T. Pierce, and J. Unguris, "Direct imaging of current-driven domain walls in ferromagnetic nanostripes," *Journal of Applied Physics,* vol. 105, 103902, May 2009.

[4] G. S. D. Beach, M. Tsoi, and J. L. Erskine, "Current-induced domain wall motion," *Journal of Magnetism and Magnetic Materials,* vol. 320, pp. 1272-1281, Apr 2008.

[5] M. Klaui, "Head-to-head domain walls in magnetic nanostructures," *Journal of Physics-Condensed Matter,* vol. 20, 313001 Aug 2008.

[6] S. Zhang and Z. Li, "Roles of nonequilibrium conduction electrons on the magnetization dynamics of ferromagnets," *Physical Review Letters,* vol. 93, 127204, Sep 2004.

[7] A. Thiaville, Y. Nakatani, J. Miltat, and Y. Suzuki, "Micromagnetic understanding of current-driven domain wall motion in patterned nanowires," *Europhysics Letters,* vol. 69, pp. 990-996, Mar 2005.

[8] D. A. Allwood, G. Xiong, C. C. Faulkner, D. Atkinson, D. Petit, and R. P. Cowburn, "Magnetic domain-wall logic," *Science,* vol. 309, pp. 1688-1692, Sep 9 2005.

[9] S. S. P. Parkin, M. Hayashi, and L. Thomas, "Magnetic domain-wall racetrack memory," *Science,* vol. 320, pp. 190-194, Apr 2008.

[10] L. Berger, "Exchange interaction between ferromagnetic domain-wall and electric-current in very thin metallic-films," *Journal of Applied Physics,* vol. 55, pp. 1954-1956, Mar 1984.

[11] M. Hayashi, "Current Driven Dyamics of Magnetic Domain Walls in Permalloy Wires," Ph.D dissertation, Dept. Mat. Sci. Eng., Stanford Univ., Stanford, CA, 2006.

[12] T. A. Moore, M. Klaui, L. Heyne, P. Mohrke, D. Backes, J. Rhensius, U. Rudiger, L. J. Heyderman, J. U. Thiele, G. Woltersdorf, C. H. Back, A. F. Rodriguez, F. Nolting, T. O. Mentes, M. A. Nino, A. Locatelli, A. Potenza, H. Marchetto, S. Cavill, and S. S.

Dhesi, "Scaling of spin relaxation and angular momentum dissipation in permalloy nanowires," *Physical Review B,* vol. 80, 132403, Oct 2009.

[13] M. T. Bryan, T. Schrefl, D. Atkinson, and D. A. Allwood, "Magnetic domain wall propagation in nanowires under transverse magnetic fields," *Journal of Applied Physics,* vol. 103, 073906, Apr 2008.

[14] T. A. Moore, P. Mohrke, L. Heyne, A. Kaldun, M. Klaui, D. Backes, J. Rhensius, L. J. Heyderman, J. U. Thiele, G. Woltersdorf, A. F. Rodriguez, F. Nolting, T. O. Mentes, M. A. Nino, A. Locatelli, A. Potenza, H. Marchetto, S. Cavill, and S. S. Dhesi, "Magnetic-field-induced domain-wall motion in permalloy nanowires with modified Gilbert damping," *Physical Review B,* vol. 82, 094445, Sep 2010.

[15] M. Hayashi, L. Thomas, R. Moriya, C. Rettner, and S. S. P. Parkin, "Current-controlled magnetic domain-wall nanowire shift register," *Science,* vol. 320, pp. 209-211, Apr 2008.

[16] M. Klaui, M. Laufenberg, L. Heyne, D. Backes, U. Rudiger, C. A. F. Vaz, J. A. C. Bland, L. J. Heyderman, S. Cherifi, A. Locatelli, T. O. Mentes, and L. Aballe, "Current-induced vortex nucleation and annihilation in vortex domain walls," *Applied Physics Letters,* vol. 88, 232507, Jun 2006.

[17] A. Yamaguchi, T. Ono, S. Nasu, K. Miyake, K. Mibu, and T. Shinjo, "Real-Space Observation of Current-Driven Domain Wall Motion in Submicron Magnetic Wires," *Physical Review Letters,* vol. 92, 077205, Feb 2004.

[18] J. A. Xiao, A. Zangwill, and M. D. Stiles, "Spin-transfer torque for continuously variable magnetization," *Physical Review B,* vol. 73, 054428, Feb 2006.

[19] W. Bailey, P. Kabos, F. Mancoff, and S. Russek, "Control of magnetization dynamics in Ni81Fe19 thin films through the use of rare-earth dopants," *IEEE Transactions on Magnetics,* vol. 37, pp. 1749-1754, Jul 2001.

[20] G. Woltersdorf, M. Kiessling, G. Meyer, J. U. Thiele, and C. H. Back, "Damping by Slow Relaxing Rare Earth Impurities in Ni80Fe20," *Physical Review Letters,* vol. 102, 257602, Jun 2009.

[21] J. Y. Lee, K. S. Lee, and S. K. Kim, "Remarkable enhancement of domain-wall velocity in magnetic nanostripes," *Applied Physics Letters,* vol. 91, 122513, Sep 2007.

[22] G. S. D. Beach, C. Nistor, C. Knutson, M. Tsoi, and J. L. Erskine, "Dynamics of field-driven domain-wall propagation in ferromagnetic nanowires," *Nature Materials,* vol. 4, pp. 741-744, Oct 2005.

CHAPTER 3

MAGNETIC NANOSTRUCTURE FABRICATION AND CHARACTERIZATION METHODS

This chapter provides describes the process for fabricating the patterned magnetic structures used to study domain wall dynamics in this dissertation. Electron beam lithography (EBL) is used to pattern submicron magnetic wires where the width is larger than the thickness to accomplish simple domain wall spin structures. Magnetic thin films are deposited through either e-beam evaporation or RF magnetron sputtering techniques. Details of the optimizing these fabrication techniques that reduce the edge roughness in our nanowires are provided. Giant magnetoresistive stacks are fabricated to analyze the magnetic orientation of the magnetic layers and analyze domain walls within the structures.

3.1 Electron Beam Lithography

Electron beam lithography (EBL) is commonly used to fabricate nanoscale device structures. An electron sensitive resist is patterned by scanning a focused electron beam. This technique surpasses the resolution of optical lithography because exposure is not limited by the wavelength of light. Positive and negative resists are available where the regions exposed to the electron beam can either be removed or maintained. It is a type of maskless lithography which enables pattern modification without the expensive and time-consuming process of creating a mask. This makes EBL convenient for prototypes although the serial nature of the process limits its throughput and reduces potential for commercial devices. EBL also offers precise alignment capabilities.

The EBL system used to fabricate our magnetic nanostructures is manufactured by Elionix and has a 50 keV accelerating voltage and minimum beam diameter of 2 nm that produces a minimum feature size of 10 nm. A field size of 300 μm with 60,000 dots per field resulting in a dot size of 5 nm was chosen. We used the popular positive electron sensitive resist polymethyl methacrylate (PMMA) because it is a high-resolution resist with good adhesion and excellent film characteristics. A bi-layer resist structure is created by spinning a high molecular weight PMMA film on top of a low molecular weight PMMA film. The molecular weight of the resists is determined by the length of PMMA chains. During exposure, the chains undergo scission and dissolve easier in the developer. The PMMA film with a lower molecular weight is more sensitive than the top layer so the resist develops with an undercut that is beneficial for lift-off techniques. Each resist is spun on using a Headway spinner at 500 rpm for 5 seconds followed by 3000 rpm for 40 seconds. A softbake of 180 °C for 2 minutes follows the spin coating for each resist. The thickness of the spun on bilayer resist is approximately 300 nm. This resist structure has well characterized 600 $\mu C/cm^2$ exposure dosage as verified through experiments.

Our patterns are written on 2-inch diameter, p-type silicon wafers. An oxide layer electrically isolates neighboring structures. Structures designed for domain propagation by magnetic field utilize a 50 nm thick thermal oxide. Wafer oxidation is carried out in a Tylan furnace at 950 °C. Because aluminum oxide has better thermal conductivity, devices designed for current induced domain wall motion that must carry large current densities are fabricated on wafers coated with 50 nm of Al_2O_3 using atomic layer deposition. The ALD process to deposit these oxides uses Trimethyl Aluminum (TMA) and H2O as reaction precursors in a Savanah S100 system from Cambridge Nanotech.

In addition to the sub-micron magnetic wires, non-magnetic electrical contact wires and pads are necessary to apply currents through the wires and enable resistance measurements in spin valve structures. The device pattern layouts are designed using AutoCAD. The magnetic wires have drawn thicknesses varying from 150 nm to 1 μm and lengths from 40 μm up to 1 mm in some test structures. Contact wires are comparatively much larger with 3 μm widths and length scales on the order of hundreds of microns. Contact pads are 80-100 μm^2 so that they can easily be probed. Due to the different size scales and importance of lithography resolution in the different features of the patterns, they were split into three separate files that were written with different beam currents and exposure times. An example of a device pattern layout including all three pattern layers is shown in Fig. 3.1. The sub-micron magnetic wires are shown in red while the contact wires and pads are shown in green and blue. The gray boxes indicate the 300 μm fields that are written without moving the stage. The pattern layouts must then be converted to the EBL CAD software to be written.

Two separate aligned layers of EBL are used to pattern the devices since the magnetic nanowires and electrical contacts must be fabricated from different materials. Alignment marks must be patterned with the first layer so that alignment can be performed. Two sets of the alignment marks, each with two 5 μm squares touching at one corner, are patterned vertically with spacing of 23 mm. Large fiduciary marks near the alignment marks are patterned because they are easier to locate with the scanning electron microscopy (SEM) capabilities of the EBL system. The first lithography layer defines the magnetic nanowires and alignment marks. To optimize the resolution of this lithography process and achieve the appropriate dosage, an electron beam current of 50 pA exposes each 5 μm dot for 3 μs. The PMMA resist is developed in a solution of methyl isobutyl ketone (MIBK) and isopropanol alcohol (IPA) with a ratio of 1:3 for 140 seconds. Residual resist is removed by ashing in an Emitech RF plasma asher at 90 W for 45 seconds. Magnetic materials are then deposited by electron-beam (e-beam) evaporation or sputtering. More details of the magnetic material deposition are provided in the next section. After completing lift-off in acetone, the second lithography layer with contact wires and pads can be patterned.

Before spinning on the resist bilayer for the second lithography layer, the alignment marks are covered with Kapton tape. The alignment marks consisting of only a thin layer of magnetic material are difficult to view in the SEM when covered in resist. Registration marks are placed on the CAD software corresponding to the positions of the alignment marks patterned on the wafer. Before the EBL systems exposes the device patterns, the alignment marks are manually located. Beam currents of 400 pA and 1.6 nA write the contact wire layer and the contact pad layer. These layers are written and deposited together because they are made of the same materials but varying the beam current reduces the exposure times and optimizes the patterning speed for these much larger structures. The nonmagnetic contacts are then created by e-beam evaporation and liftoff techniques. The EBL process for the magnetic wires and electrical contacts are outlined by Fig. 3.2 and Fig. 3.3 respectively. Straight and curved nanowires along with various other geometries that have demonstrated potential as domain wall logic operations [1] have been fabricated and examples of these structures are shown in Fig 3.4.

3.2 Magnetic Material Deposition

E-beam evaporation utilizes the energy from an electron beam to melt and evaporate a material contained in a crucible. Deposition rates can be easily adjusted by changing the current and energy of the electron beam [2]. Film thicknesses and deposition rates are determined in the systems used by a quartz crystal. Our e-beam evaporator capabilities allow deposition of up to five different materials *in situ*. Deposition of multiple materials is necessary because capping layers are required to prevent oxidation of magnetic metals. Multiple layers are also necessary to create spin valve structure which can be used to determine the presence and position of a domain wall as described in the next section. E-beam evaporation is a very directional process and consequently is good for lift-off applications. However, one of the limitations of e-beam evaporation is that it is difficult to deposit an alloy because the vapor pressures of the materials are not the same.

As a result, the co-sputtering method is utilized to deposit our magnetic alloys. Sputtering occurs when energetic ions bombard a target with enough energy to eject target electrons. Our films were deposited using a cluster flange integrating three magnetron sputtering sources that use radio-frequency (RF) energy sources. With three sources, multiple layers can be deposited and multiple targets can be deposited simultaneously. The sources are tilted toward the substrate so all sources are incident on the rotating substrates and achieve good uniformity across the substrate wafer. During co-sputtering two targets are sputtered simultaneously and different alloy compositions are obtained by adjusting the relative RF power applied to each source.

The base pressure of the ultra-high vacuum sputter chamber is kept below 5×10^{-8} Torr. The deposition rates of the individual sputtering sources were determined at 100W using a Dektak profilometer to measure the film heights. Fig. 3.5 illustrates the small thickness variation that occurs across a 4” wafer as measured through profilometry. The largest measured variations were ±5% from the average thickness values. In general, the films are slightly thinner towards the 4” wafer edges and show some oscillations in thickness from wafer edge to wafer edge. The measured uncertainty in thickness is typical for sputtering processes.

Because sputter deposition provides a more conformal coating, liftoff can be more challenging. The resist must have a well undercut or retrograde profile to accomplish good liftoff. Otherwise, material can be deposited on the sidewalls of the resist as a result of the isotropic sputter deposition. After liftoff, the extra material on the resist sidewalls will remain on the edges of the nanowires. Close examination of our sputtered nanowires using SEM has revealed problems with edge roughness in our structures (Fig. 3.6). Domain wall propagation through magnetic nanowires is very sensitive to edge defects which create large pinning potentials. Imperfections within nanowires cause domain wall to get pinned and require higher magnetic fields or current densities for depinning.

3.3 Optimization of Magnetic Nanostructure Fabrication

Initially, sonication was used in an effort to help remove the extra material on the sides of our nanowires. However, as illustrated in Fig. 3.7, sonication did not remove the material but resulted in the material on the edges curling up over the wire. While this technique did not improve our structures, it enabled us to conclude that the extra material was in fact attached to our structures and caused by an inadequate resist profile. A cartoon of the probable structure of this initial resist profile is shown in Fig. 3.8. To improve the structures after sputtering and liftoff, improvement of this resist profile is necessary. The top layer of PMMA must provide sufficient overhang to avoid deposition on the sidewalls of the bottom layer of PMMA.

Undercut is defined as the distance between the edge of the top-layer resist pattern and the edge of the bottom layer of the resist where it comes in contact with the substrate. In an attempt to increase the undercut of the resist profile, we increased the exposure and development times. While this technique will likely increase the overall width of our structures, the bottom layer of PMMA should be more effected because it is the more sensitive layer. The exposure time for the 50 pA, 5 nm beam spot was increased from 3.0 μs to 3.25 μs and 3.50 μs. As a result, the exposure dosage increases from 600 $\mu C/cm^2$ to 650 $\mu C/cm^2$ and 700 $\mu C/cm^2$ respectively. The development time in the MIBK:IPA (1:3) solution was increased by 11%. However, as shown in Fig. 3.9, these structures showed similar problems with extra material on the wire edges.

3.3.1 Lift-Off Resist

One popular method to improve lift-off processing involves using lift-off resist (LOR) under a resist layer. LOR resists are based on polymethylglutarimide (PMGI) and manufactured by MicroChem. When using LOR in a bilayer process, the undercut can be controlled by adjusting a variety of parameters such as the softbake temperature and time, the developer and development time and the type of resin composition. LOR is compatible with e-beam resists and LOR/PMMA bilayer structures have been incorporated to achieve high resolution patterns with e-beam lithography [3]. It is important to control both the amount of undercut and also the height of the undercut.

To accomplish an undercut sufficiently large to promote liftoff and minimize deposition on resist sidewalls, we replaced the lower molecular weight PMMA with LOR 2A. The thicknesses of these resists are similar after spin coating. The spin conditions for the LOR are modified slightly with an initial spin of 500 rpm for 5 seconds being followed by a spin at 4000 rpm for 35 seconds. The LOR is then soft baked at 180 °C which is near its glass transition temperature for 5 minutes to produce a slower undercut rate. The top layer of PMMA is coated and soft baked as before.

The exposure dose of the new resist structure had to be optimized. Wires were written using a 50 pA beam current with exposure times from 1.5 μs to 3.0 μs in increments of 0.5 μs. The exposure dose of these wires varies from 300-600 $\mu C/cm^2$. SEM images of the resist patterns for 500 nm wire widths of each exposure dosage after development are shown in Fig. 3.10. An extra step is added to the development procedure to develop the LOR. The development time in MIBK:IPA (1:3) is slightly reduced to 120 seconds. Then, the LOR is developed in MF-319 photoresist developer. The lowest exposure dose failed to clear away all the resist in the exposed regions. The lower exposure dosages did not resolve thinner wires. As a result, the optimized exposure dose for the LOR/PMMA bilayer is 600 $\mu C/cm^2$ since wire widths down to 50 nm can be resolved.

The development time had to be adjusted to achieve an appropriate undercut resist profile. Initially, the LOR was developed for 60 seconds in MF-319 resist developer. After sputtering and liftoff in N-methyl-2-pyrolidone (NMP), variations in metal thickness across the wire width were observed as shown in the cross-sectional SEM images in Fig. 3.11. The thickest regions occur on the wire edges and in the center of the wires and indicate that the resist profile is still flawed. Cross-sectional SEM images of the resist profile in Fig. 3.12 reveal that the resist undercut is much greater than the wire width and far too large. Because of this large undercut, the top PMMA layer buckled when the wafer was cleaved for imaging. When the wafer was not cleaved, the large undercut causes the top PMMA layer to collapse onto the substrate and part of the wire is shadowed by the resist. This results in the thick section along the center of the nanowire. Material deposits on the vertical sidewalls of the collapsed resist leaving thick wire edges.

To reduce the undercut of the LOR layer, the development time was drastically reduced. The resist profile for the LOR-PMMA bilayer were the LOR was developed for only 10s in MF-319 resist developer is shown in Fig. 3.13. The undercut for the reduced development time is ~150 nm. This undercut is adequate to promote liftoff while preventing the resist structure from collapsing. Wires with smooth edges, as shown in Fig. 3.14, were deposited via sputtering using the LOR/PMMA bilayer resist with optimal exposure dosage and development time.

3.3.2 Focused Ion Beam milling

Several of the challenges involved in fabricating submicron structures using the additive technique of liftoff have been described. Many of these challenges can be overcome by using subtractive fabrication processes such as etching or milling. The best quality nanoscale magnetic devices reported have been fabricated using subtractive methods. For example, Malinowski *et al.* found that using an Ar ion milling process with EBL rather than the conventional lift-off technique results in very low edge roughness and decreases the pinning field by a factor of five [4]. Focused ion beam (FIB) milling is another subtractive fabrication process that has been successfully utilized to create magnetic nanostructures [5]. FIB systems are similar to EBL systems except an ion beam is focused rather than an electron beam and atoms are removed from the substrate because ions are larger and heavier than electrons. Although this process results in some ion implantation to the structures due to the ion source, high quality magnetic nanostructures with good magnetic properties have been fabricated using this technique [5].

To further reduce edge pinning, we used a focused ion beam (FIB) system to mill wire edges. We use an FEI Quanta 200 3D DualBeam that incorporates both an electron and ion beam column so that defined patterns can be milled and imaged. This system uses a gallium liquid metal ion source operated at 30kV accelerating voltage with a 30 pA beam current. FIB milling was completed after the first layer of EBL. Before milling, the ferromagnetic wires were 40 μm long and ~700 nm wide. Both sides of the wire were milled to minimize edge defects and the resulting wire width is ~550 nm. By defining the distance between the two parallel milling regions, the wire width remains constant. The milling process had to be precisely configured to avoid etching all the way through the Al_2O_3 insulating layer on the substrates. The substrates also had to be carefully aligned in the system because the milling region length was 30 μm and a small angle difference resulted in a large drift across this length. Images of the magnetic wires whose edges have been milled using this process are shown in Fig. 3.15.

To analyze the effectiveness of this FIB milling process we compared the pinning field from a wire with edges milled by FIB with a wire of approximately the same width that prepared only with lift-off. In order to measure the domain wall pinning field, a domain wall has to be nucleated within the wire. Applying a current through a metal contact generates a localized magnetic field in its proximity. This magnetic field can be large enough that it will alter the magnetization of a magnetic wire under the contact to create a domain wall. An example of the devices consisting of a gold contact line for domain wall nucleation utilized for these measurements and for the MOKE measurements described in Chapter 6 is shown in Fig. 3.16.

Hysteresis loops are obtained using the longitudinal MOKE set-up which is described in more detail in Chapter 6. A short voltage pulse across the metal contact nucleates a domain wall that is propagated through the wire with a magnetic field oriented to the left represented as a negative magnetic field in the hysteresis loops shown in Fig. 3.17. The magnetic field required for depinning the domain wall is smaller for the wire that utilized FIB milling to reduce edge roughness. However, the pinning field only decreases by about 30% indicating that the lift-off procedure using the LOR/PMMA bilayer structure already has low edge roughness.

The coercivity of the wires and the strength of the Kerr signal are also obtained from the hysteresis loops. Coercivity is the field strength required to reduce the magnetization of the material to zero after its magnetization has been saturated. The amplitude of the Kerr signal is directly proportional to the sample's magnetization and decreases significantly for the milled wire. This decrease can be attributed to the ion implantation due to the Gallium ion source at the nanowire edges resulting in a smaller effective magnetic wire width. Reduced wire thickness due to the Gaussian profile of the ion beam may also contribute to the decrease in wire magnetization. The large decrease of the Kerr signal amplitude observed due to the FIB milling process will be detrimental to the MOKE measurements. The FIB milling process is not necessary in our structures because the LOR/PMMA bilayer structure already has low edge roughness and a low pinning field. The modest improvement in the pinning field achieved by FIB milling is not sufficient to justify the difficulty that is added to the measurements due to the decreased Kerr signal.

3.4 Characterization Methods

3.4.1 Giant Magnetoresistance

Giant magnetoresistance (GMR) is observed when magnetic layers are separated by a conducting layer. The electrical resistance of a GMR stack changes based on the alignment of its magnetic layers. Magnets can be classified as either hard magnets or soft magnets based on their coercivity. By using one hard magnet and one soft magnet for the magnetic layers, a pseudo-spin valve is formed where the alignment of the magnetic layers can be configured based on the magnitude of the applied magnetic field.

When the magnetic layers are aligned parallel there is little scattering and lower resistance while antiparallel alignment increases the scattering and consequently increases the resistance of the stack. The presence and position of a domain wall can be determined by measuring the impedance of the spin valve. A wire containing a domain wall has a higher resistance than one without a domain wall because the ferromagnetic layers of the multilayer stack are aligned antiparallel in a portion of the wire. The magnetoresistance ratio is $\frac{R_{AP}-R_p}{R_{AP}}$

where R_{AP} and R_P are the antiparallel and parallel resistances respectively. GMR structures have relatively small magnetoresistances when compared to magnetic tunnel junctions that use an insulator rather than a conductor between the two magnetic layers. However, GMR stacks are much easier to fabricate and provide an accurate technique to analyze domain wall positioning.

GMR multilayer wires enabled the first quantitative measurements of domain wall velocities propagated by a magnetic field in 1999 at low temperature (77 K) [6]. A DC current can propagate a domain wall through the soft layer of a spin-valve and therefore switch the magnetic configuration of the GMR stack. This technique can be used to determine the current density required to initiate domain wall motion in the Permalloy free layer of the GMR spin valve [7]. Domain wall pinning and depinning mechanisms due to both a magnetic field and an electric current have also been studied in various spin valve geometries including three-terminal Y junctions [8] and notched bars [9].

Using the method described in the section 3.1, GMR multilayer nanowires were created. The stacks of Co(8 nm)/Cu(4 nm)/Permalloy(4 nm)/Au(4 nm) were deposited *in situ* by e-beam evaporation. The magnetoresistance ratios of the devices are measured using a four point technique. Using an HP4155b current meter, a current swept from -20 μA to +20 μA is passed through the two outermost contacts. The voltage drop is measured across two of the remaining contacts as shown in Fig. 3.18. The measurements are made in the SpinField 2D Magnetic Field platform (Fig. 3.19). Magnetic fields up to ~300 Oe can be generated along orthogonal axes in the plane of the sample by electromagnets. Each pair of electromagnets are powered by a KEPCO BOP 50-2M power supply. The magnetic platform also measures the field strength with integrated magnetic field sensors for each axis.

These measurements have been automated using a National Instruments data acquisition (DAQ) device and software written in Visual Basic. The program performs four-point measurements during each interval of an applied magnetic field which can be swept from a user-defined initiate field to a maximum field in increments that are also defined. However, many measurements at small increments yielded in too much heating in the wires and changes to the wires resistance. The program also displays plots of the measured data as shown in Fig. 3.20.

A magnetic field of 300 Oe is first applied to saturate the wire's magnetization and align the free layer and fixed layer parallel to each other. Using this condition, the resistance of the parallel state of the spin stack is measured. The magnetic field is then reduced and incrementally applied in the opposite direction. Resistance measurements are obtained for each field value. The soft Permalloy layer switches with a very small applied field increasing the resistance due to the antiparallel alignment of the two magnetic layers. The magnetization of the two layers remain opposite until the applied field is large enough to flip the magnetization of the hard Co layer. The distinct resistance states of the GMR stacks are seen in Fig. 3.21 along with the corresponding alignment of the ferromagnetic layers shown in the cartoon on the right.

For the cusp-shaped nanowire, an intermediate resistance state occurs because the domain wall gets pinned at the cusp in the hard Co layer as shown on the left in Fig. 3.22. Here a second switching step occurs with a slightly larger applied field demonstrating the domain wall depins and the free layer and fixed layer of the GMR structure are once again aligned parallel. Fig. 3.22 is a cartoon illustrating the magnetic configuration of the GMR stack including pinning that occurs at the fabricated cusp.

3.4.2 Other Characterization Techniques

Other characterization techniques used throughout this work include X-ray diffraction measurements, superconducting quantum interference device (SQUID) magnetometry, Ferromagnetic resonance (FMR) measurements, spin wave Doppler measurements and measurements of the magneto-optical Kerr effect. Details of these characterization techniques and their usages are addressed in subsequent chapters of this dissertation.

3.5 Summary

The novel magnetic alloys of interest in this study are deposited through co-sputtering using an RF magnetron sputter tool. Submicron magnetic wires and larger metallic contacts are fabricated using two aligned layers of EBL and lift-off techniques. Due to the conformal coating of the sputter deposition process, the electron sensitive resist profile had to be optimized to minimize metal deposition on resist sidewalls and the resulting edge roughness in the magnetic structures. A bilayer resist structure incorporating a lift-off resist provides sufficient undercut and yields magnetic wires with low edge roughness. GMR stacks were also fabricated and their magnetoresistive behavior was verified by manipulating the alignment of their magnetic layers by application of a magnetic field. These magnetic wires will be utilized to study domain wall dynamics in this dissertation.

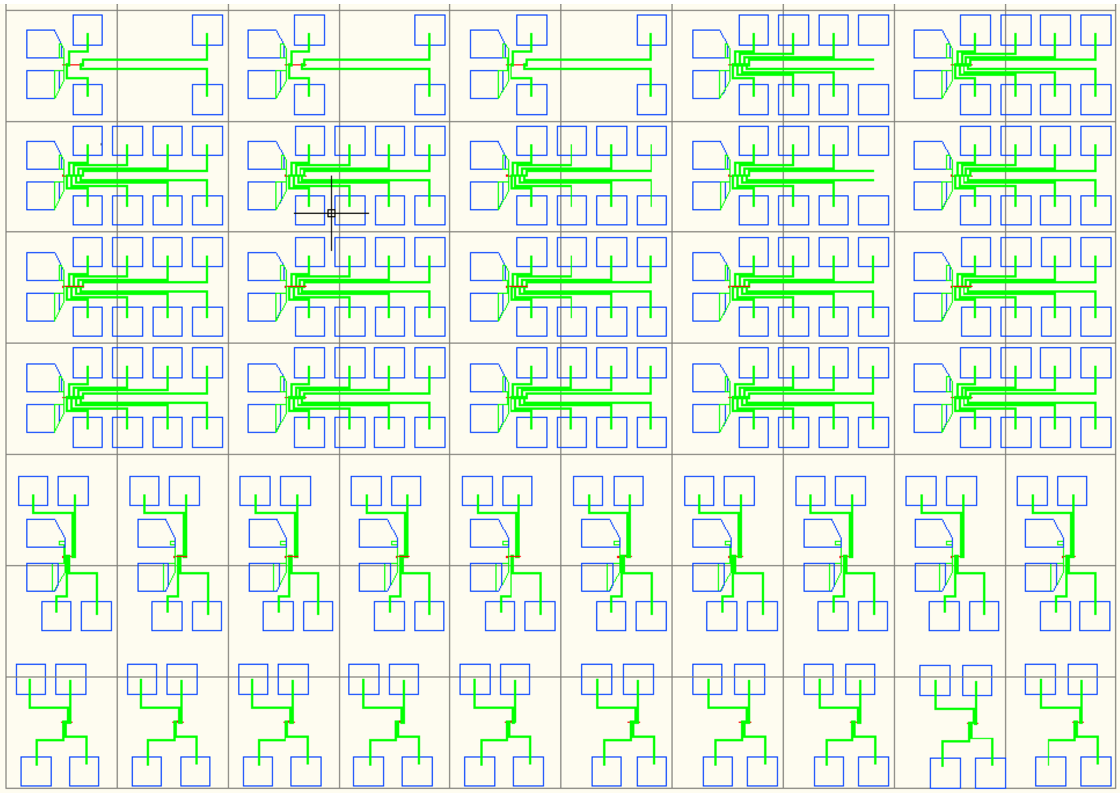

Figure 3.1: Device pattern layout designed in AutoCAD. The sub-micron magnetic wires are shown horizontally in red. The green wires show the 3 μm wide contact wires while the contact pads that are probed are shown in blue. The 300 μm fields are shown by the gray boxes.

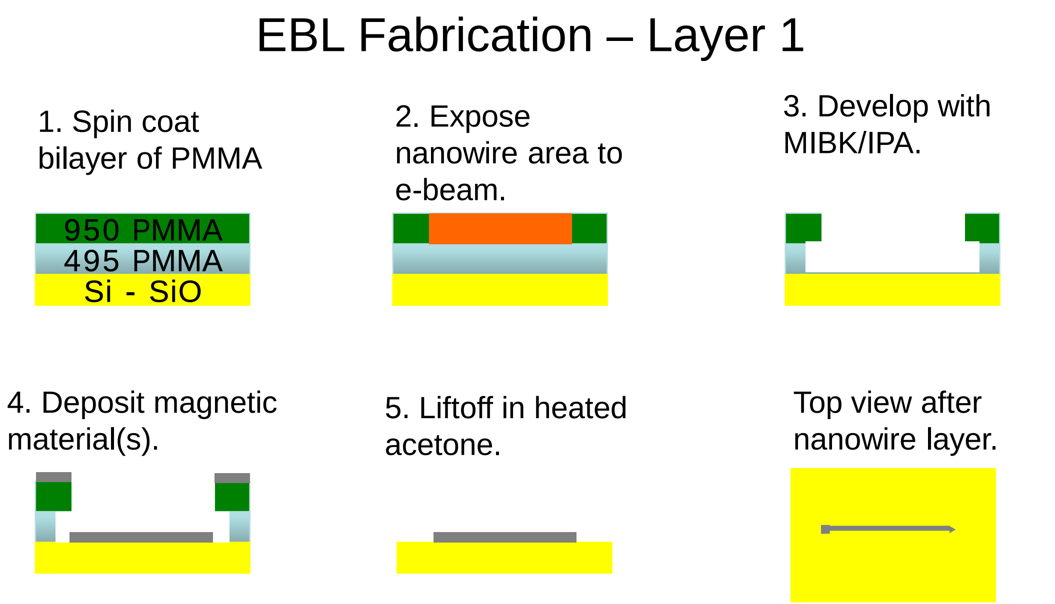

Figure 3.2: EBL process to pattern magnetic nanowires using a bi-layer resist structure.

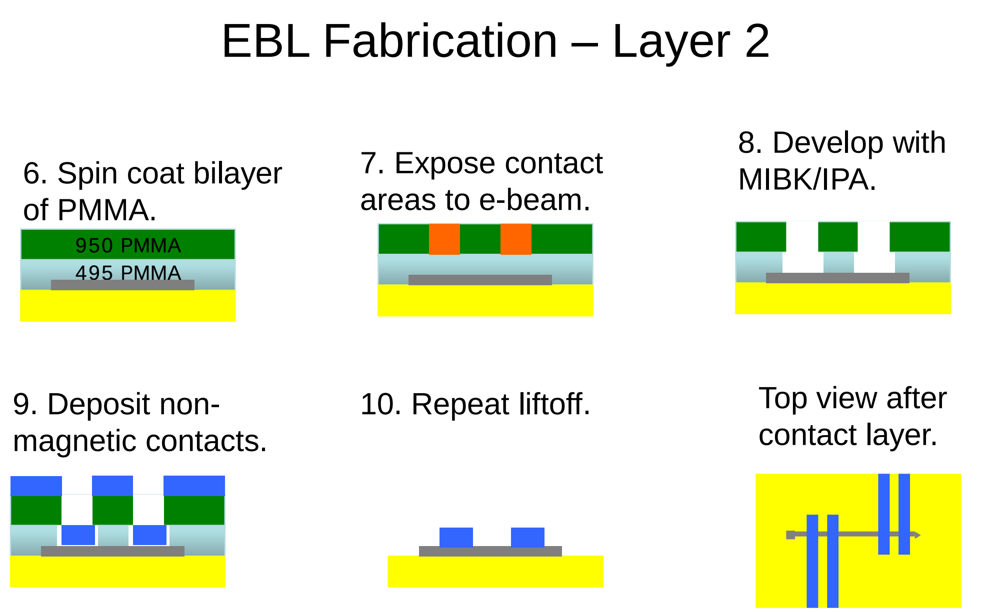

Figure 3.3: EBL process to pattern large electrical contacts for magnetic nanowires.

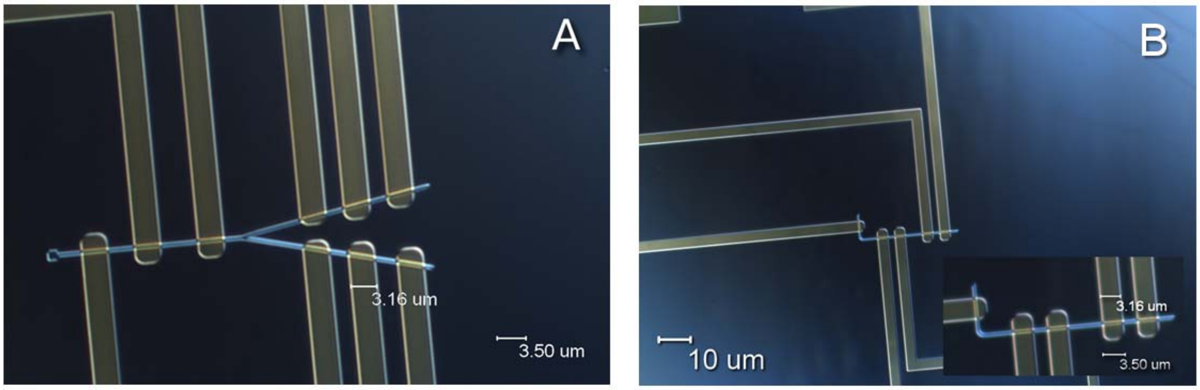

Figure 3.4: Optical microscope images of fabricated magnetic nanowires with electrical contacts.

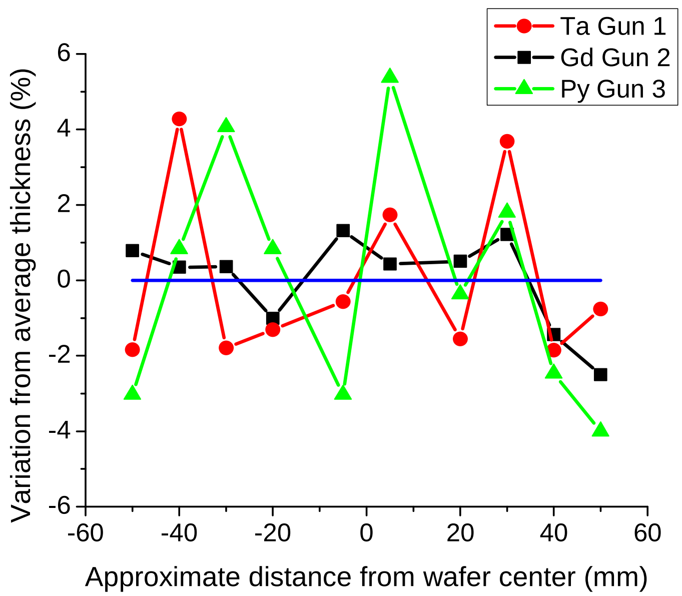

Figure 3.5: Variation in thickness across a 4” wafer as measured by profilometry. Maximum variation is ±5%.

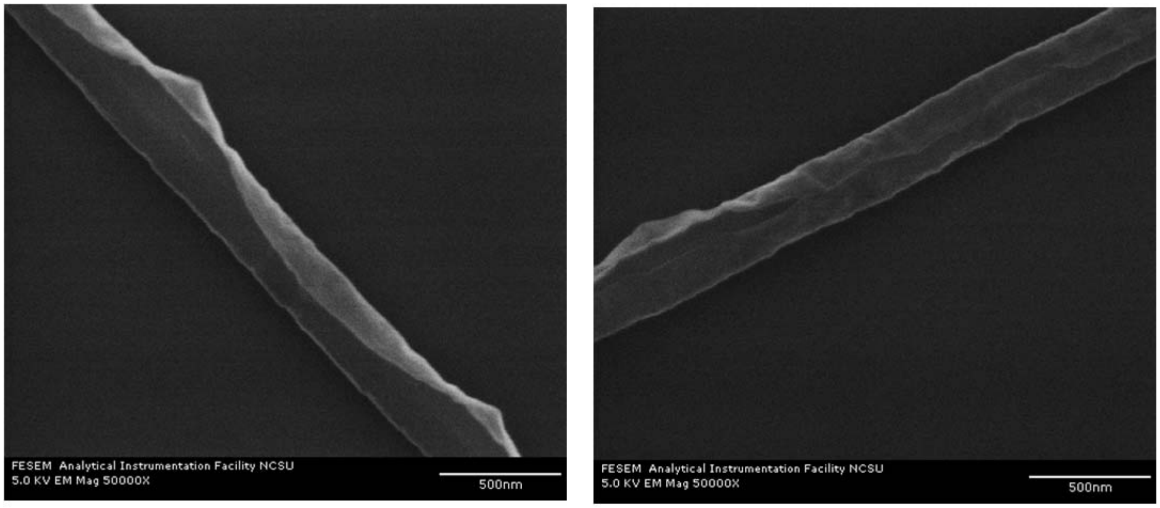

Figure 3.6: SEM images of nanowires deposited via sputtering showing extra material remaining on the edges of nanowires after liftoff.

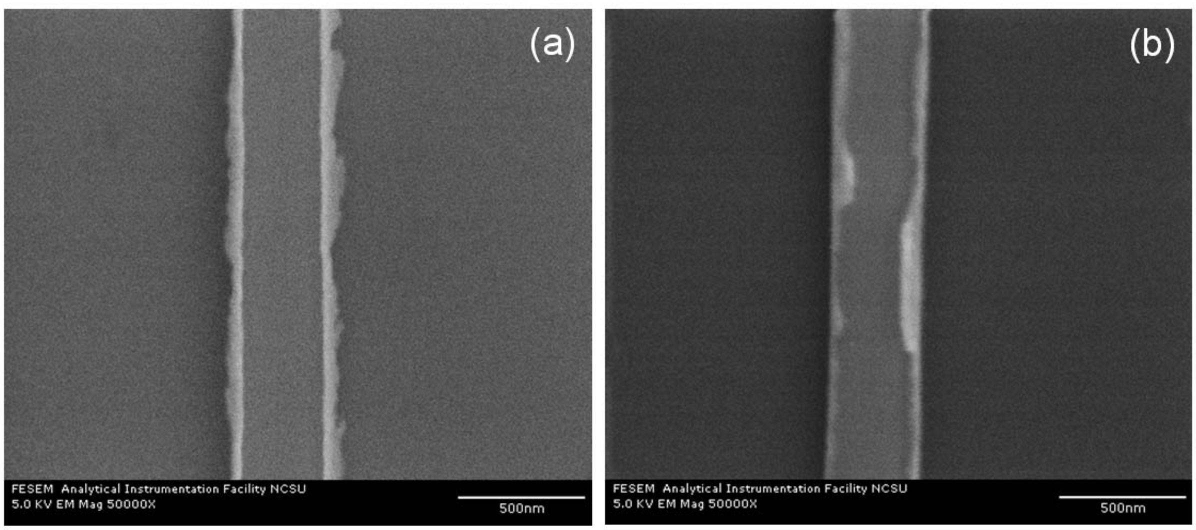

Figure 3.7: SEM images showing magnetic alloys structures deposited by co-sputtering (a) as deposited and (b) after sonication.

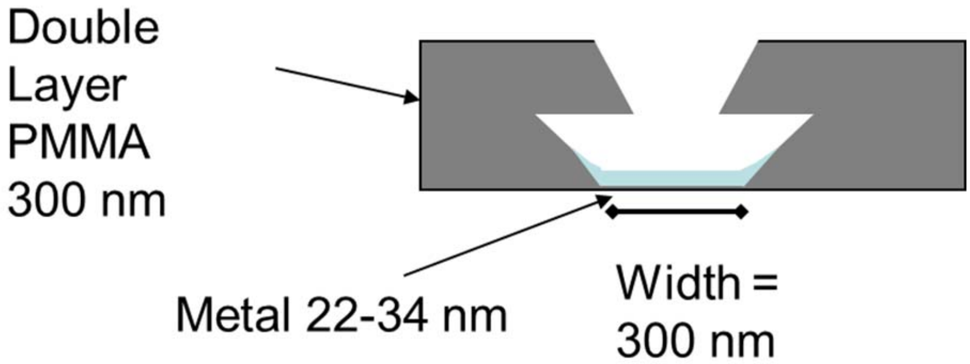

Figure 3.8: Resist profile for bilayer PMMA process. Insufficient undercut combined with conformal coating by sputtering results in metal deposition on resist sidewalls.

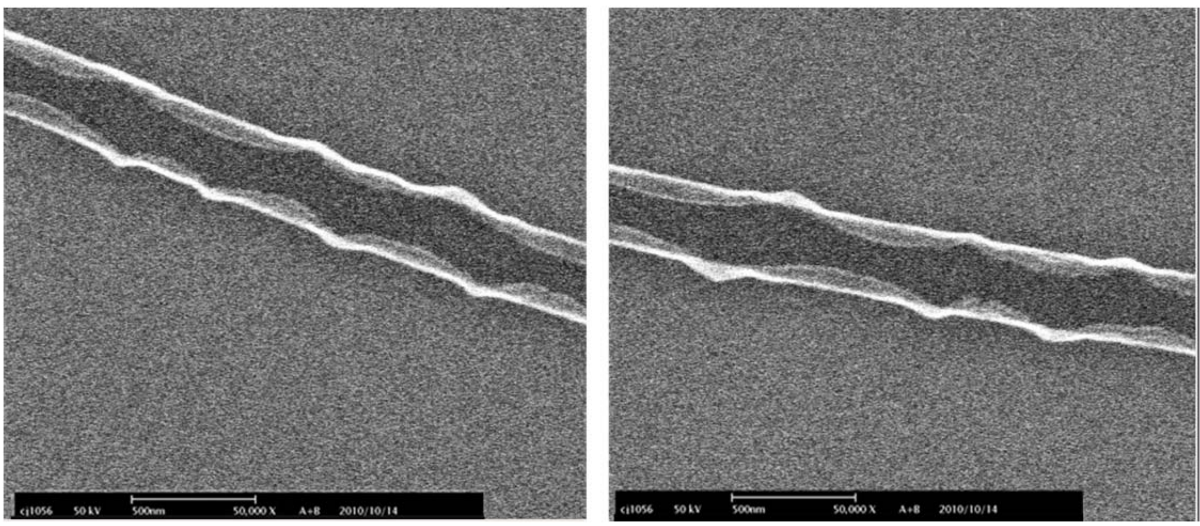

Figure 3.9: Structures with longer exposure and development times do not show significant improvement in resist profiles and resulting edge defects.

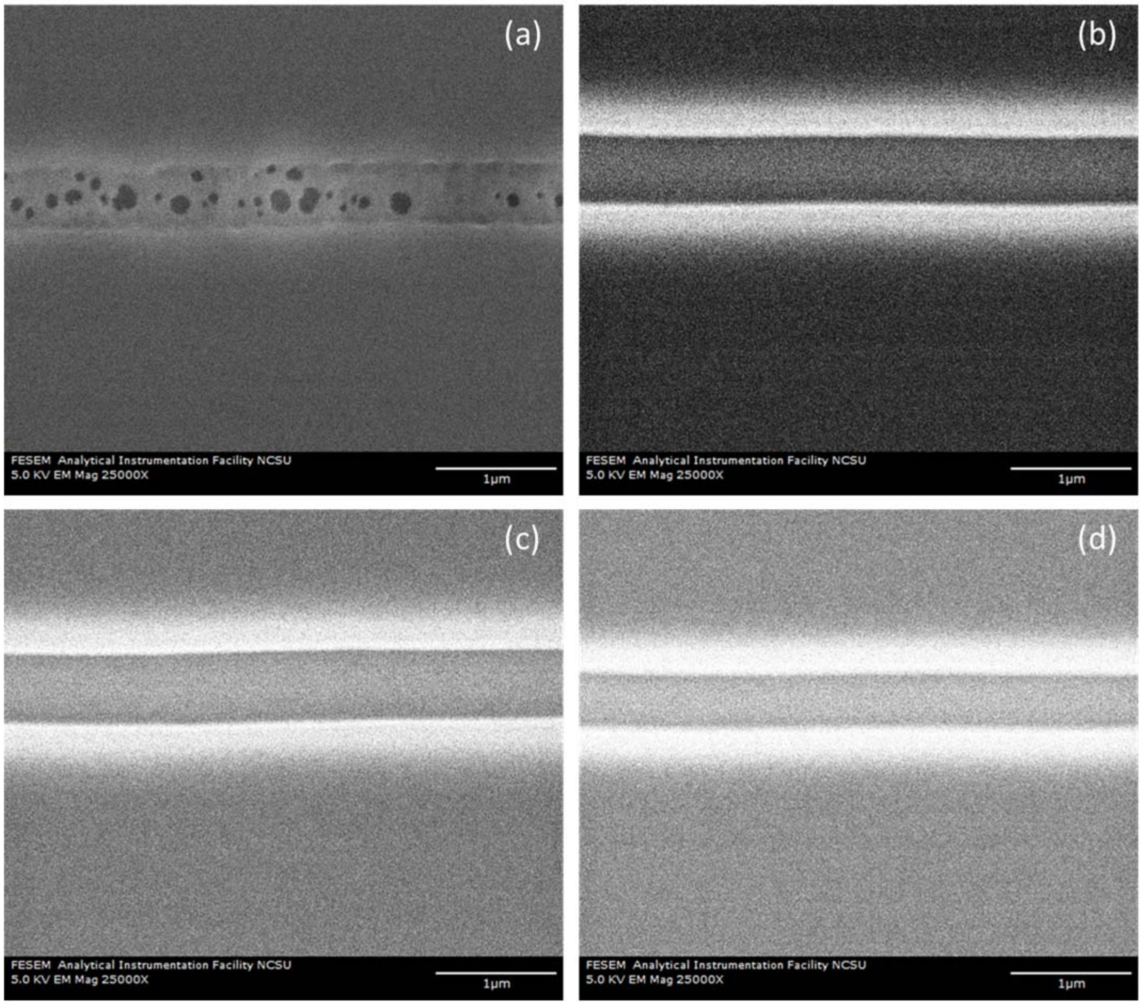

Figure 3.10: Exposure dose test for LOR/PMMA bilayer. Resist pattern for a 500 nm wide line after 50pA beam current exposed each 5 nm dot for (a) 1.5 µs, (b) 2.0 µs, (c) 2.5 µs and (d) 3.0 µs.

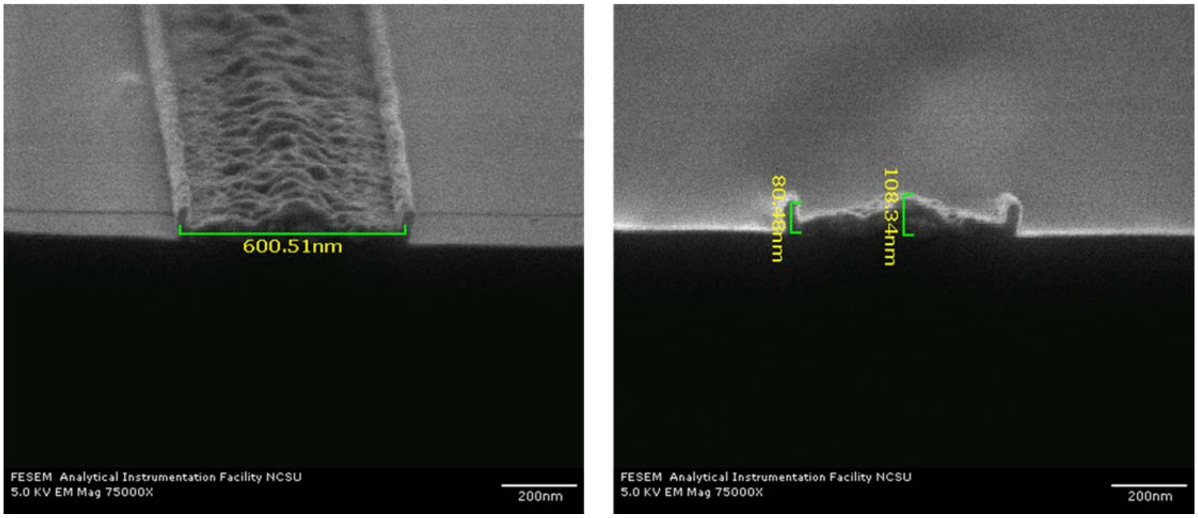

Figure 3.11: Variation in wire thickness across wire width in nanowires created using LOR/PMMA bilayer resist developed for 60 seconds in MF-319 with metal deposited via sputtering as observed in cross-sectional SEM images.

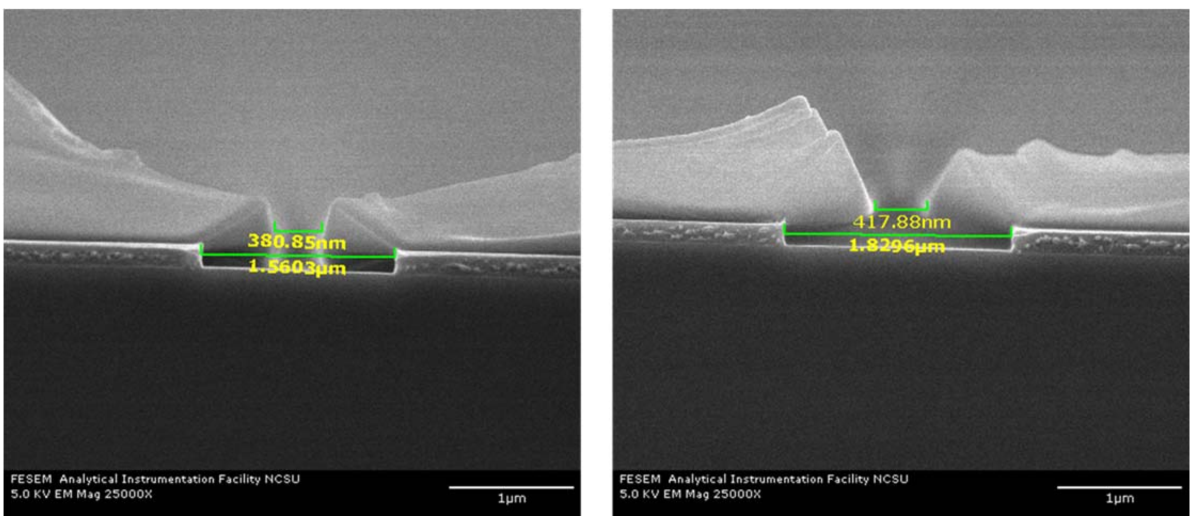

Figure 3.12: Cross-sectional resist profile of undercut occurring when LOR is developed for 60 seconds in MF-319 resist developer.

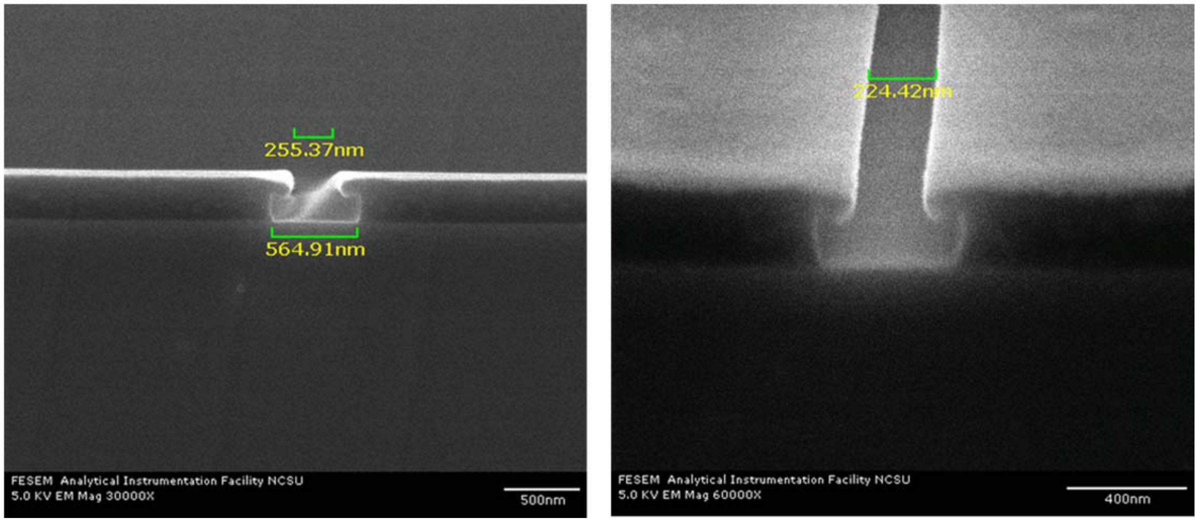

Figure 3.13: Resist profile of LOR/PMMA bilayer. The image on the right is taken with the sample tilted to show the undercut and the smooth edge of the resist pattern on along the PMMA top layer.

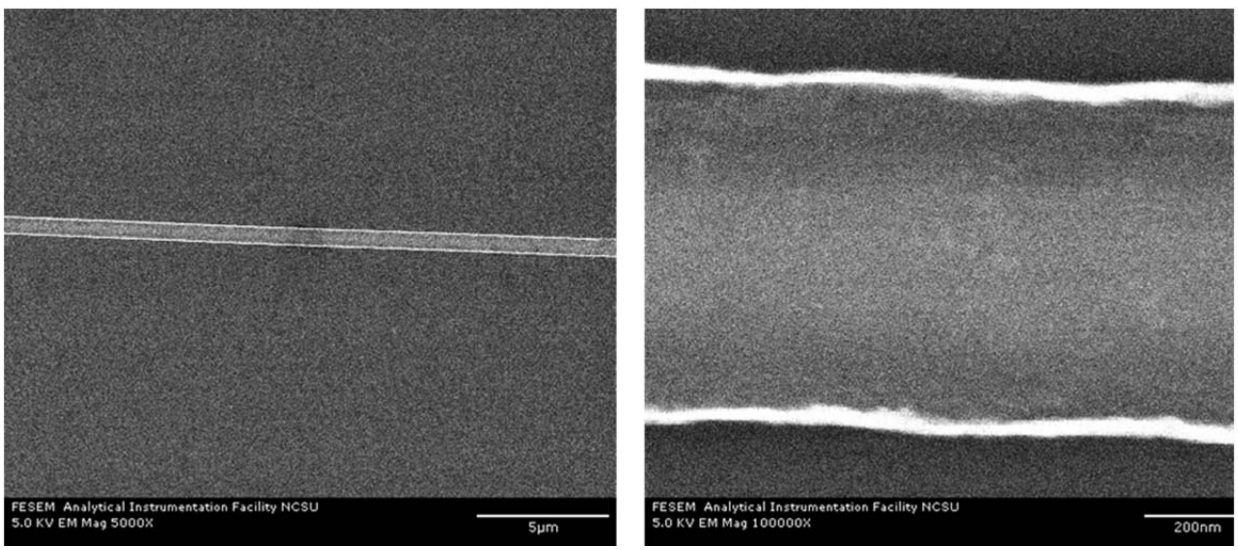

Figure 3.14: Smooth wires deposited by sputtering using LOR/PMMA resist structure to promote good liftoff.

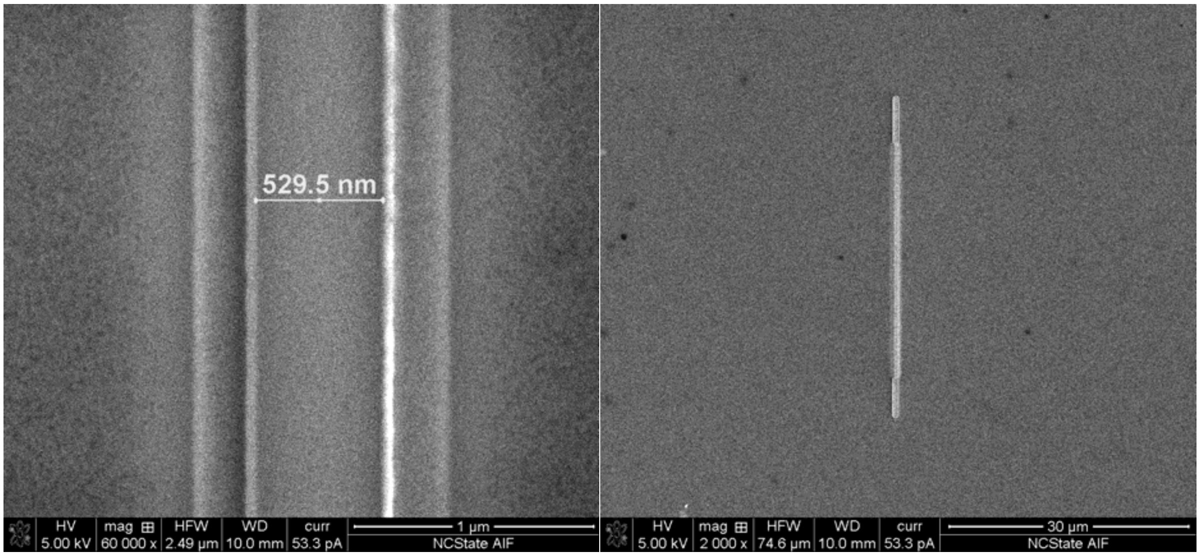

Figure 3.15: SEM image of ferromagnetic wires after FIB milling edges to reduce roughness. The high magnification image on the left shows the details of the resulting edge roughness and the milling regions on each edge of the nanowire. The image on the right has lower magnification so the milling regions can be seen with respect to the wire dimensions.

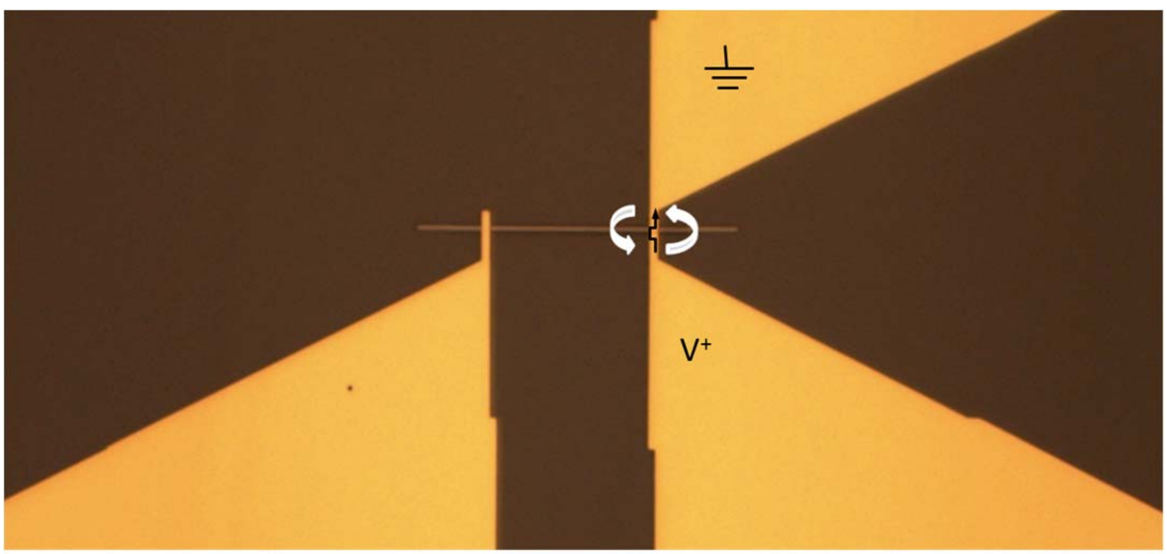

Figure 3.16: Applying a current pulse through a gold contact nucleates a domain wall in the ferromagnetic wire. The white arrows show the direction of the magnetic field rotation around the metal contact.

.

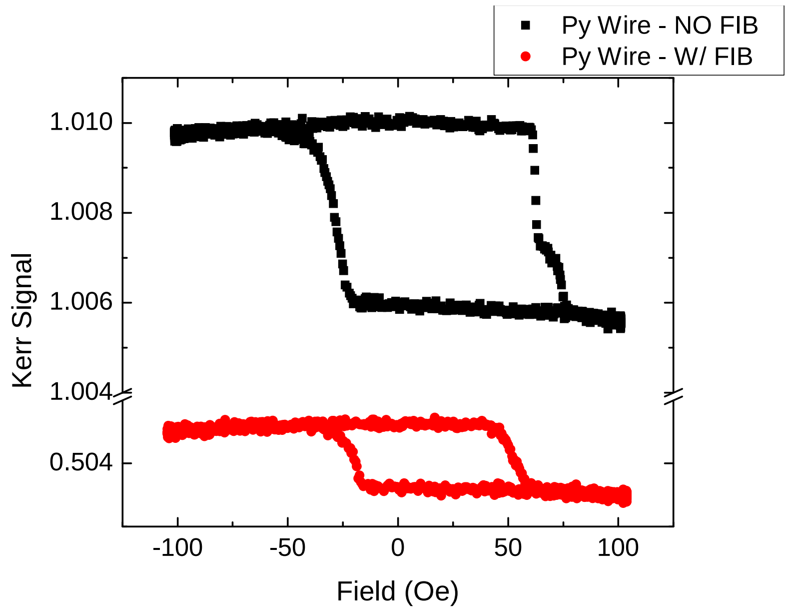

Figure 3.17: Magnetic hysteresis loops comparing two Py wires that have been prepared using the LOR/PMMA bilayer resist process with (red circles) and without (black squares) the wire edges milled by FIB. The wire that has received the milling process has a smaller depinning field but a significantly lower Kerr signal.

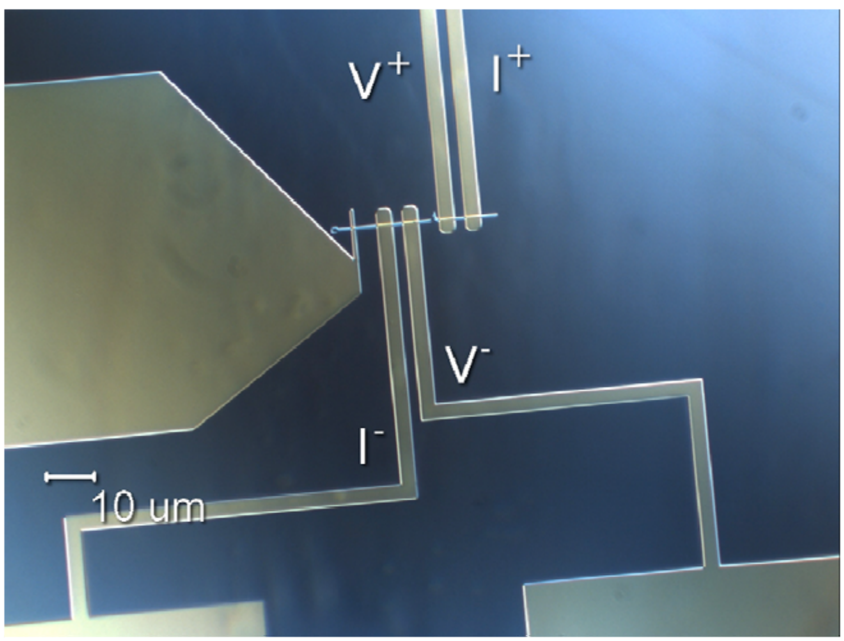

Figure 3.18: Optical microscope image of the 4-point GMR measurement technique. A current is applied through the outermost contacts while the voltage differential is measured across the adjacent contacts to determine the resistance of the multilayer wire.

Figure 3.19: SpinField 2D Magnetic Field platform used for GMR measurements that can generate magnetic fields along two axes and measure the strengths of the fields; available at http://www.directvacuum.com/.

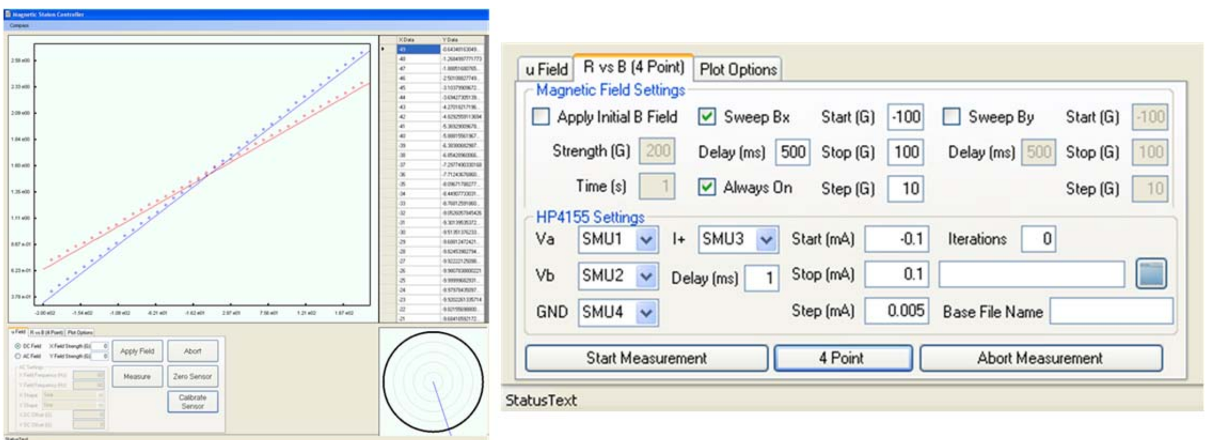

Figure 3.20: Software to automate measurements incorporating control of the HP4155 current meter, BOP power supplies and magnetic sensors in the 2D field platform. The magnetic field can be swept at intervals programmed by the user as shown on the right.

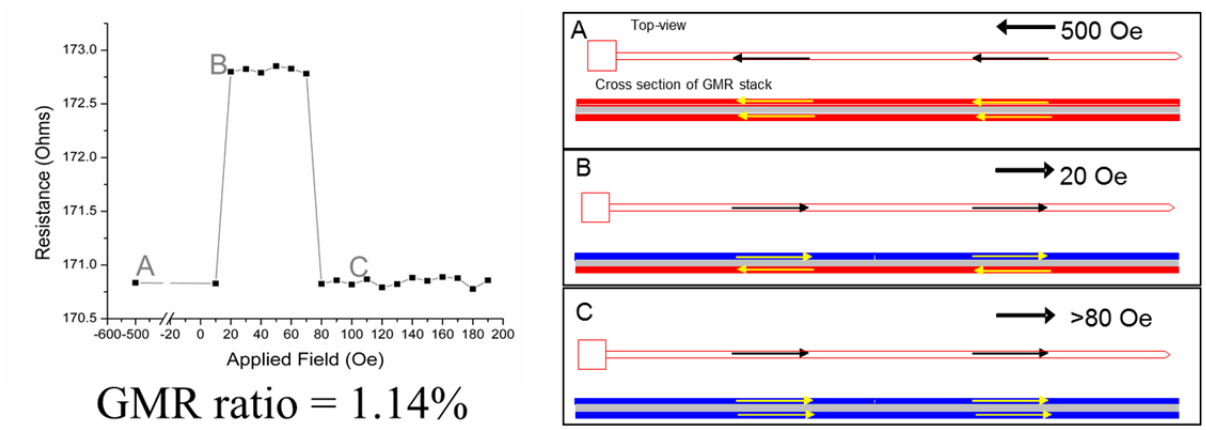

Figure 3.21: Measured resistance versus applied magnetic field demonstrating distinct parallel and antiparallel magnetic layer alignments in the straight wire on the right.

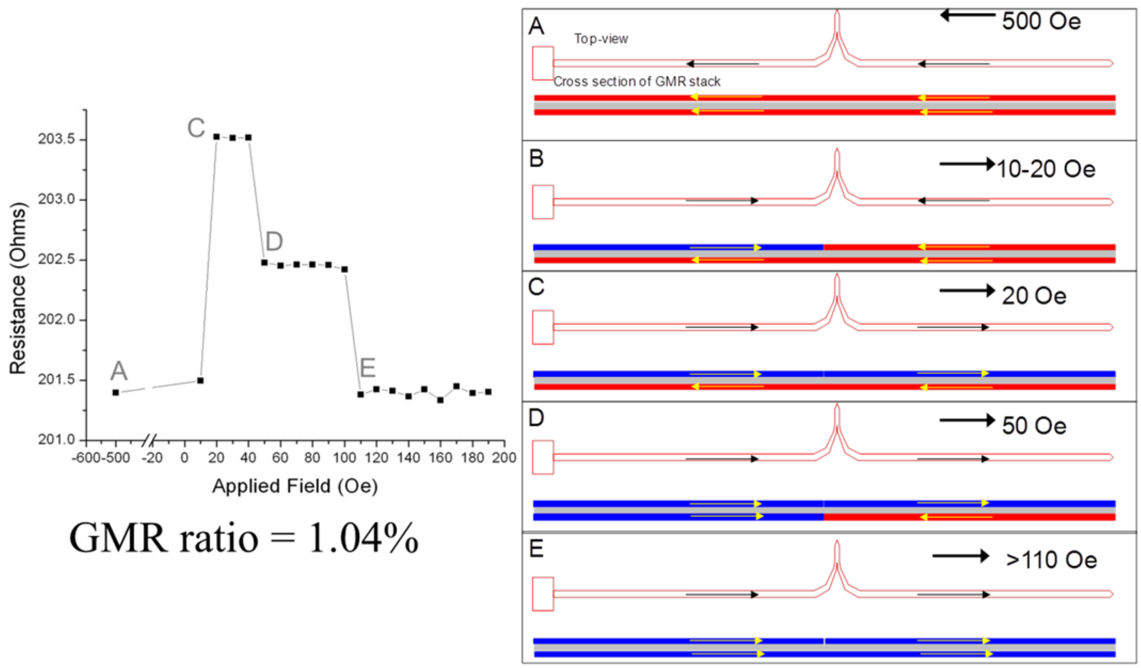

Figure 3.22: Resistance measurements of the GMR stack as a function of applied magnetic field. An intermediate resistance state occurs as the domain wall gets pinned at the cusp in the hard layer of the GMR stack. (The resistance corresponding to the alignment labeled in the cartoon on the left as B is not evident in the measurement because the field steps are too large to maintain pinning in the soft Permalloy layer.)

REFERENCES

[1] D. A. Allwood, G. Xiong, C. C. Faulkner, D. Atkinson, D. Petit, and R. P. Cowburn, "Magnetic domain-wall logic," *Science,* vol. 309, pp. 1688-1692, Sep 9 2005.

[2] R. C. Jaeger, *Introduction to Microelectronic Fabrication* vol. V. Upper Saddle River, New Jersey: Prentice Hill, 2002.

[3] Y. F. Chen, K. W. Peng, and Z. Cui, "A lift-off process for high resolution patterns using PMMA/LOR resist stack," *Microelectronic Engineering,* vol. 73-4, pp. 278-281, Jun 2004.

[4] G. Malinowski, A. Lorincz, S. Krzyk, P. Mohrke, D. Bedau, O. Boulle, J. Rhensius, L. J. Heyderman, Y. J. Cho, S. Seo, and M. Klaui, "Current-induced domain wall motion in Ni(80)Fe(20) nanowires with low depinning fields," *Journal of Physics D-Applied Physics,* vol. 43, 045003, Feb 2010.

[5] G. Xiong, D. A. Allwood, M. D. Cooke, and R. P. Cowburn, "Magnetic nanoelements for magnetoelectronics made by focused-ion-beam milling," *Applied Physics Letters,* vol. 79, pp. 3461-3463, Nov 2001.

[6] T. Ono, H. Miyajima, K. Shigeto, K. Mibu, N. Hosoito, and T. Shinjo, "Propagation of the magnetic domain wall in submicron magnetic wire investigated by using giant magnetoresistance effect," *Journal of Applied Physics,* vol. 85, pp. 6181-6183, Apr 1999.

[7] J. Grollier, P. Boulenc, V. Cros, A. Hamzic, A. Vaures, A. Fert, and G. Faini, "Switching a spin valve back and forth by current-induced domain wall motion," *Applied Physics Letters,* vol. 83, pp. 509-511, Jul 2003.

[8] C. Nam, Y. Jang, K. S. Lee, and B. K. Cho, "Current-driven output magnetization switching in a magnetic nanowire with a three-terminal Y junction," *Applied Physics Letters,* vol. 92, 202501, May 2008.

[9] D. Morecroft, I. A. Colin, F. J. Castano, J. A. C. Bland, and C. A. Ross, "Current-induced magnetization reversal in NiFe/Cu/Co/Au notched mesoscopic bars," *Physical Review B,* vol. 76,054449, Aug 2007.

CHAPTER 4

IMPACT OF RARE-EARTH DOPANTS ON MAGNETIC PROPERTIES

4.1 Motivation for Rare-Earth Doped Magnetic Alloys

Because materials engineering is key to understanding and optimizing domain wall dynamics, new materials must be explored for domain wall motion applications. Rare-earth dopants have been used to modify the magnetic properties of materials for over fifty years [1]. More recently, researchers have attempted to tailor the dynamical response of Permalloy (Py, $Ni_{0.80}Fe_{0.20}$) thin films by introducing rare-earth dopants to achieve higher data rates in MRAM devices [2-4]. These studies indicate that rare-earth doping may improve domain wall dynamics and have led us to focus on alloys doped with rare-earth elements.

In the aforementioned studies, various rare-earth dopants were analyzed for potential improvements in magnetic storage applications by measuring the effect on the Gilbert damping parameter, α, of Permalloy films. Different dopants provided much different impacts on α as shown in Fig. 4.1. Low concentrations of Tb and Dy increase α by an order of magnitude while Gd dopants have a negligible effect of the term [3]. The anisotropic *4f-5d* exchange interaction drives the slow relaxing impurity mechanism that causes the impact on α. The dopants effect on the Gilbert damping parameter is correlated to the strength of the exchange contribution to the anisotropy. Gd cannot contribute to further relaxation due to its isotropic exchange interaction between the *4f* and *5d* states [3]. While achieving a large damping parameter is desirable for magnetic storage devices, maintaining a low α value is important for domain wall dynamics. Energy is dissipated through damping which applies a retarding pressure on a propagating domain wall. As a result, Gd dopants that have a small impact on the α value demonstrate the most potential for domain wall dynamics.

Antiferromagnetic coupling occurs between the ferromagnetic transition metals (Ni, Fe, Co) and rare-earth elements meaning that the spins of these materials align antiparallel. Consequently, a decrease in magnetization occurs as a function of rare-earth doping in Permalloy as confirmed by Bailey *et al.*[2]. The composition of these alloys can even be adjusted to accomplish a compensated composition where the rare-earth element and the ferromagnetic transition metal have equal but opposite magnetizations resulting in no external magnetization. Adjusting the compositions of the alloys to minimize external magnetization is desirable in order to increase the domain wall velocity caused by the spin transfer torque according to Equation 2.4.

Rare-earth dopants produce a crystalline to amorphous transformation in Permalloy as rare-earth dopant atoms occupy sites of the host lattice introducing lattice defects and disorder [2]. Amorphous magnets are novel materials with attractive properties that make them very interesting for magnetic applications. Because there are no grain boundaries, the amount of pinning centers is reduced. The amorphous structure leads to small-scale film roughness and smooth interfaces in magnetic multilayer structures. Additionally, amorphous magnets are magnetically very soft because of the lack of magnetocrystalline anisotropy due to their non-crystalline state. Domain walls with larger widths should be formed due to the low crystalline anisotropy since the exchange energy is large compared to the anisotropic energy. As a result, domain walls in amorphous magnetic alloys propagated by a magnetic field potentially have a higher mobility since domain wall mobility is proportional to the domain wall width.

While the impact on magnetization is relatively clear, the effect of doping on current induced domain wall dynamics is more difficult to predict. While potential benefits to the adiabatic spin transfer velocity are achieved by the decrease in magnetization due to antiferromagnetic coupling, the overall benefit is dependent on the effect doping has on other material parameters such as the current polarization. Additionally, the domain wall velocity below Walker breakdown is dependent on the non-adiabatic factor. Dopant atoms act as scattering centers to reduce the spin-flip length [5] which would increase the non-adiabatic factor according to Equation 2.5. On the contrary, an increase in the domain wall width due to reduced crystalline energy of the amorphous compositions is predicted to reduce the non-adiabatic effects [6].

4.2 Alloy Compositions

In this work, we create novel magnetic alloys by doping ferromagnetic transition metals and their alloys with rare-earth elements and explore the effect of these dopants on material properties. Gd dopants are explored because they couple antiferromagnetically with the transition metals while only slightly increasing the damping parameter of Permalloy [2]. The doped are materials Co, Ni and Permalloy. We chose CoGd and NiGd alloys based on the abundance of compounds that can be formed by varying the material compositions as evident in the phase diagrams shown in Fig. 4.2. The PyGd alloy compositions are analyzed because Permalloy is already widely used in domain wall devices and our work is based on initial results from studies using Permalloy. The ternary phase diagram representing the PyGd composition is also included in Fig. 4.2.

Three series of compositions of CoGd, NiGd and PyGd were prepared by the co-sputtering technique briefly described in Chapter 3. Co-sputtering was accomplished onto Si substrates using an RF supply to deliver power to each magnetron sputter gun. Because the sputter rates of these magnetron guns have been shown to be linear with applied power, different alloy compositions are achieved by simply adjusting the relative power applied to each target. The deposition rates were then converted to atomic percentages for each composition. The product of the deposition rate and the elemental density was divided by the standard atomic weight for Gd and the doped material. The ratio of the two materials was analyzed to yield a compositions based on atomic percentages. The Gd concentrations for each of the various alloys created are shown in Table 4.1 along with the corresponding power applied to the Gd target. The power applied to the target for the doped material was held constant at 100 Watts. The NiGd and CoGd series consist of six different compositions with Gd concentration ranging from 0-25%. There are also six different compositions of PyGd alloys with the Gd concentration ranging from 0-12.5%.

4.3 Alloy Characterization

The effect of dopants on the magnetic properties and microstructure of each composition are measured. The crystallinity of the samples was analyzed using the X-ray diffraction (XRD) technique. During XRD measurements, the films are rotated while being bombarded with X-rays and the diffraction pattern is recorded. Crystalline samples produce peaks because constructive interference occurs when electrons are scattered by parallel crystal planes.

A Bruker D-5000 diffractometer with a Highstar detector was used to determine film crystallinity. A Cu Kα radiation source generated X-rays at 40 kV and 30 mA. The data shown in Fig. 4.3 confirm that a crystalline to amorphous transition takes place in all three alloy series. The compositions are XRD amorphous for all compositions with at least 10% Gd concentration.

4.3.1 Superconducting Quantum Interference Device (SQUID) Magnetometry

To understand the impact of doping on magnetic properties of the above alloys, superconducting quantum interference device (SQUID) magnetometry was performed at 4 K. SQUIDs are very sensitive magnetometers that consist of a ring of superconducting material with two Josephson junctions. A Josephson junction is a tunnel junction of two superconductors separated by an insulator. Electrons tunneling through these junctions demonstrate quantum interference dependent on the magnetic flux that occurs in the loop. Therefore the resistance is a function of magnetic field and is sensitive to even small fluctuations.

Our measurements were obtained with a Quantum Design MPMS XL-7 SQUID magnetometer. This tool can apply from 0-7 Tesla and can operate within a temperature range of 1.9 to 400 K with a sensitivity of $1x10^{-7}$ emu. We obtained hysteresis loops of our rare-earth doped magnetic alloys by sweeping the applied magnetic field from -1 to 1 Tesla and back. From these hysteresis loops values for the external magnetization and coercive field are extracted for each composition.

The hysteresis curves for the CoGd alloys are shown in Fig. 4.4. The magnetic moments of the Gd atoms oppose the moments of the Co atoms and reduce the amount of magnetization. Before the transition to an amorphous metal, introducing Gd atoms increases the coercivity of Co and results in hard magnetic films. However when films become amorphous, the alloys are magnetically soft as predicted.

Some compositions of amorphous CoGd films are known to exhibit perpendicular magnetic anisotropy (PMA) [7]. Materials with PMA are of interest for magnetic memory because they offer low switching currents with large thermal stability. Domain wall devices composed of materials exhibiting PMA are predicted to be more efficient than devices utilizing materials with in-plane anisotropy because the spin transfer torque must overcome a larger energy in the latter case [8].

SQUID measurements of the CoGd alloys with the magnetization direction perpendicular to the film plane were also analyzed to determine the anisotropy of the film compositions. The perpendicular measurements are shown in Fig. 4.5. To saturate the films' magnetization in the perpendicular direction fields that are 20 times larger than were applied for magnetization parallel to the film plane are required due to the shape anisotropy of the thin films. Like the parallel magnetization of the films, the perpendicular magnetization decreases monotonically with increasing Gd concentration. Therefore, we conclude the CoGd films measured do not exhibit PMA because the film thickness is 100 nm which is too small to create PMA [9].

The SQUID measurements of the NiGd alloys are shown in Fig. 4.6 and are similar to the CoGd series when small percentages of Gd dopants are introduced. The films become less magnetic and have higher coercivity when lightly doped with Gd. However, the magnetization of the NiGd films is more strongly affected by the Gd dopants. At higher percentages of Gd, the net magnetization due to the Gd atoms is larger than that of the Ni. The Gd dopant atoms dominate the overall magnetization of the alloy resulting in increasing magnetization with increasing Gd content. When the Gd content is at least 12.6%, the coercive field is drastically reduced implying that these alloys are very soft magnetically.

The coercivity of the CoGd and NiGd alloys as a function of Gd concentration is shown in Fig. 4.7. The coercive field is comprised of the domain nucleation field and pinning fields. It is beneficial to minimize both of these parameters to create an energy efficient device in which domains are written and propagated efficiently. An increase in coercivity occurs with doping before the amorphous transition is complete. After the films become amorphous, the coercivity reduces as the films become magnetically softer. The coercivity of the NiGd films reduces to approximately zero at $Ni_{0.923}Gd_{0.077}$ implying the magnetic state of these films could easily be altered by stray magnetic fields. However, forming nanowires with these compositions may induce enough shape anisotropy to increase the coercivity and ensure data retention.

The reduction in magnetization as a result of Gd dopants is demonstrated in Fig. 4.8. The reduction in magnetization of the CoGd and NiGd alloys are compared here with the impact of Gd dopants in Permalloy which was also obtained through SQUID measurements. A slight increase from the initial magnetization occurs in the PyGd film series. The CoGd and PyGd film compositions both exhibit a linear decrease above 7.5% Gd concentration. The magnetization of the CoGd films decreases by 4.3% for each percentage of Gd dopants introduced, whereas Gd dopants have a greater effect in the PyGd films resulting in a 7.8% decrease per atomic percentage of Gd.

The effect of the Gd dopants is proportional to the number of Bohr magnetons per atom for each of the doped materials. Gd atoms have the strongest magnetization out of the materials studied with -7.5 Bohr magnetons per atom at 0K. Gd dopants have the weakest effect on Co which has 1.7 Bohr magnetons per atom. The number of Bohr magnetons per atom for Permalloy is 1.2 which is comparable to the value for Co. Ni has only 0.6 Bohr magnetons per atom which explains the large slope of magnetization versus Gd concentration in the plot on the right of Fig. 4.8. Each percentage of Gd dopants added to the Ni film reduces the film's magnetization by ~11.3%. The measured magnetization value for the $Ni_{.965}Gd_{.035}$ composition is not accurate because the film was not fully saturated at 1,000 Oe which was the largest field applied for these measurements. The NiGd alloy with 7.7% Gd concentration is very close to the compensation point. The highly doped samples show an increase in magnetization when compared to pure Ni because Gd atoms have larger magnetic moments than Ni atoms and the Gd atoms are dominating the film's external magnetization.

It is important to note that promising materials for domain wall motion devices will have low coercive fields and low magnetization. To this end, we have identified several doped material compositions that exhibit these two parameters. Both NiGd and CoGd require low coercive fields when doped with ~12-18% Gd concentration. CoGd exhibits a very low magnetization at 25% Gd doping while the magnetization of NiGd is nearly eliminated when the composition is composed of 7.7% Gd. If no other parameters were affected by doping, the enhancement in current induced domain wall velocity would be inversely proportional to the reduction in magnetization that occurs.

However, many factors besides magnetization are crucial to a material's magnetization dynamics and will likely be impacted through doping. For example, the Gilbert damping factor is crucial in both magnetic and current driven domain wall velocities. Permalloy has a very low Gilbert damping factor that is 2-3 times lower than that of Co and Ni making Permalloy excellent candidate for domain wall dynamic studies. Consequently, the dynamical properties of Permalloy have been extensively studied. Therefore, the subsequent measurements of dynamic magnetic properties included in this dissertation are limited to doped Permalloy compositions because of Permalloy's low Gilbert damping factor and due to the extent of knowledge about the magnetization dynamics of this material.

4.3.1 Ferromagnetic Resonance (FMR) Measurements

Ferromagnetic resonance (FMR) originates from the precession of magnetic atoms under a magnetic field. The FMR technique is useful in determining dynamical properties of magnetic materials. During FMR measurements, a large DC field is applied perpendicular to the sample causing the magnetic atoms to precess with the same frequency. Power is absorbed by the sample when the frequency of the applied alternating magnetic field resonates with the sample's precessional frequency. To perform an FMR experiment, spectra can be taken at several points while sweeping the frequency or with a fixed frequency and a variable DC field. FMR spectra for our measurements were taken using a coplanar waveguide with fixed frequencies from 2 GHz to 40 GHz and swept applied fields up to 1.2 T. Both the resonance field at which the power from the alternating field is absorbed and the half power linewidth are obtained from the measured spectra. The main contributions to linewidth broadening are the intrinsic broadening which is proportional to the Gilbert damping factor and the inhomogeneous broadening term.

The FMR results are summarized in Fig. 4.9. Values for effective magnetization M_{eff} and gyromagnetic ratio γ were determined by fitting the resonance field and frequency data to

$$f = \frac{\gamma\mu_0}{2\pi}\left[H_{\mathrm{res}}(H_{\mathrm{res}} + M_{\mathrm{eff}})\right]^{1/2}. \tag{4.1}$$

The effective magnetization values for both SQUID magnetometry and FMR mearsurements showing the expected decrease in magnetization due to antiferromagnetic coupling between Permalloy and Gd atoms are presented in Fig. 4.10(a). SQUID magnetometry measures the magnetic moment of the film while FMR determines the effective magnetization characterizing the shape anisotropy of the film; differences can be attributed to perpendicular anisotropy. The measurements of film resistivity shown in Fig. 4.10(b) were measured on Hall bar structures. Resistance measurements of samples with different PyGd thicknesses but with the same 4 nm Ta capping layers verify that the resistivity of the capping layer is much greater than the PyGd layer. Therefore, the amount of shunt current carried by the capping layer is negligible.

The damping parameters were determined by fitting line width measurements to

$$\Delta H = \Delta H_0 + \alpha\frac{4\pi f}{\sqrt{3}\gamma}. \tag{4.2}$$

Plots showing trends of the gyromagnetic ratio and the damping parameter as a function of Gd concentration from fitting the FMR resonance spectra to Equation 4.1 and Equation 4.2

are shown in Fig. 4.11. Only a slight increase in the damping parameter is observed with 5.4% Gd concentration. With further increases in Gd content, a larger linear trend is observed. The damping value ranges from .0075 to .01221 for compositions ranging from 0-10.3% Gd concentration. The inhomogeneous broadening term ΔH_0 was less than 0.7 mT in each case, indicating high-quality, uniform films. Error bars in FMR data in Figs. 4.10(a), 4.11(a) and Fig. 4.11(b) are standard deviations of the least-squares fits.

4.4 Summary

Modifying magnetic materials by rare-earth doping creates novel magnetic alloys that should be explored for their potential to affect domain wall dynamics. Because the spins of the ferromagnetic transition metals and the heavy rare-earth metal Gd couple antiferromagnetically, alloy compositions can be adjusted to minimize the film's magnetization. Minimizing magnetization is desirable because magnetization is in inversely related to the spin transfer velocity. Doping ferromagnetic transition metals with Gd also produces an amorphous film as verified through XRD measurements. Amorphous magnets are very soft with reduced pinning due to grain boundaries.

Hysteresis loops of CoGd and NiGd alloys confirm the expected trends yielding a decrease in magnetization up to the compensation point and a decrease in coercivity beyond the amorphous transition. However, PyGd films are settled upon because Permalloy has a much lower initial Gilbert damping factor. PyGd films were evaluated using FMR to study the impact of Gd dopants on the damping parameter and gyromagnetic ratio. A slight increase occurred in the damping parameter while the magnetization decreased systematically with increasing Gd content. The large decrease observed in magnetization would provide a 50% improvement in the spin transfer velocity assuming the polarization value is unaffected by doping. The investigation of polarization of these doped films will be explored in Chapter 5. The PyGd film compositions will be further analyzed to evaluate their potential to enhance domain wall dynamics and to provide better understanding of current induced domain wall dynamics.

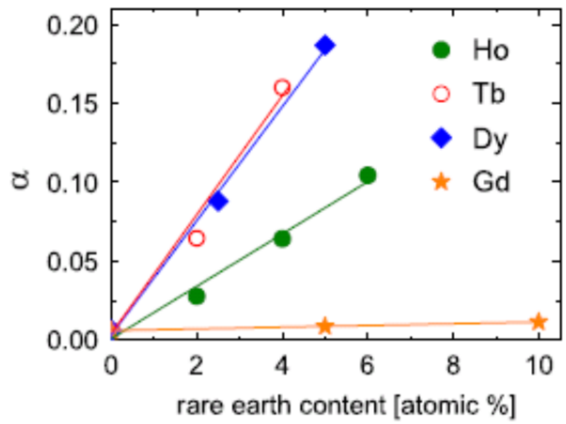

Figure 4.1: Doping Permalloy with various rare earth elements has demonstrated very different effects on the Gilbert damping parameter, α [3].

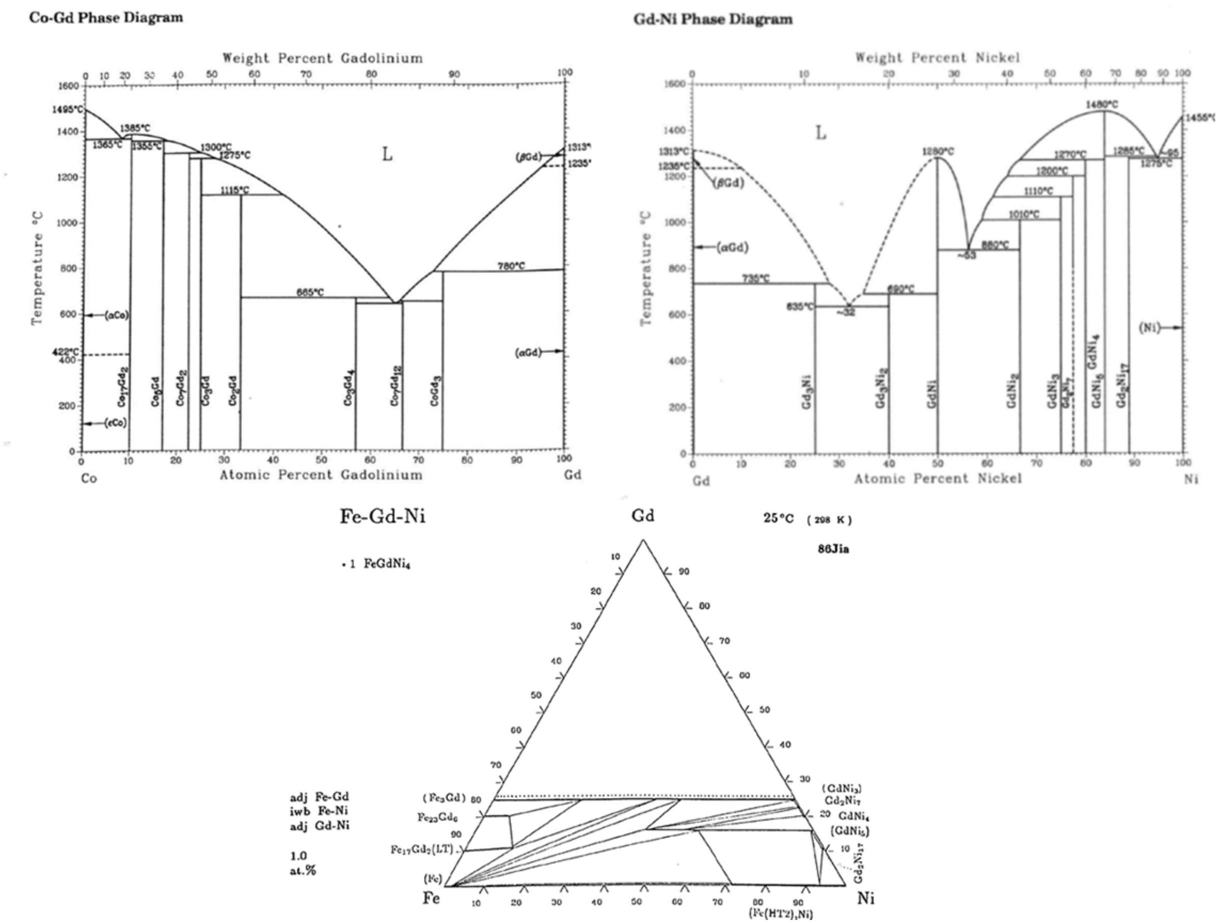

Figure 4.2: Phase diagrams of CoGd, NiGd and PyGd alloys showing various different compounds formed by varying the material compositions [10, 11].

Table 4.1: Alloy compositions for each material series. The first column represents the power applied to the sputter source with the Gd target. The second column conveys the atomic percentage of Gd in the resulting alloy.

NiGd		CoGd		PyGd	
Gd RF Power (Watts)	Gd Concentration	Gd RF Power (Watts)	Gd Concentration	Gd RF Power (Watts)	Gd Concentration
0	0.0%	0	0.0%	0	0.0%
6	3.5%	4	3.9%	4	3.7%
14	7.7%	8	7.5%	6	5.4%
24	12.6%	14	12.4%	9	7.9%
37	18.1%	22	18.2%	12	10.3%
55	24.8%	33	25.0%	15	12.5%

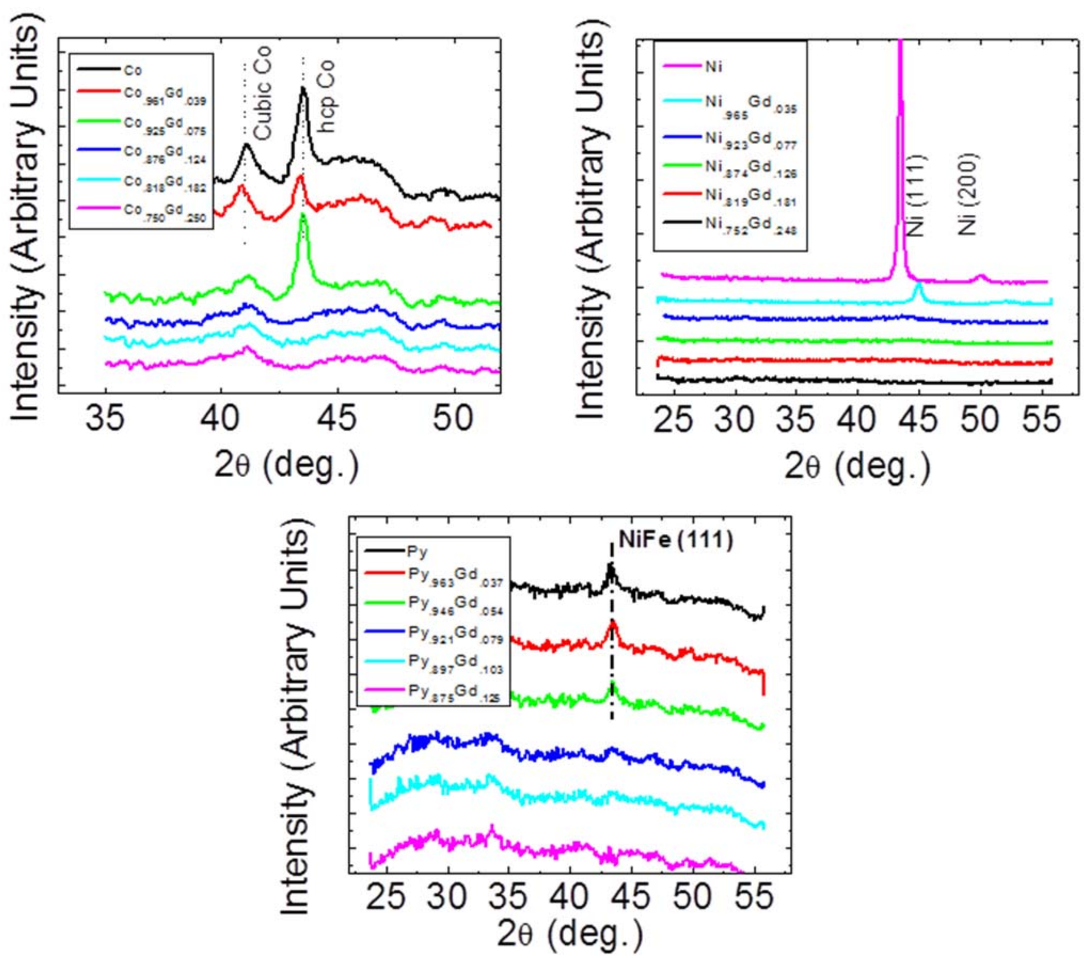

Figure 4.3: XRD measurements of each alloy series including varying composition formed by co-sputtering. Peaks are not observed for any compositions with at least 10% Gd concentration confirming amorphous alloys.

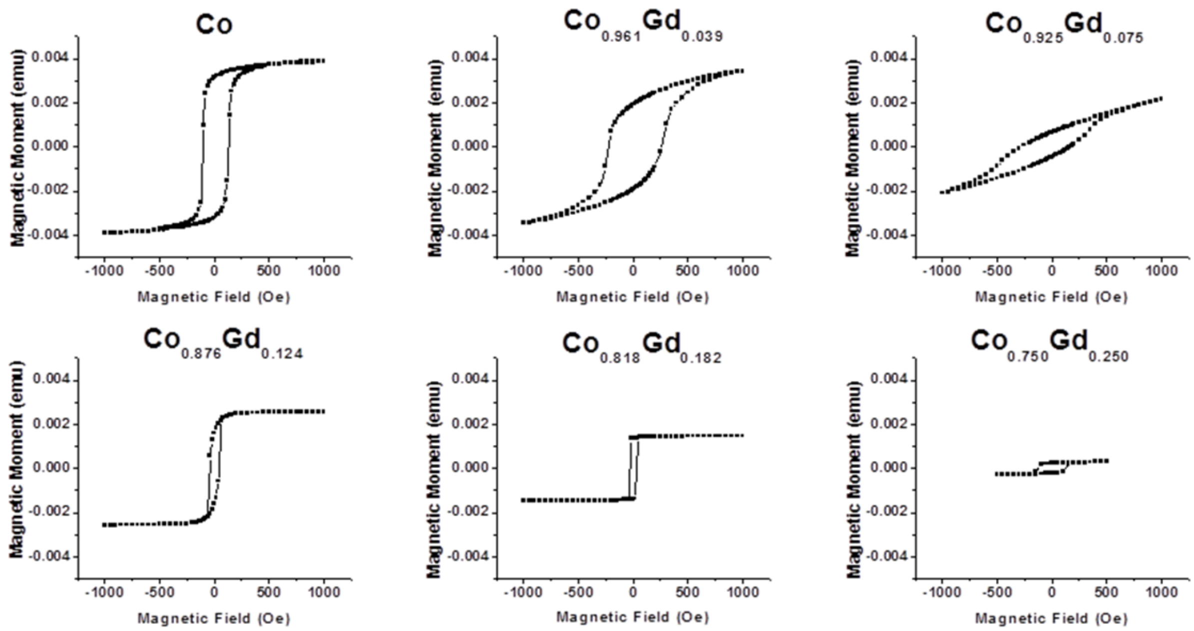

Figure 4.4: Magnetic hysteresis loops for CoGd alloys measured using SQUID magnetometry at 4 K.

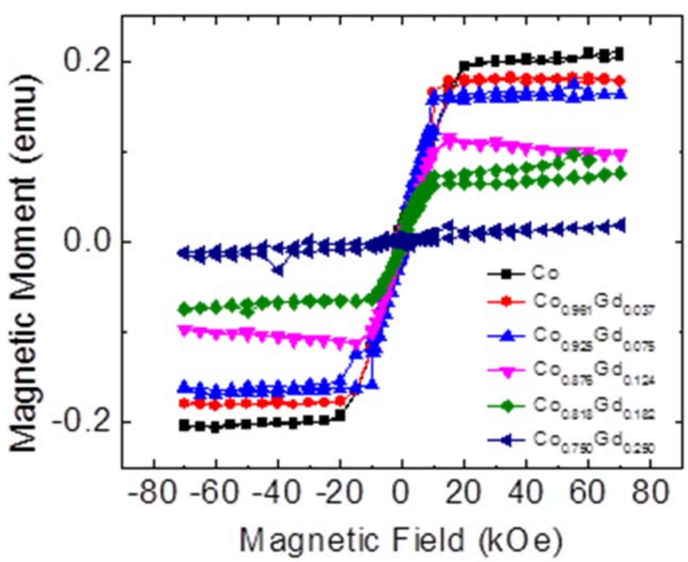

Figure 4.5: Perpendicular magnetization of the CoGd thin films obtained through SQUID measurements.

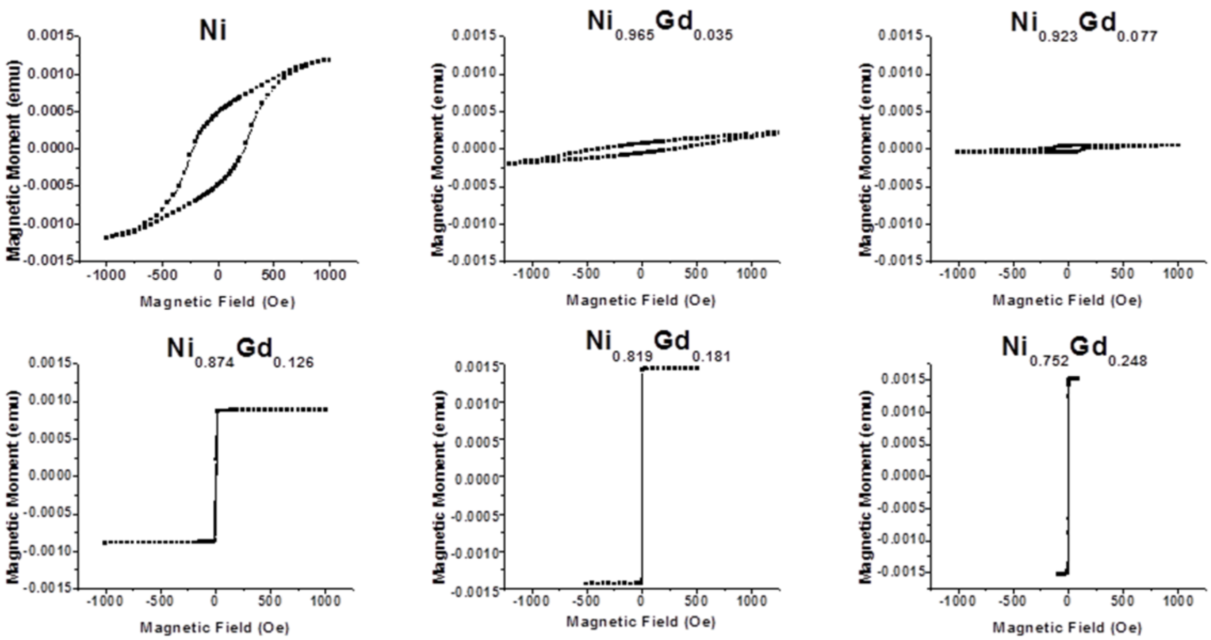

Figure 4.6: Experimental magnetic hysteresis loops for NiGd alloys obtained from SQUID measurements at 4 K.

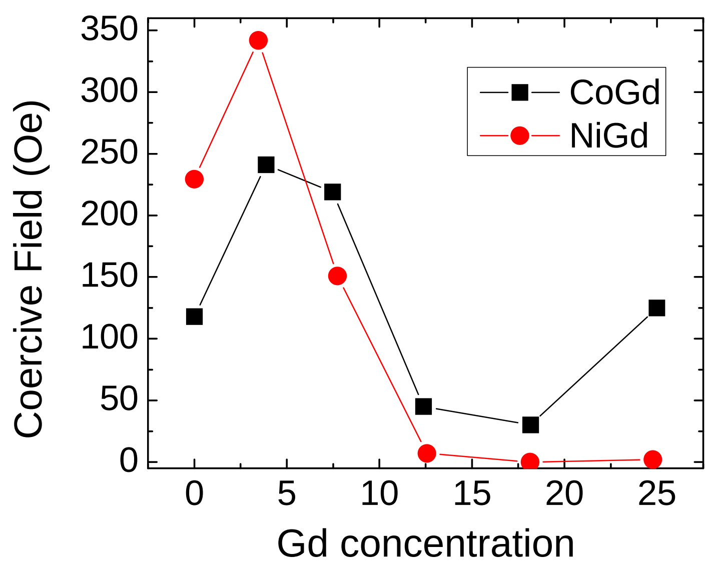

Figure 4.7: Coercive field as a function of Gd concentration for CoGd and NiGd alloys as determined from the SQUID measurements.

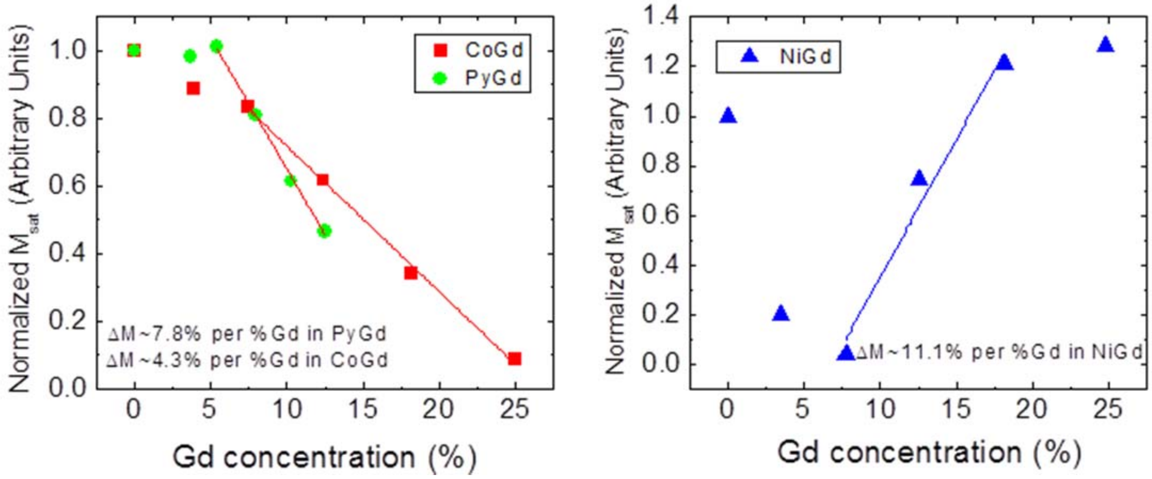

Figure 4.8: Change in magnetization as a function of Gd concentration for CoGd, PyGd and NiGd alloys as determined from the hysteresis loops obtained through SQUID magnetometry.

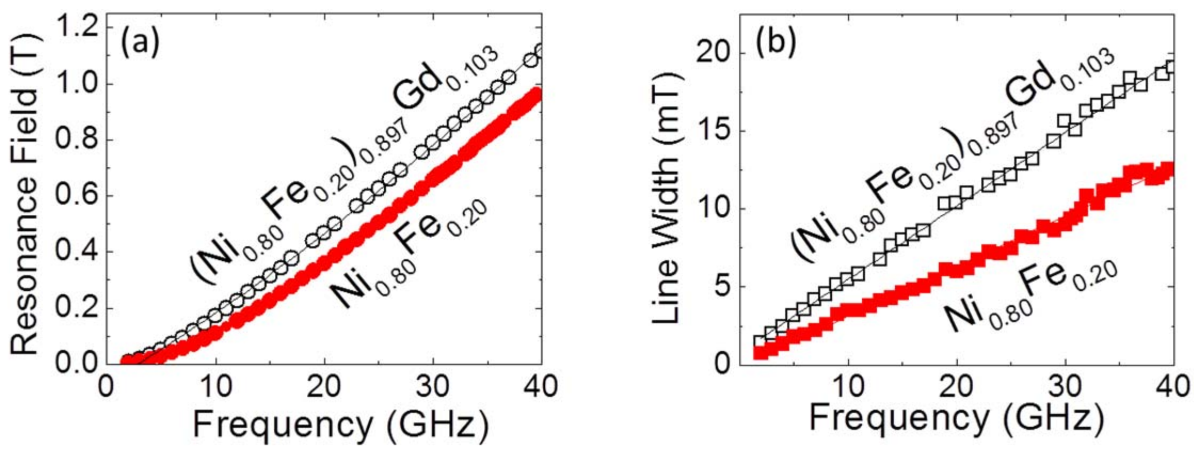

Figure 4.9: (a) Ferromagnetic resonance field and (b) line width as a function of excitation frequency for two representative samples. The small line width values obtained by extrapolation to zero frequency are indicative of high uniformity films.

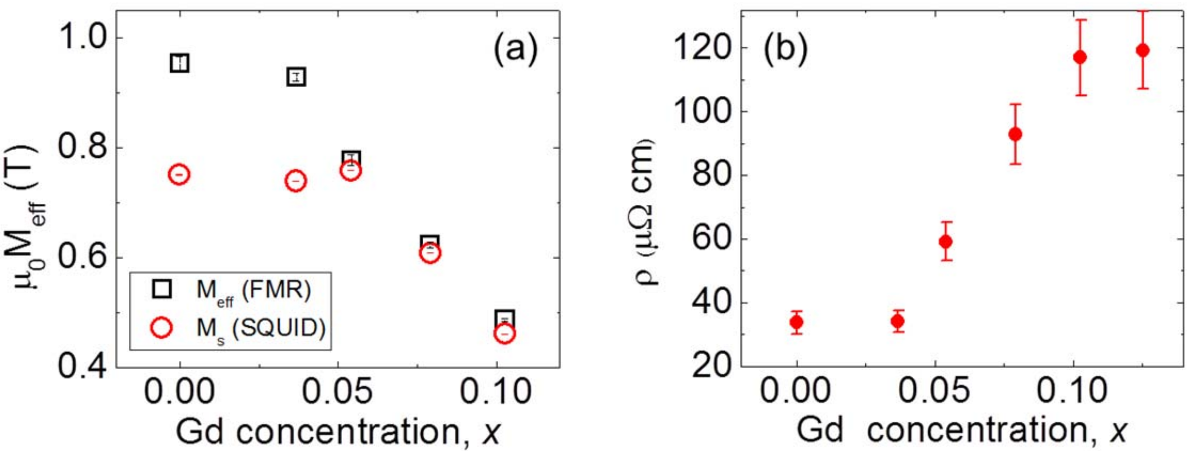

Figure 4.10: (a) Magnetization as a function of Gd concentration as measured by both SQUID and FMR techniques. (b) Resistivity as a function of Gd concentration measured across Hall bar patterns.

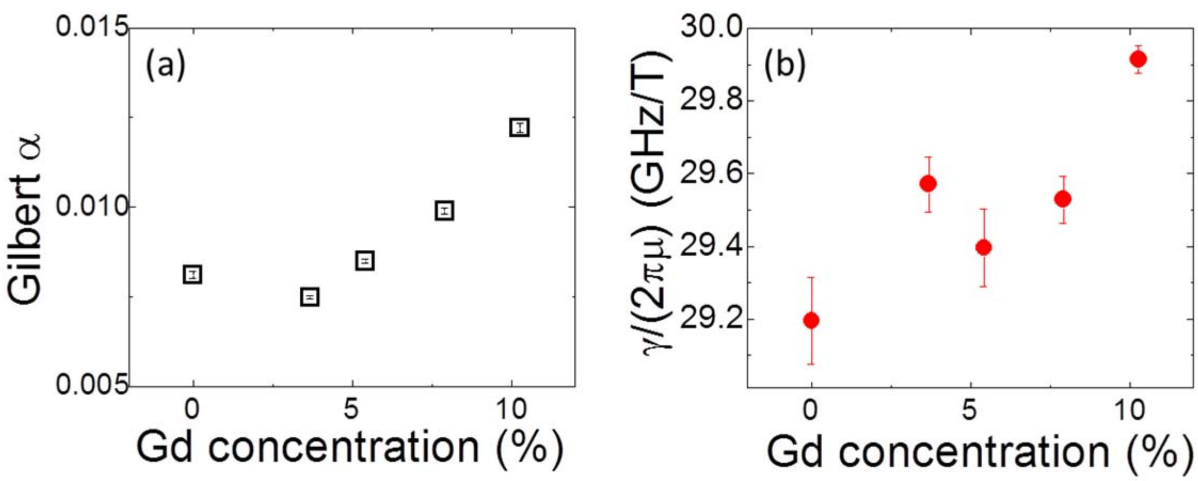

Figure 4.11: (a) Fitting of the resonance fields yields the gyromagnetic ratio and (b) fitting of the line width yields the damping parameter.

REFERENCES

[1] J. F. Dillon and J. W. Nielsen, "Ferrimagnetic resonance in rare-earth doped yttrium iron garnet. I. Field for resonance" *Physical Review,* vol. 120, pp. 105-113, May 1960.

[2] W. Bailey, P. Kabos, F. Mancoff, and S. Russek, "Control of magnetization dynamics in $Ni_{81}Fe_{19}$ thin films through the use of rare-earth dopants," *IEEE Transactions on Magnetics,* vol. 37, pp. 1749-1754, Jul 2001.

[3] G. Woltersdorf, M. Kiessling, G. Meyer, J. U. Thiele, and C. H. Back, "Damping by Slow Relaxing Rare Earth Impurities in $Ni_{80}Fe_{20}$," *Physical Review Letters,* vol. 102, 257602, Jun 2009.

[4] S. G. Reidy, L. Cheng, and W. E. Bailey, "Dopants for independent control of precessional frequency and damping in $Ni_{81}Fe_{19}$ (50 nm) thin films," *Applied Physics Letters,* vol. 82, pp. 1254-1256, Feb 2003.

[5] A. Thiaville, Y. Nakatani, J. Miltat, and Y. Suzuki, "Micromagnetic understanding of current-driven domain wall motion in patterned nanowires," *Europhysics Letters,* vol. 69, pp. 990-996, Mar 2005.

[6] J. A. Xiao, A. Zangwill, and M. D. Stiles, "Spin-transfer torque for continuously variable magnetization," *Physical Review B,* vol. 73, 054428, Feb 2006.

[7] R. C. Taylor and A. Gangulee, "Magnetization and magnetic-anisotropy in evaporated GdCo amorphous films," *Journal of Applied Physics,* vol. 47, pp. 4666-4668, May 1976.

[8] S. Mangin, D. Ravelosona, J. A. Katine, M. J. Carey, B. D. Terris, and E. E. Fullerton, "Current-induced magnetization reversal in nanopillars with perpendicular anisotropy," *Nature Materials,* vol. 5, pp. 210-215, Mar 2006.

[9] Chaudhar.P, J. J. Cuomo, and R. J. Gambino, "Amorphous metallic films for bubble domain applications," *IBM Journal of Research and Development,* vol. 17, pp. 66-68, Jan 1973.

[10] T. B. Massalski, H. Okamoto, P. R. Subramanian, and L. Kacprzak, *Binary Alloy Phase Diagrams*, 2 ed. Materials Park, OH: ASM International, 1990.

[11] P. Villars, *Handbook of ternary phase diagrams*. Materials Park, OH: ASM International, 1995.

CHAPTER 5

SPIN WAVE DOPPLER MEASUREMENTS

5.1 Spin Wave Doppler Technique

A spin wave Doppler technique is explained in this chapter and used to measure the spin transfer velocity and the current polarization in current-carrying $Py_{1-x}Gd_x$ alloy wires. Reduced magnetization values with Gd doping suggest possible increases in the spin transfer velocity of Permalloy. Contrary to these expectations, we measure a decrease in the spin transfer velocity upon introducing Gd dopants. For a current density of 10^{11} A/m^2, the measured velocities range from 6.0 m/s ± 0.6 m/s for pure Permalloy to 2.6 m/s ± 0.3 m/s for $Py_{0.946}Gd_{0.054}$. Interpretation of these values yields a current polarization ranging from 0.71 ± 0.02 to 0.30 ± 0.01 for the same compositions. These results reveal that Gd dopants in Permalloy have a more significant impact on the current polarization than on the material's magnetization for these alloy compositions.

Doppler shifts generally occur when there is relative motion between a source and the observer but can also occur with a stationary source and observer but motion within the medium. For example, systematic perturbations in water result in waves propagating away from the source with a frequency determined by the oscillation frequency of the perturbations and the properties of the water. However, if the water is flowing in relation to the source the waves propagating in the direction of the water flow will have a longer wavelength while the wavelengths of waves opposing the direction of current flow will be reduced as illustrated in Fig. 5.1.

In a ferromagnetic material, all atomic spins are aligned parallel. However, if the magnetic moment of one atom is deflected due to some external stimulation this deflection will effect neighboring moments and result in the propagation of the perturbation through the ferromagnetic material. These propagating perturbations are called spin waves and precess with the same frequency about an external magnetization with a direction and wavelength determined by the wave vector $\mathbf{k}$. Applying a current shifts the spin wave dispersion relation. The magnitude of this shift is equivalent to the dot product of the wave vector and the spin transfer velocity as shown:

$$\Delta w = \mathbf{k} \cdot \mathbf{u} \tag{5.1}$$

Recent experiments have demonstrated that magnetization spin transfer velocity and subsequently polarization can be obtained through a spin wave Doppler technique [1-3]. We use the spin wave Doppler technique to measure the effect Gd dopants in Permalloy have on the spin transfer velocity. Much of the device fabrication and the spin wave Doppler measurements were conducted at the Center for Nanoscale Science and Technology facilities at the National Institute of Standards and Technology. The reduced magnetization values achieved with Gd doping shown by the SQUID measurements in Chapter 4 suggest possible improvements in the spin transfer velocity according to Eq. 2.4. However, the effect that Gd dopants have on polarization and β will determine the effectiveness of Gd doping in increasing the current driven domain wall velocity. Lepadatu et al. conclude from measurements of domain wall depinning that doping Permalloy with Gd increases the non-adiabatic factor β while inducing only small changes in the adiabatic spin transfer velocity, $\mathbf{u}$ [4]. In this paper, we use the spin wave Doppler technique to provide a direct measurement of the spin transfer velocity and the effect of Gd doping on the current polarization of Permalloy. Contrary to Ref. [4], we find that Gd doping has a negative effect on both the current polarization and **u**.

5.2 Spin Wave Doppler Devices

For Doppler measurements, the PyGd films were patterned using photolithography and lift-off techniques to obtain 30 nm thick wires with varying widths on high-resistivity Si wafers coated with a 20 nm Al_2O_3 adhesion layer. Four DC contacts were patterned at the wire ends for current application and four-point resistance measurements. A 50 nm Al_2O_3 insulating layer was evaporated prior to patterning microwave antennas over the wires via electron beam lithography. Other details concerning device fabrication are given elsewhere [2]. An example device used to obtain spin wave Doppler measurements is shown in Fig. 5.2. The bulk magnetization of the wire is saturated by applying an in-plane static field perpendicular to the wire.

The microwave antennas, connected to the two ports of a vector network analyzer, emit and detect spin waves that propagate through the magnetic strip. The periodic structures of the antennas (inset of Fig. 5.2) couple primarily to the spin wave modes of two wave vectors: $k_0 = 8.38\ \mu m^{-1}$ and $k_1 = 2.79\ \mu m^{-1}$. The transmission peaks due to these two wave vectors are well separated in frequency [1, 2]. The transmission impedance values are extracted from the transmission coefficients measured from antenna to antenna and are averaged over 1,280 individual transmission spectra. The components due to spin waves are isolated by subtracting background spectra at a reference field sufficient to shift the resonance outside the measured frequency window. Applying current to the magnetic wire shifts the spin wave angular frequency relative to the zero-current value by an amount determined by Equation 5.1 [1].

The high current densities applied during these measurements result in temperature increases due to Joule heating within the wire. Previous room temperature measurements of 4 μm Permalloy wires indicated results from Doppler measurements were not compromised due to this heating because the spin transfer velocity in Permalloy is only weakly temperature dependent [2]. However, the effects of Joule heating become more pronounced in film compositions with higher Gd content due to increased resistivity.

The effect of heating in wires of various widths was analyzed by measuring resistance as a function of temperature on a heated chuck. The changes in resistance due to high current density were then measured. In 8 μm wires with 8% Gd content, the maximum current density of 1.3×10^{11} A/m^2 caused the resistance to increase by a fraction of 10% while in 2 μm wires the fractional increase in resistance was only 2.5%. The change is resistance due to the maximum applied current density as a function of Gd concentration is shown in Fig. 5.3 along with the resistance measurements as a function of temperature. By correlating the resulting current dependent resistance changes with the temperature dependent resistance measurements, we estimate temperature changes of 136 K and 34 K respectively as seen in Fig. 5.4. We conclude that wider wires exhibit a greater temperature increase than more narrow wires because they require larger currents to accomplish the same current density. To avoid issues with heating, the measurements are limited to 2 μm wires. In the measurements, we ensure that variations in Joule heating are kept to a minimum by holding the current constant while measuring the transmission of spin waves parallel and antiparallel to the current direction. Consequently, the frequency shifts measured are caused by the applied current rather than temperature variations and their magnitudes are twice as large (from –J to +J) as theoretical shifts occurring with and without current flowing through the device (from 0 to +/-J).

5.3 Spin Wave Doppler Measurements

An example of the frequency shifts that occur between transmission impedances, Z_{12} and Z_{21}, is shown in Fig. 5.5 for a $Py_{0.963}Gd_{0.037}$ wire. In the upper panel, a positive current density of 1.3×10^{11} A/m^2 is applied to the wire shifting Z_{12} and Z_{21} to higher and lower frequencies respectively. Reversing the current also reverses the sign of the frequency shift as shown in the lower panel. The frequency shift is estimated over the displayed range in Fig. 5.5 and found by fitting the autocorrelation function of the transmission spectra to locate the maximum. Standard errors in the frequency shift were less than 0.070 MHz for all such fits. However, the frequency shift is also slightly dependent on the range of values selected for each fit. As a result, we conservatively estimate our maximum uncertainty as the minimum frequency step size of the spectrum of 2.5 MHz.

The current-dependent frequency shift, Δf, for samples with different Gd content are shown in Fig. 5.6(a). The spin transfer velocity is obtained from the frequency shift where $u = \pi \Delta f / k$. Spin transfer velocities for a current density of 10^{11} A/m^2 were extracted from the slopes of the linear fits for varying Gd content and plotted in Fig. 5.6(b). Error bars are the combined uncertainties from uncertainty in width and thickness of the stripe, uncertainty in wavelength of spin waves and standard deviation of the linear fit.

The measurements were verified by comparing multiple devices for each concentration, and the spin transfer velocity measurements were within the error bars on all compositions except the $Py_{0.921}Gd_{0.079}$ samples. Four different $Py_{0.921}Gd_{0.079}$ device samples were measured yielding a range from (3.7 ± 0.4) m/s to (5.4 ± 0.6) m/s. We speculate that these highly doped amorphous films show greater variation because changes can occur in the microstructure of these films due to the heating at large current densities applied during measurements. An average velocity of (4.3 ± 0.5) m/s was obtained by applying a linear fit to all the acquired data points at the current density of 10^{11} A/m^2. The minimum value for the spin transfer velocity is (2.6 ± 0.3) m/s for 5.5% Gd content. This is a fractional reduction of 57 % from the value for Permalloy, (6.0 ± 0.6) m/s. Introducing Gd dopants results in a reduction of the spin transfer velocity, an effect that contradicts expectations based solely on the decrease in magnetization.

Using the spin transfer velocity equation (Equation 2.4), polarization values are extracted using the slope of **u** vs. **J** and the magnetization data obtained by SQUID measurements. As expected, the polarization values as a function of Gd dopant content follow the trend of the spin transfer velocity, also reaching a minimum at the $Py_{0.946}Gd_{0.054}$ composition as shown in Fig. 5.7(a).

The spin-up and spin-down conductivities of these alloys are obtained using: $\sigma_{\uparrow} = (1+P)/2\rho$ and $\sigma_{\downarrow} = (1-P)/2\rho$. These quantities are plotted in Fig. 5.7(b). In agreement with the previous results for Permalloy, we find the spin-up conductivity to be much larger than the spin-down conductivity [2]. The spin-up conductivity shows a monotonic decrease with the largest effect occurring between samples consisting of 3.7% and 5.4 % Gd content.

The spin down conductivity shows an initial increase but decreases for concentrations above 3.7% Gd content. The simultaneous increase in the minority conductivity and decrease in the majority conductivity is an effect expected for increased spin flip scattering [2, 5]. Spin flip scattering mixes the majority and minority conduction channels, reducing the polarization.

5.4 Conclusions

We finish with speculation on the prospects for increasing the current driven domain wall velocity via further Gd doping of Permalloy. The relative increase in both spin transfer velocity and polarization between the $Py_{0.945}Gd_{0.055}$ and the $Py_{0.921}Gd_{0.079}$ compositions (Fig. 5.6(b)) suggests that the spin transfer velocity may increase with further Gd doping. Unfortunately, due to its low magnetization and increased damping value, the alloy with $x = 0.103$ Gd content did not provide sufficient spin wave transmission signal to allow spin transfer velocity measurements.

In conclusion, we have measured the spin transfer velocity and polarization in PyGd wires using the spin wave Doppler technique. The current polarization of $(Ni_{0.80}Fe_{0.20})_{1-x}Gd_x$ decreases for compositions with up to $x = 0.054$ Gd content, corresponding to an overall decrease in spin transfer velocity. Compositions with higher Gd content demonstrate the potential to possess larger current polarizations and spin transfer velocities. We conclude that modulating the properties of Permalloy by introducing Gd dopants has a strong impact on the material's current polarization.

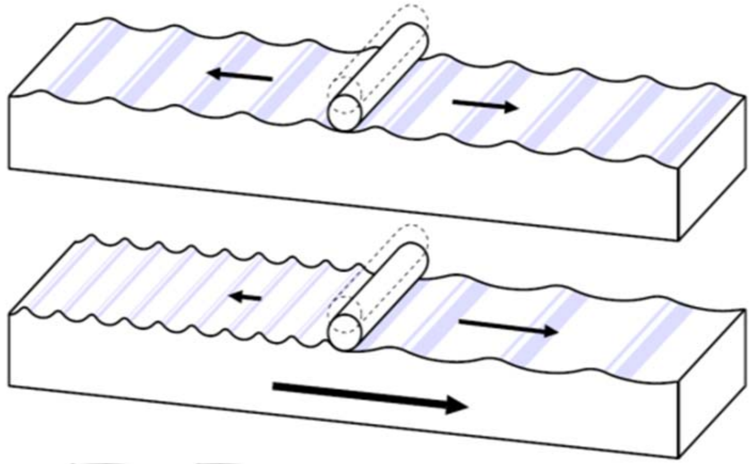

Figure 5.1: A Doppler shift occurs in water waves where there is flow in relation to a perturbation source [6].

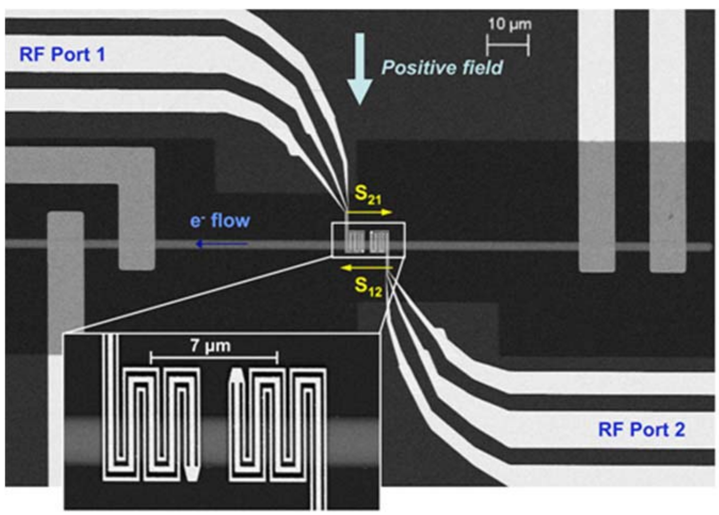

Figure 5.2: SEM image of the fabricated Doppler device with a 2 μm wide PyGd wire, seen here as a thin horizontal line. S_{12} (S_{21}) refers to the spin wave transmission from RF port 2(1) to port 1(2). The direction of electron flow for positive current is represented by the arrow in the image. The inset shows a magnified image of the microwave antennas with a center-to-center distance of 7 μm.

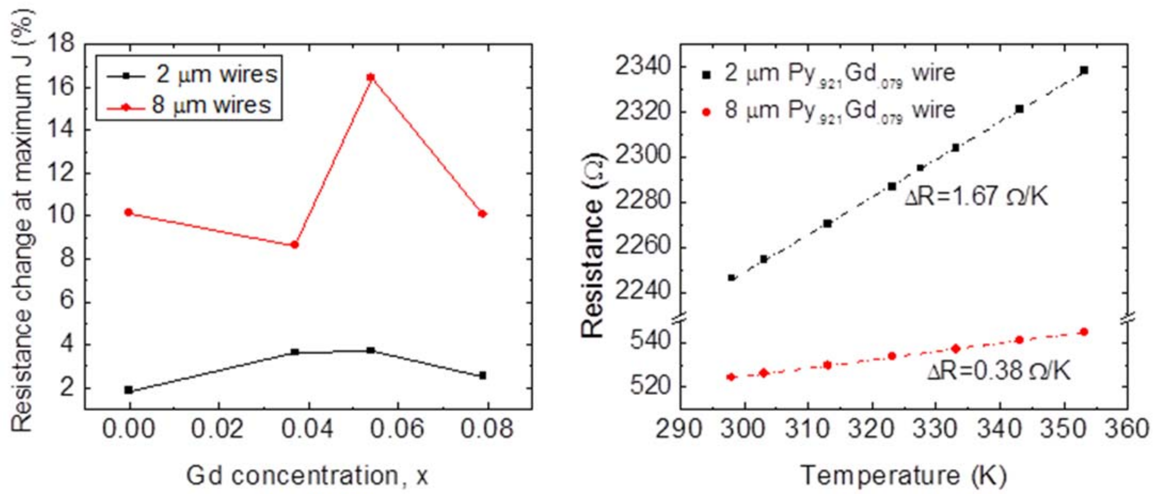

Figure 5.3: Changes in resistance due to high current density shown on left. The percent change is greater for the 8 μm wires because they have a lower resistance. The plot on the right shows the measured resistance as a function of temperature for $Py_{0.921}Gd_{0.079}$ wires with widths of 2 μm and 8 μm.

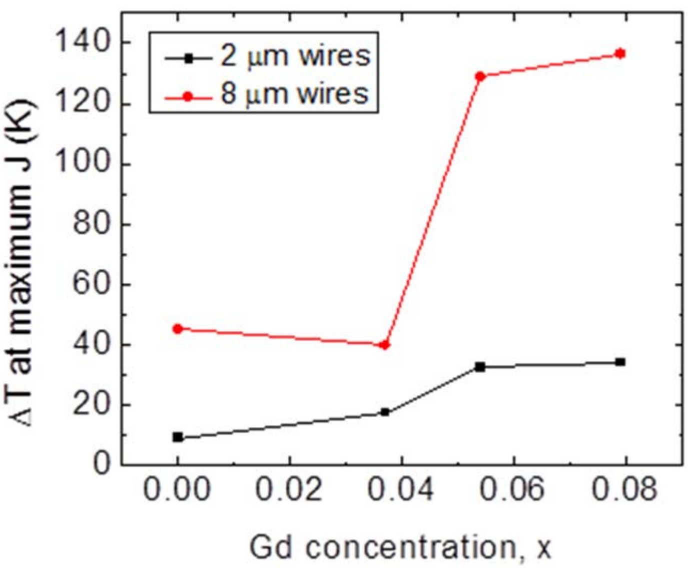

Figure 5.4: Amount of Joule heating occurring in the samples at the maximum current density of 1.3×10^{11} A/m^2. Temperature changes above 100 K will potentially alter our results although the spin transfer velocity is weakly temperature dependent.

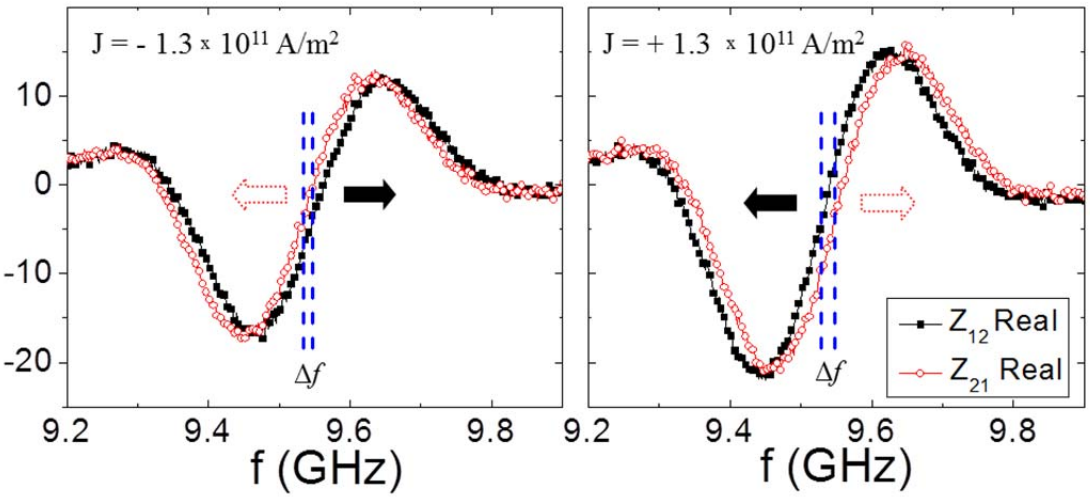

Figure 5.5: Real part of the transmission impedance Z_{12} and Z_{21} when a current density of $\pm 1.3 \times 10^{11}$ A/m^2 flows through the $Py_{0.963}Gd_{0.037}$ wire.

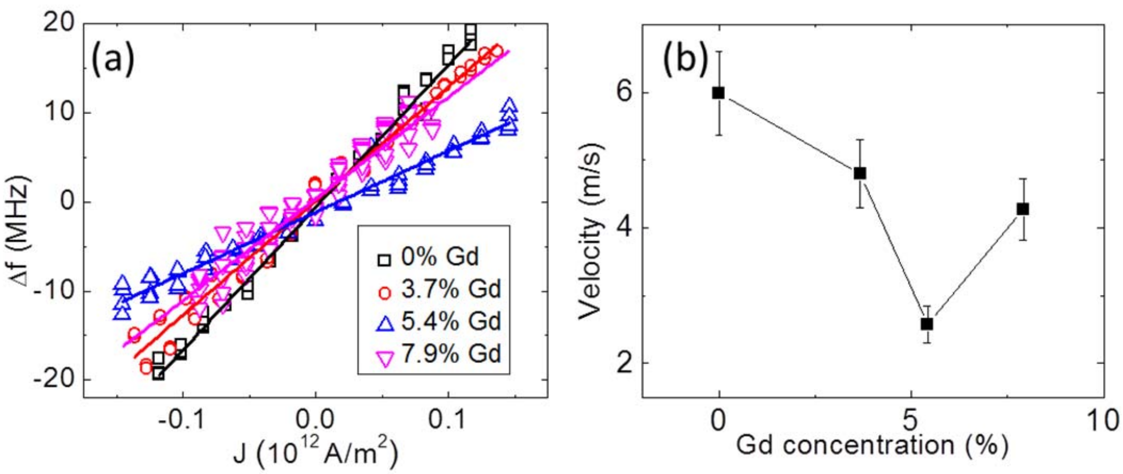

Figure 5.6: (a) The relative frequency shift, Δ*f*, as a function of applied current density for different PyGd alloys with linear fits. (b) Spin transfer velocity as a function of Gd concentration for a current density of 10^{11} A/m^2.

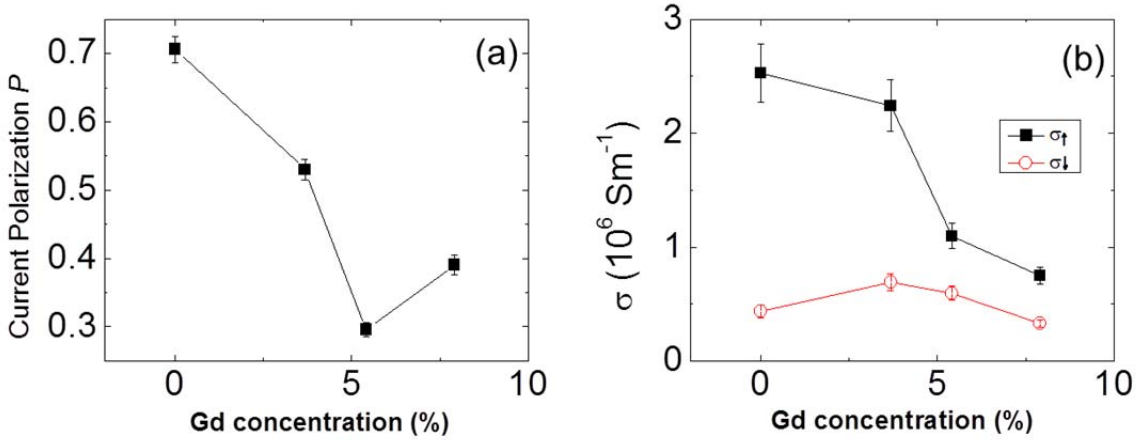

Figure 5.7: (a) Current polarization of PyGd alloys. (b) Spin-up and spin-down conductivities as a function of Gd concentration.

REFERENCES

[1] V. Vlaminck and M. Bailleul, "Current-induced spin-wave Doppler shift," *Science,* vol. 322, pp. 410-413, Oct 2008.

[2] M. Zhu, C. L. Dennis, and R. D. McMichael, "Temperature dependence of magnetization drift velocity and current polarization in $Ni_{80}Fe_{20}$ by spin-wave Doppler measurements," *Physical Review B,* vol. 81, 140407 Apr 2010.

[3] M. Zhu, B. D. Soe, R. D. McMichael, M. J. Carey, S. Maat, and J. R. Childress, "Enhanced magnetization drift velocity and current polarization in $(CoFe)_{(1-x)}Ge_x$ alloys," *Applied Physics Letters,* vol. 98, 072510, Feb 2011.

[4] S. Lepadatu, J. Claydon, D. Ciudad, A. Naylor, C. Kinane, S. Langridge, S. Dhesi, and C. Marrows, "Reduction of Threshold Current for Domain Wall Depinning Using Gd Doping of Permalloy," *Applied Physics Express,* vol. 3, 083002, Aug 2010.

[5] A. Fert and I. A. Campbell, "Electrical-resistivity of ferromagnetic nickel and iron based alloys," *Journal of Physics F-Metal Physics,* vol. 6, pp. 849-871, May 1976.

[6] R. D. McMichael and M. D. Stiles, "A new spin on the Doppler effect," *Science,* vol. 322, pp. 386-387, Oct 2008.

CHAPTER 6

DOMAIN WALL VELOCITY MEASUREMENTS

6.1 Overview of Domain Wall Velocity Measurement Techniques

Domain wall velocity directly relates to the operation speed of domain wall motion devices and is therefore one of the crucial parameters for establishing the viability of this technology. Obtaining an accurate measurement of the overall impact of doping on the domain wall velocity is critical to our study. Domain wall velocity measurements are utilized to confirm the results of our spin wave Doppler measurements. Measurements of domain wall velocities through ferromagnetic wires were first demonstrated using an inductive method developed by Sixtus and Tonks in 1931 [1]. Velocities can be determined by measuring the domain wall travel time between two sensing coils that have a known separation. This technique is very powerful but becomes more difficult as the induced voltage signal decreases with wire diameter. The speed of domain wall velocities that can be detected is also limited by the relaxation time of the pickup coils [2].

The magneto-optical analog of the Sixtus-Tonks technique uses the Kerr effect to accomplish a more direct measurement of the domain wall velocity and was first introduced in 1958 [3]. Time-resolved magneto-optical Kerr effect (MOKE) measurements can be performed on submicron magnetic wires and will be discussed more thoroughly in section 6.2. Another optical technique for obtaining current-induced domain wall motion measurements uses x-ray magnetic circular-dichroism photoemission electron microscopy, but a synchrotron is required for these types of measurements [4]. More recent electrical techniques measuring magnetoresistance values [5, 6] have been established providing more feasible alternatives to the Sixtus-Tonks method. Resistance measurements in real time are used to detect the propagation of domain walls and this technique can be easily scaled for small magnetic structures. The giant magnetoresistance effect is larger than the anisotropic magnetoresistance which in turn will yield better signal to noise ratios in GMR structures. Consequently, we identify time-resolved resistance measurement techniques for analyzing domain wall velocities through our GMR stacks.

6.2 Time-Resolved GMR Measurements

Time-resolved resistance measurements in GMR structures can provide direct evidence of domain wall motion using single-shot measurements. The experimental setup from Ref. [7] enables room temperature measurements and is therefore replicated. The voltage change that occurs as the magnetic orientation is altered in the GMR wire is separated through the RF path of a broadband bias tee while the DC component is filtered out. An ultra wide-band, high gain RF amplifier with a low noise factor is required to amplify the signal which is then detected by an oscilloscope that enables measurements of single-shot waveforms. Ground-signal-ground, 3-tip RF probes connected to contacts patterned with coplanar waveguide (CPW) geometry ensure low loss of the RF signals.

New devices were fabricated incorporating contacts in a CPW structure following the procedure outlined in Chapter 3. The dimension of the CPW contacts are determined by using the formulas provided in [8] and the dielectric constant of our Al_2O_3 ALD deposited films ($\varepsilon_r = 6.9$). The resistance of the CPW structure was designed to be 50 Ohms to match the impedance of the model 5575A bias tee manufactured by Picosecond Pulse labs. The Agilent Advanced Design System was used to perform RF characterization of our device design. The transmission parameters and Smith charts shown in Fig. 6.1 demonstrate that the CPW design meets our specifications through frequencies ranging from 1 MHz to 2 GHz.

An example device fabricated for these measurements with contacts in the CPW geometry along with the time-resolved GMR measurement setup is shown in Fig. 6.2. The GMR stacks are identical to the ones fabricated using e-beam evaporation and measured in Chapter 3. However, the magnetoresistance are an order of magnitude smaller in these GMR stacks when compared with our previous measurements. The measured GMR ratios for this chip were between 0.10-0.15% and the Permalloy layer did not exhibit sharp switching as visible in Fig. 6.3. Because good switching was observed in the Co layer and there were no visible defects in the magnetic wires, we eliminate problems with the physical structural of the wires.

We speculate that the Permalloy layer contains oxygen defects that reduce the magnetoresistance ratio and create additional pinning sites within the structure. These problems are caused by our e-beam evaporation system or due to oxidation of our deposition materials. Fabricating GMR stacks using other deposition tools was not possible because at least four metals must be deposited *in situ* and due to concerns of material contamination with some of the materials included in the stacks. Obtaining domain wall velocities through time-resolved resistance measurements in GMR structures was abandoned due to difficulties in fabricating stacks with appropriate magnetoresistance ratios and good quality magnetic thin films.

6.3 Magneto-Optical Kerr Effect (MOKE) Magnetometry

Because MOKE is an optical technique, measurements can be performed on single-layer wires rather than on spin valve structures. Consequently, devices for MOKE measurements can be deposited using our RF magnetron sputtering system. Domain wall velocity measurements can therefore be accomplished on our PyGd alloys using the MOKE technique since these alloys are deposited via co-sputtering techniques. Polarized light reflected from a magnetic material is analyzed for MOKE measurements. Kerr rotation is the small rotation in the polarization plane of the reflected light which is directly proportional to sample magnetization [9]. The three types of MOKE measurements characterized by the direction of the samples magnetization and plane of incidence are polar, longitudinal and transverse. We are only concerned with longitudinal MOKE as we are dealing with thin films that have in-plane anisotropy.

MOKE magnetometry was originally developed for thin film analysis and used for domain imaging as well as measuring hysteretic properties of magnetic materials [10]. MOKE instruments have made improvements in sensitivity and resolution and continue to be applicable in research involving nanomagnetism and magnetization dynamics. The spatial resolution of this technique is determined by the profile of the focused light source spot on the sample because the signal amplitude depends on the ratio of the area of the magnetic material to the area of the spot size. Using a continuous wave laser as the light source and focusing the beam to the diffraction-limited spot size with a scale of a few microns, Cowburn *et al.* first demonstrated that the properties of submicron nanomagnets could be analyzed by MOKE [11].

The temporal resolution of MOKE instruments has steadily improved so that this technique can be used to detect switching responses [12] and domain wall dynamics [13, 14]. Ultra-fast timescales can be achieved using femtosecond laser pulses or by using continuous wave lasers with high speed detectors [15]. To obtain sufficient signal-to-noise ratios with high speed detection, signal averaging of a repetitive process such as measurements of hysteresis loops or domain wall dynamics with repetitive excitations must be conducted. In addition to good temporal and spatial resolution, the MOKE technique also allows for easy manipulation of the sample. During measurements magnetic fields and currents can be applied to nucleate and propagate domains through the magnetic structures. Measurements of domain wall velocities propagated by fields [13, 14] or a combination of field and current [16] have been studied in Permalloy wires using MOKE measurements.

6.3.1 Experimental Methods for MOKE Measurements

High-bandwidth MOKE measurements are performed through collaboration with Dr. Geoffrey Beach's Spin Dynamics Group at the Massachusetts Institute of Technology. We analyze the effect of Gd dopants on the spin transfer efficiency of Permalloy. These provide the first domain wall velocity measurements performed on PyGd wires and enable comparisons with our Doppler measurements. In addition, domain wall depinning measurements are carried out to analyze the effect of doping on the spin torque efficiency.

Devices for these measurements were fabricated using e-beam lithography as described in Chapter 3 and co-sputtering techniques at NCSU to pattern and deposit PyGd wires with a width of ~550 nm and a thickness of ~30 nm capped in a ~4 nm layer of Ta. According to Fig. 2.2, this wire geometry is well beyond the phase boundary where vortex domain walls are energetically preferred over walls with a transverse spin structure. Consequently, vortex walls are nucleated and propagated in these measurements. Domain walls are nucleated by applying a voltage bias across the adjacent Cr(5 nm)/Au(100 nm) contact pads using a pulse generator to induce a current pulse through the contact wire perpendicular to the PyGd wire as previously described in Chapter 3. The remaining contact, spaced 20 μm from the domain wall nucleation contact line, is connected to a current source to apply a DC current through the magnetic wire. An optical image of the fabricated PyGd wires used for the domain wall velocity measurements is shown in Fig. 6.4.

The MOKE magnetometer utilized in this work consists of a continuous wave laser with a wavelength of 532 nm and a photomultiplier tube with a risetime of ~10 ns. A translational stage with a stage motion resolution of 50 nm is used to focus the beam spot and position the appropriate region of the ferromagnetic structure. The laser beam is focused by adjusting the vertical distance between the sample and microscope objective while scanning across the edge of a large pad of magnetic material on the substrate. The reflected intensity and differentiated intensity profile are recorded to determine the optimal position of the sample and the resulting diameter of the spot size. For these measurements, the laser beam was focused to a ~5.5 μm spot size.

The magnetic wire must then be positioned in the laser spot. The feature is positioned near the laser spot using an optical microscope and then reflected intensity scans in the x and y directions are used to determine the contact and wire positions. An example of the changes in reflected intensity is shown by the reflectivity map of one of the devices in Fig. 6.5. Three types of measurements were performed to analyze the effects of Gd dopants on the magnetization dynamics of Permalloy. The first type of measurement involves analyzing the non-adiabatic spin torque through current-assisted domain wall depinning measurements. Next, the dependence on field-driven domain wall velocity as a function of applied field is determined. Finally, domain wall velocity measurements with an applied current are measured to evaluate the velocity due to the adiabatic spin transfer torque.

6.3.2 Current-Assisted Domain Wall Depinning Fields

The depinning fields necessary to initiate domain wall motion are obtained for each composition by measuring hysteresis loops after a domain wall is nucleated within the wire. The hysteresis loops are asymmetric because the nucleated domain wall will only move toward the measurement position with a magnetic field applied in the same direction. The propagation field required to move existing domain walls toward the measurement position is referred to as the depinning field and is considerably lower than the field required to switch the wire's magnetization through nucleating and propagating domain walls.

Various amplitudes of DC currents are applied through the magnetic wires where positive currents denote the electron current in the same direction as domain wall propagation toward the measurement position. Positive currents will therefore exert a non-adiabatic spin transfer torque to the nucleated domain wall that will assist the depinning process. Negative currents should symmetrically impede domain wall depinning because the non-adiabatic spin transfer torque opposes the direction of propagation. However, Joule heating caused by the high current densities during the measurements and the adiabatic spin transfer torque also contribute to the domain wall depinning processes. We observe a decrease in the field required for domain wall depinning with large current densities regardless of the current direction as shown in Fig. 6.6. The effects of Joule heating and domain wall distortion due to the adiabatic spin transfer torque are expected to be the same for currents with opposite polarities so by measuring depinning fields with both the positive and negative currents we are able to separate these effects from non-adiabatic spin torque effects.

Depinning fields are measured as a function of applied currents for the PyGd compositions as shown in Fig. 6.7. The data is then fit to a second-order polynomial function. The quadratic term is caused by reduction of the pinning potential due to Joule heating within the wires and adiabatic torques. The linear term represents the non-adiabatic spin transfer contribution where the slope is indicative of the spin transfer efficiency, which is proportional to the current polarization and the non-adiabatic factor [17-19]. For doped compositions to exhibit larger spin transfer efficiencies than Permalloy, the Gd dopants must have a more significant impact on the non-adiabatic factor than on Permalloy's current polarization. The largest spin transfer efficiency is observed for Permalloy samples as expected due to significant reduction in current polarization as determined by our spin wave Doppler measurements in Chapter 5.

However, the results for the $Py_{0.946}Gd_{0.054}$ and $Py_{0.921}Gd_{0.079}$ compositions are quite unexpected. The linear terms in the fits of these compositions are positive indicating negative spin transfer efficiencies. To ensure this effect is not an artifact of our measurement configuration, we repeated measurements on several samples using both positive and negative current steps and domain walls with both head-to-head and tail-to-tail configurations consistently yielding the same effect. Because the sign of the current polarization does not change, this reversal in efficiency must occur because of a negative β value. Negative non-adiabatic spin torque has never been experimentally observed, although it is possible in theory [20, 21]. However, negative β values proposed in theory require special circumstances such as holelike carriers at the Fermi energy [20] or narrow domain walls [21]. The PyGd alloys do not have holelike carriers because they are metals where the current is carried by electrons. Permalloy and PyGd compositions have relatively large domain walls because their magnetization is parallel to the film plane.

Additional measurements where domain walls are depinned from notches within the magnetic wires will provide more insight into the impact of Gd dopants on the non-adiabatic factor of Permalloy. Materials with negative β values do not provide apparent advantages in domain wall devices because the magnitude of β is the significant factor. However, these results provide information about the nature of the non-adiabatic spin torque which can be used to optimize the interaction between spin polarized currents and domain walls. The β/α ratio depends on the details of the band structure and better microscopic understanding of these alloys and the spin scattering mechanisms caused by Gd dopants is necessary to determine the reasoning for this unexpected phenomenon.

6.3.3 Field-Driven Domain Wall Velocity Measurements

Time-resolved propagation measurements were conducted by measuring the MOKE reversal transients at several positions along a wire. An example of a typical reversal transient is shown in Fig. 6.8(a). Wall propagation is confirmed because domain wall arrival times increase linearly with the distance from the nucleation site as shown for a constant field of 35.6 Oe in Fig. 6.8(b). The average velocity of each wall is obtained from the inverse slope of arrival time versus position. These velocities are plotted versus applied magnetic fields for all compositions in Fig. 6.9. The minimum and maximum measured velocities are 17.3 m/s for $Py_{0.875}Gd_{0.125}$ to 127.8 m/s for Permalloy respectively.

The maximum propagation fields that can be measured decrease with Gd concentration because the domain nucleation fields are reduced. The $Py_{0.946}Gd_{0.054}$ sample yields larger average velocities than the Permalloy sample in its measured field range. The faster velocities for the doped samples at equal magnetic fields is due to the reduced magnetization in doped samples causing Walker breakdown at lower fields as described by Equation 2.7. Consequently, the average velocities in the linear regime after Walker breakdown are higher for the doped alloys than for Permalloy at constant fields. The average domain wall mobility in this regime is also expected to be higher due to the increase in the Gilbert damping factor. As a result, incorporating Gd doped alloys in devices using magnetic field propagation will yield velocities comparable to Permalloy at lower drive fields.

The magnetic fields applied in these measurements are well above the Walker breakdown field for Permalloy. The linearity of the measurements proves that we are beyond Walker breakdown in the precessional regime where the adiabatic torque dominates over the non-adiabatic contribution for all compositions. The current-assisted domain wall velocity measurements described in the next section are performed with the assistance of an external magnetic field to overcome pinning and isolate the contribution of the effect of spin torque on the domain wall motion. The fields applied during these measurements are shown by the arrows in Fig. 6.9 for each composition.

6.3.4 Current-Assisted Domain Wall Velocity Measurements

Domain wall propagation by a combination of field and current is analyzed to determine the effect of the adiabatic spin torque on domain wall velocity. Since these measurements are conducted above Walker breakdown, the change in velocity due to an applied current is equivalent to the spin transfer velocity. Positive currents increase the measured values for domain wall velocities while negative currents linearly reduce the domain wall velocity as consistent with expectations. The average velocities resulting from the combination of drive fields and current densities for samples with different Gd content are shown in Fig. 6.10(a). The current-dependent change in velocity is plotted with values normalized to eliminate the effect of different magnetic drive field amplitudes as shown in Fig. 6.10(b).

Spin transfer velocities for a current density of 10^{11} A/m^2 are determined from the slopes of the linear fit for each composition and are plotted as a function of Gd content in Fig. 6.11. Adding Gd dopants to Permalloy monotonically reduces its spin transfer velocity. These results correspond to the values obtained by our previous spin wave Doppler measurements. Both techniques reveal a 30% drop in spin transfer velocity as the Gd concentration increases from 0-7.9%. Unlike the spin wave Doppler technique, MOKE measurements can be performed on materials with high Gilbert damping values. An alloy with 12.5% Gd content was therefore measured to examine the effect of further Gd doping. The minimum value for the spin transfer velocity of (2.4 ±0.2) m/s was found at this composition which is a fractional reduction of 41% from the value for Permalloy. Our results confirm earlier conclusions that Gd dopants have a significant impact on the polarization of Permalloy which is detrimental to the spin transfer velocity despite the reduction in magnetization.

6.3 Summary

We have shown the first domain wall velocity measurements performed on PyGd alloys demonstrating the effects of doping on domain wall dynamics. Three different types of measurements were performed utilizing the MOKE technique and combinations of magnetic and current-induced domain wall propagation. A previous study published by Lepadatu *et al.* indicates Gd dopants in Permalloy are useful for enhancing the performance of spin transfer torque devices suggesting a 275% increase to the non-adiabatic factor with only a small change in the adiabatic spin transfer velocity at 10% Gd concentration [22]. The current-assisted domain wall velocity measurements show that Gd dopants have a negative effect on the adiabatic spin transfer velocity agreeing with our spin wave Doppler measurements but contrasting the results obtained in Ref. [22].

The MOKE depinning measurements that show the largest spin transfer efficiency for Permalloy also differ significantly from the results obtained by Lepadatu *et al.* [22]. Our depinning measurements indicate a decrease in the non-adiabatic factor as a result of Gd dopants. Surprisingly, negative spin transfer efficiencies were seen in the $Py_{0.946}Gd_{0.054}$ and $Py_{0.921}Gd_{0.079}$ compositions that must be due to a negative non-adiabatic spin torque effect. This behavior is consistently observed in the measurements but is not well understood and appears to be an effect of spin-flip scattering. While negative β values will not directly enhance domain wall based devices since the magnitude of domain wall velocity is dependent on the amplitude of the non-adiabatic factor, these findings will improve understanding of the interaction between domain walls and spin-polarized currents which will lead to faster, more efficient spin torque devices.

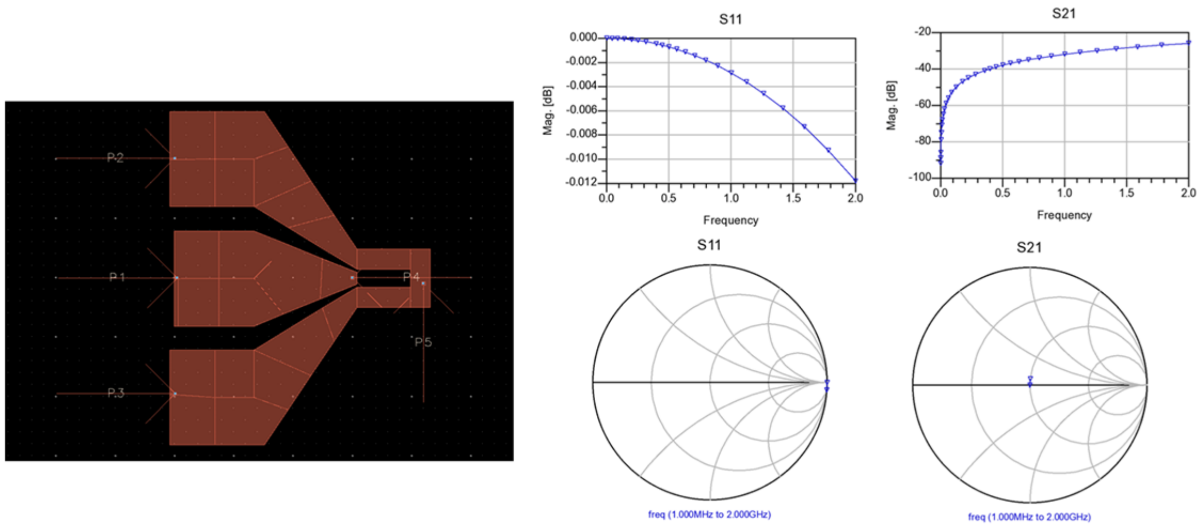

Figure 6.1: Simulation of CPW contacts using Agilent Advanced Design System software to confirm impedance matching between the device and bias tee necessary to optimize signal transmission.

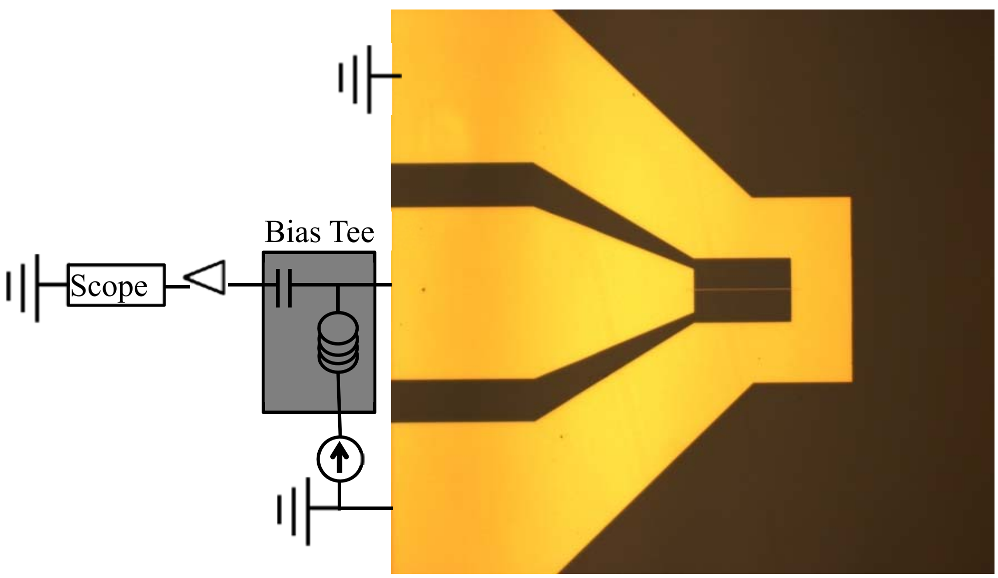

Figure 6.2: Optical microscope image of device for time-resolved resistance measurements with CPW contact geometry to ensure low loss signal transmission of the RF signals. A schematic of the measurements setup is also shown where the voltage change due to the magnetic orientation of the GMR wire (shown here as the thin horizontal line) is measured over the RF path of the bias tee by a RF amplifier and the oscilloscope.

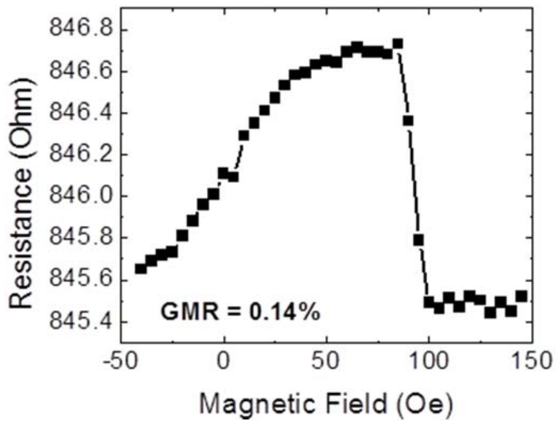

Figure 6.3: GMR measurements for stacks fabricated along with devices for electrical domain wall velocity measurements. The resistance ratio is an order of magnitude smaller than for the GMR stacks measured in Chapter 3. The reduced GMR ratio and gradual magnetization change in the Permalloy layer indicate problems with the film quality.

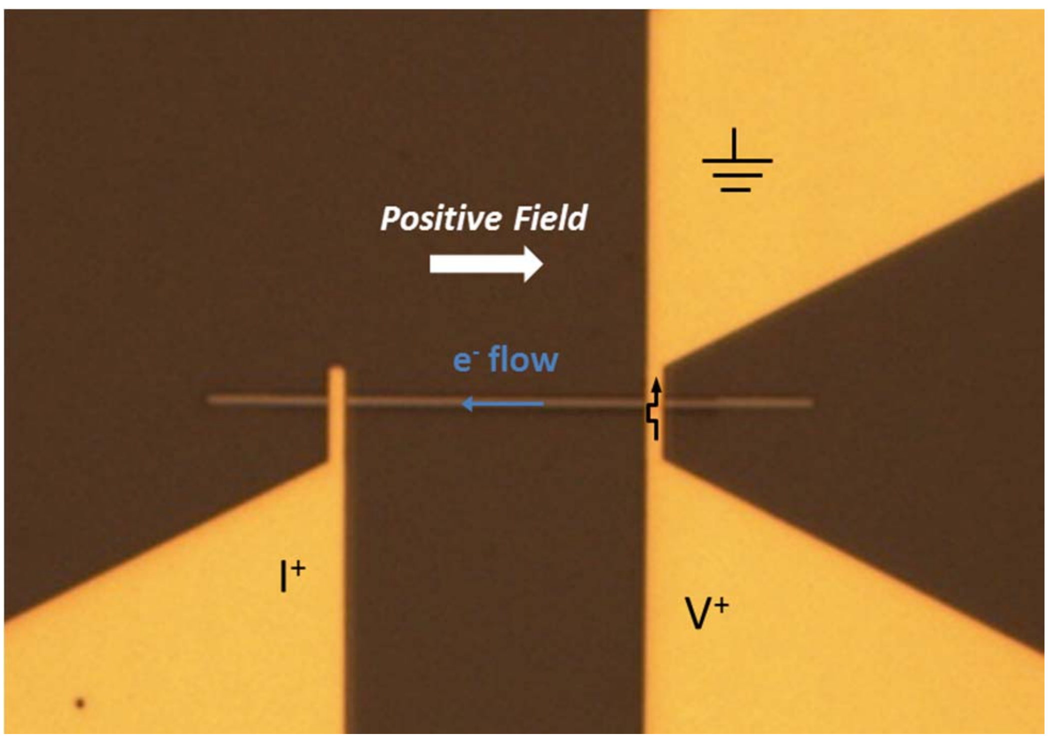

Figure 6.4: Optical microscope image of a fabricated ~550 nm PyGd wire for MOKE measurements. Domain walls are nucleated by applying a voltage pulse across the connected contacts shown on the left side of the device. Domain walls are propagated to measured locations with a negative field. The blue arrow in the image shows that a positive current results in the direction of electron flow in the same direction as the propagation direction for the nucleated wall.

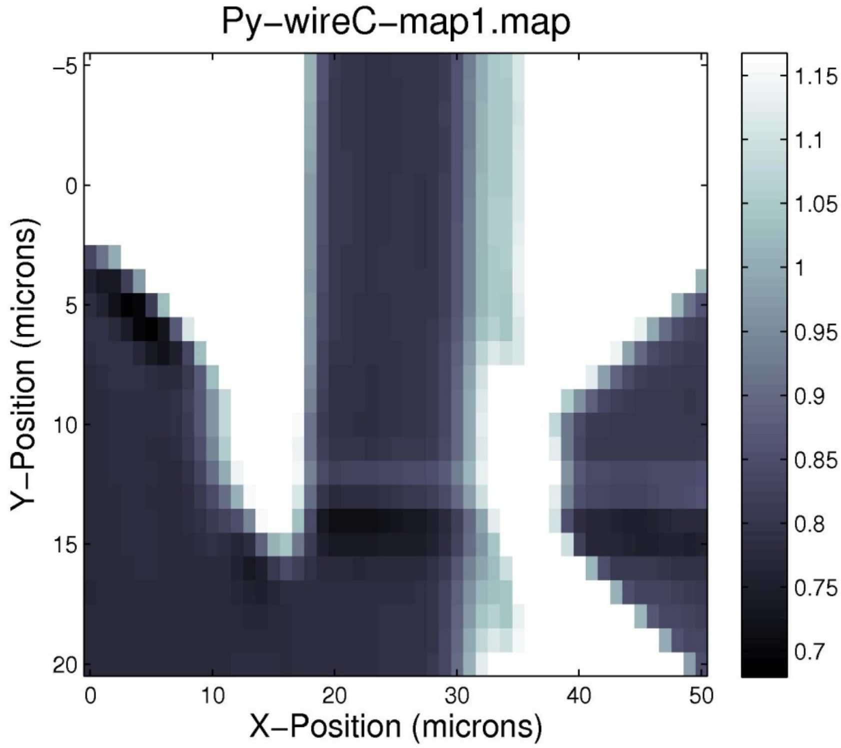

Figure 6.5: Reflectivity map of fabricated structures used to precisely position the magnetic wire within the MOKE laser spot.

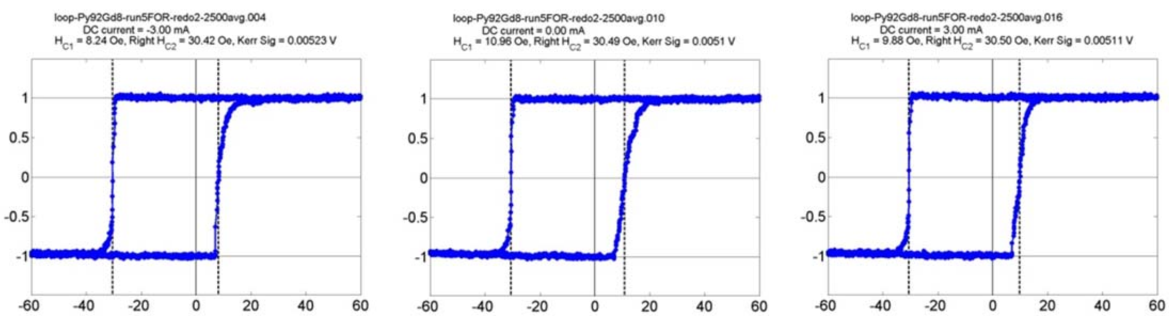

Figure 6.6: Hysteresis loops of $Py_{0.921}Gd_{0.077}$ wire measured by MOKE showing small shifts in depinning fields with applied current due to Joule heating. The difference between the depinning fields with opposite current polarities is attributed to the effective magnetic field caused by spin transfer torque.

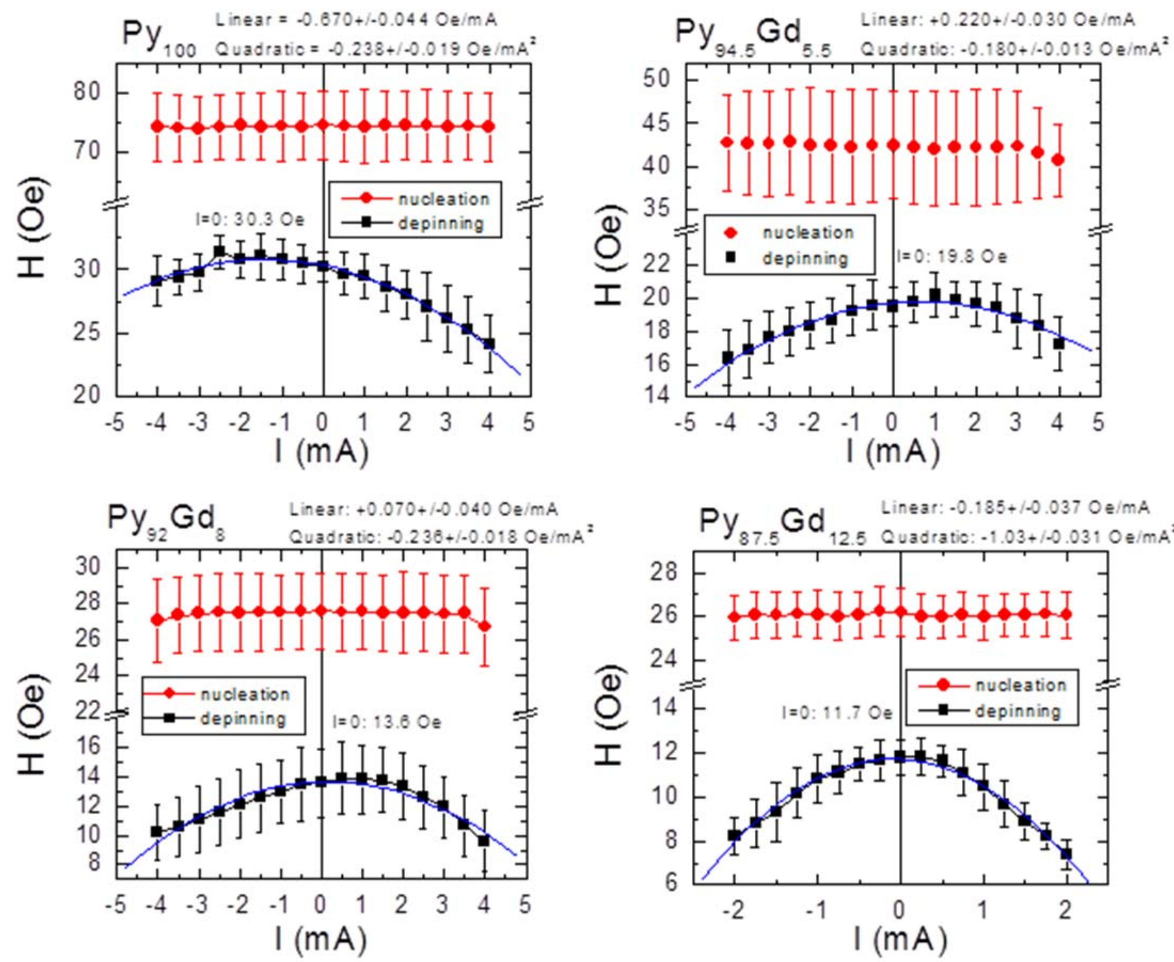

Figure 6.7: Average coercive fields (red circles) and depinning fields (black squares) obtained from hysteretic curves for each PyGd composition with quadratic fits. Error bars represent the standard deviation of values between measurements on three devices. The quadratic term is caused by thermally assisted depinning due to Joule heating in the wires. The linear term represents the spin torque contribution. The positive linear slopes for the Py$_{0.946}$Gd$_{0.054}$ and Py$_{0.921}$Gd$_{0.079}$ compositions indicate negative spin transfer efficiencies.

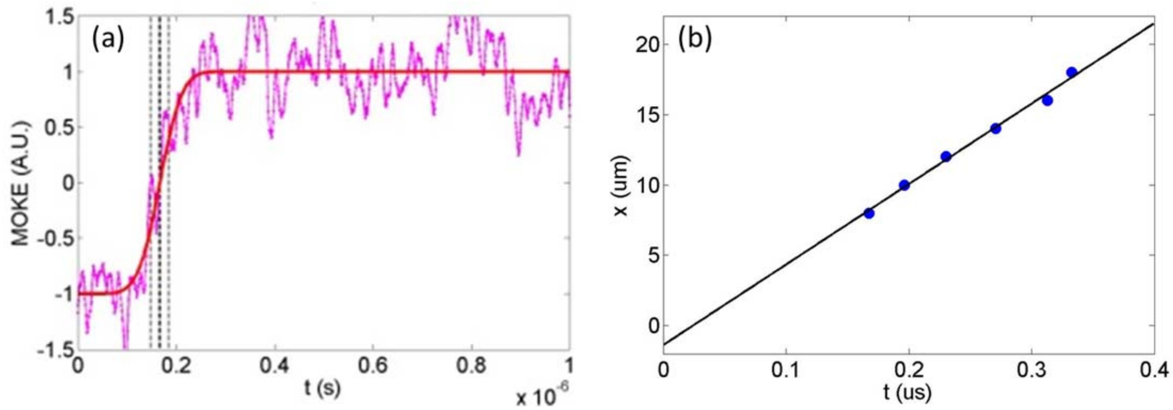

Figure 6.8: (a) Time-resolved MOKE signal (pink line) with fit to the error function (red line) and (b) domain wall arrival time as a function of position from the nucleation site in response to a 35.6 Oe field.

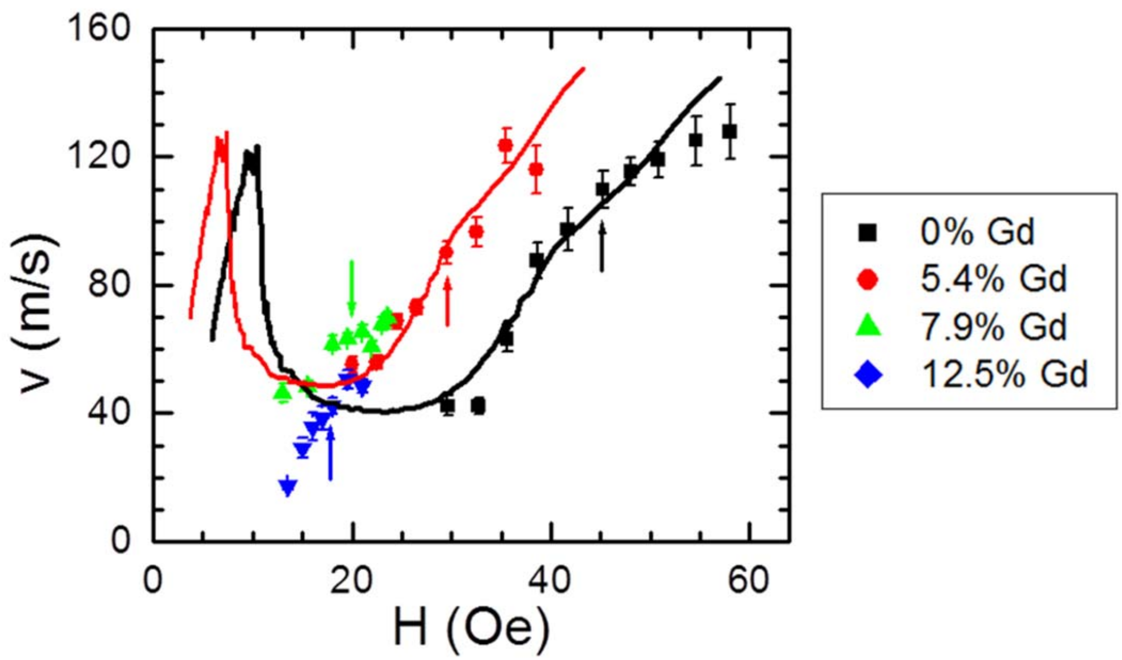

Figure 6.9: Domain wall velocities as a function of driving fields for different PyGd alloys. Compositions with 5.4% Gd content exhibit higher average velocities that Permalloy with the same drive field. Solid lines show overlaid experimental mobility curves published in Ref. [23]. Colored arrows indicate the drive fields at which the current-assisted velocities are measured.

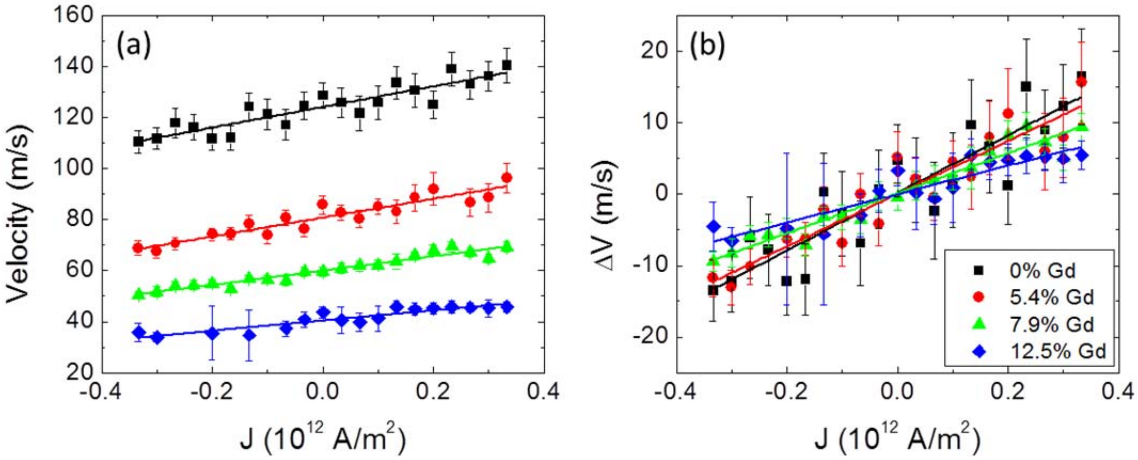

Figure 6.10: (a) Measured velocities versus applied current densities at drive fields with linear fits. (b) Normalized measurements demonstrating the change in velocity due to the applied current densities.

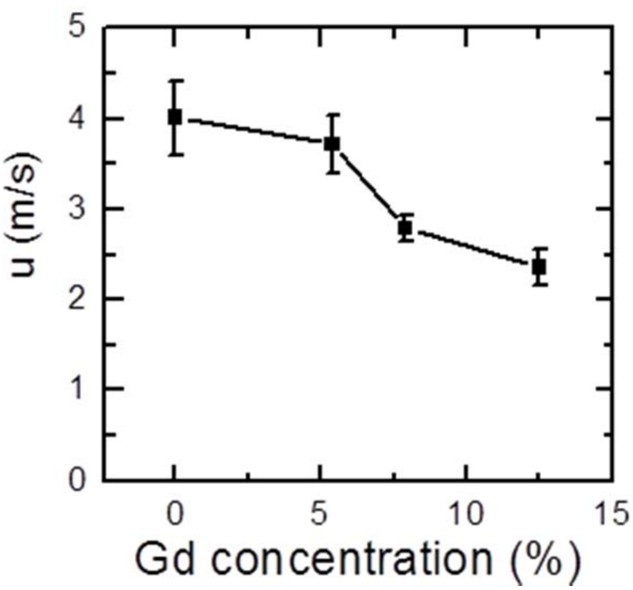

Figure 6.11: Spin transfer velocity as a function of Gd concentration for a current density of 10^{11} A/m^2 measured by MOKE measurements.

REFERENCES

[1] K. J. Sixtus and L. Tonks, "Propagation of large Barkhausen discontinuities," *Physical Review,* vol. 37, pp. 930-958, Apr 1931.

[2] A. Chizhik, R. Varga, A. Zhukov, J. Gonzalez, and J. M. Blanco, "Kerr-effect based Sixtus-Tonks experiment for measuring the single domain wall dynamics," *Journal of Applied Physics,* vol. 103, 07E707, Apr 2008.

[3] E. W. Lee and D. R. Callaby, "Direct measurement of the velocity of propagation of a ferromagnetic domain boundary in 'Perminvar'," *Nature,* vol. 182, pp. 254-255, Jul 1958.

[4] T. A. Moore, M. Klaui, L. Heyne, P. Mohrke, D. Backes, J. Rhensius, U. Rudiger, L. J. Heyderman, J. U. Thiele, G. Woltersdorf, C. H. Back, A. F. Rodriguez, F. Nolting, T. O. Mentes, M. A. Nino, A. Locatelli, A. Potenza, H. Marchetto, S. Cavill, and S. S. Dhesi, "Scaling of spin relaxation and angular momentum dissipation in permalloy nanowires," *Physical Review B,* vol. 80, 132403, Oct 2009.

[5] T. Ono, H. Miyajima, K. Shigeto, K. Mibu, N. Hosoito, and T. Shinjo, "Propagation of the magnetic domain wall in submicron magnetic wire investigated by using giant magnetoresistance effect," *Journal of Applied Physics,* vol. 85, pp. 6181-6183, Apr 1999.

[6] M. Hayashi, L. Thomas, Y. B. Bazaliy, C. Rettner, R. Moriya, X. Jiang, and S. S. P. Parkin, "Influence of current on field-driven domain wall motion in permalloy nanowires from time resolved measurements of anisotropic magnetoresistance," *Physical Review Letters,* vol. 96, 197207, May 2006.

[7] S. Glathe, R. Mattheis, and D. V. Berkov, "Direct observation and control of the Walker breakdown process during a field driven domain wall motion," *Applied Physics Letters,* vol. 93, 072508, Aug 2008.

[8] S. Jahn, M. Margraf, V. Habchi, and R. Jacob, "Coplanar waveguides (CPW)," http://qucs.sourceforge.net/tech/node86.html.

[9] D. T. Pierce, "Spin-polarized electron-microscopy," *Physica Scripta,* vol. 38, pp. 291-296, Aug 1988.

[10] D. A. Allwood, G. Xiong, M. D. Cooke, and R. P. Cowburn, "Magneto-optical Kerr effect analysis of magnetic nanostructures," *Journal of Physics D-Applied Physics,* vol. 36, pp. 2175-2182, Sep 2003.

[11] R. P. Cowburn, D. K. Koltsov, A. O. Adeyeye, and M. E. Welland, "Probing submicron nanomagnets by magneto-optics," *Applied Physics Letters,* vol. 73, pp. 3947-3949, Dec 1998.

[12] M. R. Freeman and A. K. Hiebert, "Stroboscopic microscopy of magnetic dynamics," in *Spin Dynamics in Confined Magnetic Structures I.* vol. 83, B. Hillebrands and K. Ounadjela, Eds. Berlin: Springer-Verlag Berlin, 2002, pp. 93-126.

[13] D. Atkinson, D. A. Allwood, G. Xiong, M. D. Cooke, C. C. Faulkner, and R. P. Cowburn, "Magnetic domain-wall dynamics in a submicrometre ferromagnetic structure," *Nature Materials,* vol. 2, pp. 85-87, Feb 2003.

[14] G. S. D. Beach, C. Nistor, C. Knutson, M. Tsoi, and J. L. Erskine, "Dynamics of field-driven domain-wall propagation in ferromagnetic nanowires," *Nature Materials,* vol. 4, pp. 741-744, Oct 2005.

[15] C. Nistor, G. S. D. Beach, and J. L. Erskine, "Versatile magneto-optic Kerr effect polarimeter for studies of domain-wall dynamics in magnetic nanostructures," *Review of Scientific Instruments,* vol. 77, 103901, Oct 2006.

[16] G. S. D. Beach, C. Knutson, C. Nistor, M. Tsoi, and J. L. Erskine, "Nonlinear domain-wall velocity enhancement by spin-polarized electric current," *Physical Review Letters,* vol. 97, 057203, Aug 2006.

[17] J. He, Z. Li, and S. Zhang, "Current-driven domain-wall depinning," *Journal of Applied Physics,* vol. 98, 016108, Jul 2005.

[18] J. V. Kim and C. Burrowes, "Influence of magnetic viscosity on domain wall dynamics under spin-polarized currents," *Physical Review B,* vol. 80, p. 8, Dec 2009.

[19] O. Boulle, J. Kimling, P. Warnicke, M. Klaui, U. Rudiger, G. Malinowski, H. J. M. Swagten, B. Koopmans, C. Ulysse, and G. Faini, "Nonadiabatic Spin Transfer Torque in High Anisotropy Magnetic Nanowires with Narrow Domain Walls," *Physical Review Letters,* vol. 101, 216601, Nov 2008.

[20] I. Garate, K. Gilmore, M. D. Stiles, and A. H. MacDonald, "Nonadiabatic spin-transfer torque in real materials," *Physical Review B,* vol. 79, 104416, Mar 2009.

[21] S. Bohlens and D. Pfannkuche, "Width Dependence of the Nonadiabatic Spin-Transfer Torque in Narrow Domain Walls," *Physical Review Letters,* vol. 105, 177201, Oct 2010.

[22] S. Lepadatu, J. Claydon, D. Ciudad, A. Naylor, C. Kinane, S. Langridge, S. Dhesi, and C. Marrows, "Reduction of Threshold Current for Domain Wall Depinning Using Gd Doping of Permalloy," *Applied Physics Express,* vol. 3, 083002, Aug. 2010.

[23] G. S. D. Beach, M. Tsoi, and J. L. Erskine, "Current-induced domain wall motion," *Journal of Magnetism and Magnetic Materials,* vol. 320, pp. 1272-1281, Apr 2008.

CHAPTER 7

CONCLUSIONS AND FUTURE WORK

7.1 Conclusions

In this work, the impact of rare-earth dopants on the magnetization dynamics of Permalloy has been explored to provide better understanding of current-induced domain wall motion. It has been suggested that because dopants cause spin-flip scattering they can be expected to increase the non-adiabatic factor [1]. Rare-earth elements were identified as dopants that may additionally enhance spin transfer torque effects due to antiferromagnetic coupling with the ferromagnetic transition metals. Specifically Gd dopants were selected since they cause a negligible effect on the Gilbert damping parameter of Permalloy [2, 3]. Novel magnetic alloys were created by co-sputtering Gd with ferromagnetic transition metals or their alloys and adjusting the RF power applied to the Gd sputter source to achieve different compositions.

Initial characterization of NiGd, CoGd and PyGd alloys included studying static magnetic properties by analyzing hysteresis loops obtained through SQUID magnetometry. Film magnetization decreases linearly with Gd content up to the compensated composition. Gd dopants cause a greater impact on the magnetization of Ni because Gd has 12.5 times more Bohr magnetons per atom than Ni at 0 K. The NiGd alloy reaches compensation when the Gd concentration is ~7.7% and further doping causes a dramatic increase in magnetization since the Gd atoms dominate the external magnetization of the film. The coercivity of each alloy series was also obtained as a function of Gd concentration. The film coercivity reduces significantly when the alloys transition to an amorphous structure as verified by XRD measurements. Compositions with low magnetization suggest possible increases in the spin transfer velocity while compositions with low coercive fields require less energy to nucleate a domain wall and reduce domain wall pinning. The SQUID measurements identify several compositions that may enhance domain wall dynamics such as $Co_{0.818}Gd_{0.182}$.

Permalloy has a Gilbert damping factor that is significantly lower than Ni and Co and accordingly significant effort has gone into understanding domain wall motion through Permalloy wires. Consequently, the majority of this study is focused on measuring the effects of Gd dopants on the magnetization dynamics of Permalloy. FMR measurements performed on unpatterned PyGd films confirm Gd dopants produce a modest increase in the damping parameter of Permalloy and indicate high-quality uniform films. An increase in film resistivity associated with the destruction of film crystallinity is also observed. Consequently, Joule heating occurring due to high current densities required for domain wall motion is more of a concern in film compositions with higher Gd content.

Spin wave Doppler measurements were performed to measure the spin transfer velocity and the current polarization in current-carrying PyGd alloy wires. Although decreased magnetization values should result in an increase to the spin transfer velocity, the ultimate effect is dependent the effect doping has on the current polarization. The current-induced spin wave Doppler technique is a reliable method for measuring the current polarization because it is immune to interfacial effects at contacts and inadvertent defects in the wire structure. We measure a decrease in the current polarization upon introducing Gd dopants corresponding to an overall decrease in the spin transfer velocity. Because Gd dopants decrease magnetization while augmenting damping values, the amplitude of the spin wave transmission signals reduce as a function of Gd content. Consequently, measurements of alloys with higher Gd content are not obtainable using this technique because the transmission signals are insufficient for detecting frequency shifts.

Submicron magnetic wires were fabricated to perform physical domain wall velocity measurements to corroborate the accuracy of the spin wave Doppler measurements. Two separate aligned layers of EBL were required to create magnetic wires with electrical contacts. The non-magnetic contacts are used to nucleate domain walls within the nanowires and to apply currents through the wire that generate spin torque. Our fabrication process had to be optimized to reduce edge roughness caused by complications in combining conformal sputter deposition with lift-off techniques. Although a bilayer PMMA resist structure was used to promote liftoff, significant amounts of extra material were deposited on the sidewalls of our resist structures and adhered to the wire edges. A sufficient undercut was achieved by incorporating a LOR in the bilayer resist structure as verified by cross-sectional SEM images. FIB milling was examined to further reduce edge roughness in the magnetic wires but was abandoned because Ga^+ ion implantation degraded magnetic properties of the wires.

MOKE measurements were performed to measure domain wall velocities and analyze the spin transfer efficiency as a function of Gd content through depinning measurements. PyGd alloys with higher Gd concentration than obtainable by the spin wave Doppler measurements were also assessed. The MOKE measurements provide good agreement with our previous spin wave Doppler measurements confirming that Gd dopants reduce the adiabatic spin transfer velocity. The $Py_{0.875}Gd_{0.125}$ alloy extends the range of measured compositions and confirms that the adiabatic spin torque effect continues to decrease. Domain wall depinning measurements evaluate the overall spin transfer efficiency including non-adiabatic effects. These measurements conclude that Gd dopants are also detrimental to the non-adiabatic spin torque. Two of our compositions even show a negative non-adiabatic spin torque effect indicating negative β values.

We conclude that although PyGd alloys demonstrate potential to enhance domain wall dynamics through static magnetic measurements, introducing dopants to Permalloy negatively affects several parameters that dominate magnetization dynamics. Dopants reduce magnetization in Permalloy but also reduce its current polarization yielding a reduction in spin transfer velocity as measured by the spin wave Doppler technique and verified through time-resolved MOKE measurements. Domain wall depinning measurements analyzed by MOKE also show degradation of the non-adiabatic spin torque effects upon introducing Gd dopants. This work provides important insights into the mechanisms of current-induced domain wall propagation and the effects of doping on magnetization dynamics.

7.2 Future Work

Because magnetization dynamics are directly related to material properties, further work in materials engineering is necessary to increase understanding of domain wall dynamics. Studying a wide variety of materials for domain wall dynamics will lead to optimization of magnetization dynamics and will improve the specifications for domain wall motion devices. We propose future work in further exploring PyGd alloys as well as investigating several other types of material systems.

7.2.1 More Current-Assisted Domain Wall Depinning Measurements

The results of the current-assisted domain wall depinning measurements indicate a reduction in non-adiabatic effects as a result of Gd dopants. These results are contrary to expectations due to increased spin-flip scattering and previously published values [4]. The mechanisms that are causing negative non-adiabatic factors are not known. We propose to repeat the current-assisted depinning measurements using a fabricated artificial pinning site to initially pin the domain wall. The depinning probability as a function of current pulse length can then be examined to evaluate current induced dynamic parameters as previously demonstrated in Permalloy wires [5]. These measurements could be compared with our depinning measurements that used only intrinsic pinning and would provide quantitative values for non-adiabatic terms and better understanding of the unexpected negative spin efficiencies observed in this work.

7.2.2 Temperature Dependence of PyGd Alloys

We have verified that Gd dopants in Permalloy produce an amorphous transition which is complete with a Gd concentration of 7.9%. Greater variation was found between Doppler measurements of $Py_{0.921}Gd_{0.079}$ samples. This composition represents the only XRD amorphous alloy measured using the spin wave Doppler technique. We suspect that this variation may be due to changes in the microstructure of these films as a result of the heating at large current densities applied during measurements. This theory could be verified by completing an annealing study. Amorphous alloys have been annealed to reduce stresses in films as well as control anisotropy [6]. The effect of different annealing conditions on the crystalline, static and dynamic properties of the initially amorphous highly doped PyGd alloys would improve understanding of this material system and increase understanding of the impact of film microstructure on domain wall dynamics.

The Curie temperature for bulk Gd is very close to room temperature while the Curie temperature for a 50 nm thin film moderately reduces to 250 K [7]. The temperature dependence of current polarization in Permalloy has been studied using the same spin wave Doppler measurement setup used in this work [8]. The magnetic moment of Gd atoms increase much more significantly than Permalloy atoms over the temperature range from 80 K to 300 K due to the proximity of the Curie temperature of Gd. We suspect that reduced temperatures will also have a more significant impact on the spin transfer velocity and current polarization in PyGd alloy wires. Using the spin wave Doppler technique to measure the temperature dependence on PyGd alloys will further characterize these materials. Current polarization is a key parameter in spin transfer effects and these measurements will also enable better understanding of the impact of material modulation on this parameter.

7.2.3 Materials with Perpendicular Magnetic Anisotropy

Materials exhibiting PMA are generating much interest because they offer several advantages over Permalloy and other materials with in-plane magnetization. High thermal stability is achieved by using PMA materials which enables closer spacing of neighboring domains within the wires [12]. Smaller domain wall widths occurring in PMA wires enhance the non-adiabatic effects requiring lower threshold current densities for current-induced domain wall motion and increasing the non-adiabatic factor [13]. Domain wall velocity measurements have recently been performed in PMA wires [14, 15]. The strength of the PMA in Co/Pt multilayers can be tuned by varying the thickness of the Co layer or the type of buffer layer upon which the stack is grown [16]. We propose a study to compare domain wall dynamics in Co/Pt multilayers exhibiting magnetic anisotropies that differ in magnitude and in their plane of magnetization. A systematic study based on the dependence of current-driven domain wall dynamics on the strength of a material's PMA will further promote understanding of current induced domain wall dynamics.

7.2.4 Materials with Large Current Polarizations

Materials with high current polarizations are promising for increasing domain wall velocities and reducing the critical current density required for domain wall propagation. CoFeGe alloys are of interest for current perpendicular to the plane (CPP) spin valves for recording read-head sensors [9]. Current polarizations for these alloys with 20-30% Ge content are very close to 1 and the spin transfer velocity measured by the spin wave Doppler technique is larger for the $(CoFe)_{0.70}Ge_{0.30}$ composition than the value we obtained for Permalloy [10]. In addition, the Gilbert damping parameter measured for this composition after being annealed in vacuum at 245° C for 5 hours is significantly lower than the modest values measured for Permalloy [11]. CoFeGe alloys should therefore exhibit better domain wall dynamics than Permalloy and need to be further investigated for domain wall motion applications.

REFERENCES

[1] A. Thiaville, Y. Nakatani, J. Miltat, and Y. Suzuki, "Micromagnetic understanding of current-driven domain wall motion in patterned nanowires," *Europhysics Letters,* vol. 69, pp. 990-996, Mar 2005.

[2] W. Bailey, P. Kabos, F. Mancoff, and S. Russek, "Control of magnetization dynamics in Ni81Fe19 thin films through the use of rare-earth dopants," *Ieee Transactions on Magnetics,* vol. 37, pp. 1749-1754, Jul 2001.

[3] G. Woltersdorf, M. Kiessling, G. Meyer, J. U. Thiele, and C. H. Back, "Damping by Slow Relaxing Rare Earth Impurities in Ni80Fe20," *Physical Review Letters,* vol. 102, 257602, Jun 2009.

[4] S. Lepadatu, J. Claydon, D. Ciudad, A. Naylor, C. Kinane, S. Langridge, S. Dhesi, and C. Marrows, "Reduction of Threshold Current for Domain Wall Depinning Using Gd Doping of Permalloy," *Applied Physics Express,* vol. 3, 083002, Aug 2010.

[5] M. Hayashi, L. Thomas, C. Rettner, R. Moriya, and S. S. P. Parkin, "Dynamics of domain wall depinning driven by a combination of direct and pulsed currents," *Applied Physics Letters,* vol. 92, 162503, Apr 2008.

[6] H. Gavrila and V. Ionita, "Crystalline and amorphous soft magnetic materials and their applications - Status of art and challenges," *Journal of Optoelectronics and Advanced Materials,* vol. 4, pp. 173-191, Jun 2002.

[7] R. Ranchal, C. Aroca, M. Maicas, and E. Lopez, "Temperature dependence of the magnetic and electrical properties of Permalloy/gadolinium/Permalloy thin films," *Journal of Applied Physics,* vol. 102, 053904, Sep 2007.

[8] M. Zhu, C. L. Dennis, and R. D. McMichael, "Temperature dependence of magnetization drift velocity and current polarization in Ni80Fe20 by spin-wave Doppler measurements," *Physical Review B,* vol. 81, 140407, Apr 1 2010.

[9] S. Maat, M. J. Carey, and J. R. Childress, "Current perpendicular to the plane spin-valves with CoFeGe magnetic layers," *Applied Physics Letters,* vol. 93, 143505, Oct 2008.

[10] M. Zhu, B. D. Soe, R. D. McMichael, M. J. Carey, S. Maat, and J. R. Childress, "Enhanced magnetization drift velocity and current polarization in (CoFe)(1-x)Ge-x alloys," *Applied Physics Letters,* vol. 98, 072510, Feb 2011.

[11] H. Lee, Y. H. A. Wang, C. K. A. Mewes, W. H. Butler, T. Mewes, S. Maat, B. York, M. J. Carey, and J. R. Childress, "Magnetization relaxation and structure of CoFeGe alloys," *Applied Physics Letters,* vol. 95, 082502, Aug 2009.

[12] S. Mangin, D. Ravelosona, J. A. Katine, M. J. Carey, B. D. Terris, and E. E. Fullerton, "Current-induced magnetization reversal in nanopillars with perpendicular anisotropy," *Nature Materials,* vol. 5, pp. 210-215, Mar 2006.

[13] S. Fukami, T. Suzuki, N. Ohshima, K. Nagahara, and N. Ishiwata, "Micromagnetic analysis of current driven domain wall motion in nanostrips with perpendicular magnetic anisotropy," *Journal of Applied Physics,* vol. 103, 07E718, Apr 2008.

[14] T. A. Moore, I. M. Miron, G. Gaudin, G. Serret, S. Auffret, B. Rodmacq, A. Schuhl, S. Pizzini, J. Vogel, and M. Bonfim, "High domain wall velocities induced by current in ultrathin Pt/Co/AlOx wires with perpendicular magnetic anisotropy," *Applied Physics Letters,* vol. 93, 262504, Dec 29 2008.

[15] M. Cormier, A. Mougin, J. Ferre, J. P. Jamet, R. Weil, J. Fassbender, V. Baltz, and B. Rodmacq, "Fast propagation of weakly pinned domain walls and current-assisted magnetization reversal in He(+)-irradiated Pt/Co/Pt nanotracks," *Journal of Physics D-Applied Physics,* vol. 44, 215002, Jun 2011.

[16] S. Emori and G. S. D. Beach, "Optimization of out-of-plane magnetized Co/Pt multilayers with resistive buffer layers," *Journal of Applied Physics,* vol. 110, 033919, Aug 2011.